

Copyright  
by  
Peng Chen  
2014

The Dissertation Committee for Peng Chen  
certifies that this is the approved version of the following dissertation:

**Immunomagnetic Circulating Tumor Cells (CTCs) Detection  
at Small Scale: Multiphysical Modeling, Thin-film Magnets  
and Cancer Screening**

Committee:

---

John X.J. Zhang, Supervisor

---

Tim H.C. Yeh, Co-Supervisor

---

James W. Tunnell

---

Jenny Ning Jiang

---

Kazunori Hoshino

**Immunomagnetic Circulating Tumor Cells (CTCs) Detection  
at Small Scale: Multiphysical Modeling, Thin-film Magnets  
and Cancer Screening**

**by**

**Peng Chen, BE, MSE**

**DISSERTATION**

Presented to the Faculty of the Graduate School of  
The University of Texas at Austin  
in Partial Fulfillment  
of the Requirements  
for the Degree of

**DOCTOR OF PHILOSOPHY**

THE UNIVERSITY OF TEXAS AT AUSTIN

August 2014

## **Dedication**

Dedicated to my beloved family.

## Acknowledgments

President Abraham Lincoln once said, “In the end it’s not the years in your life that count. It’s the life in your years.” Looking back at the past few years as a doctoral student, I feel so fortunate to have had so many people helping and supporting me generously, and I would like to express my sincere gratitude to all of them.

First and foremost, I want to thank my respected advisor, Dr. Xiaojing Zhang. He provided me with every bit of guidance, assistance, and expertise that I needed to finish my research work. I appreciate all of his contributions of effort and patience to make my PhD studies productive and stimulating. His conviction and determination will always push me toward a higher degree of excellence in future.

I am grateful for the insightful and enlightening suggestions on my thesis from my dissertation committee members and my co-advisor Dr. Tim Yeh, Dr. James Tunnell, and Dr. Jenny Jiang. I especially want to thank Dr. Kazunori Hoshino for his valuable advice, constructive criticism, and extensive and fruitful discussions. This thesis would never have come into shape without their help.

I also extend my thanks to Dr. Andrew Dunn, Dr. Pengyu Ren, Courtney Templeton, Brittain Sobey, and Krystal Peralez, who made my

life in the Biomedical Engineering Department meaningful and joyful. I am very thankful to my collaborators, Dr. Gene Frenkel and Dr. Konstantin Sokolov, for the priceless discussions regarding my research work and for broadening my horizons.

I want to thank past and present members of the Zhang group - Dr. Gauri Bhawe, Dr. Dajing Chen, Dr. Tushar Sharma, Dr. Youngkyu Lee, Dr. Youmin Wang, Elaine Ng, Kaarthik Rajendran, Nick Triesault, Oanh Ngoc Hoang, and Alice Chen - for being a fantastic source of friendships as well as for giving brilliant advice and collaborating. Special thanks go to Dr. Yu-yen Huang for his enthusiasm, intensity, and willingness to help me with my research and share his knowledge.

I will never forget the friends with whom I have been lucky and honored enough to be acquainted with during graduate school, especially Jing Cui, Dr. Hongkun Yang, Dr. Bingqing Wang, Dr. Biwei Yin, Dr. Zhen Xia, Dr. Chun-hsien Wu, Dr. Bin Yang, Cong Liu, and Yen-liang Liu. Our friendship will be everlasting.

Last but not least, I would like to thank my beloved parents Shuqing Chen and Yongdi Wei, and my grandma, Liangying Huo, for their sincere love and encouragement throughout my life for so many years.

Many thanks to all.

Peng Chen

# **Immunomagnetic Circulating Tumor Cells (CTCs) Detection at Small Scale: Multiphysical Modeling, Thin-film Magnets and Cancer Screening**

Publication No. \_\_\_\_\_

Peng Chen, Ph.D.

The University of Texas at Austin, 2014

Supervisors: John X.J. Zhang  
Tim H.C. Yeh

Circulating tumor cells (CTCs) are the cells that are shed from a primary tumor into the vasculature and circulate in the bloodstream. CTCs may trigger cancer metastasis, which leads to most cancer-related deaths. CTCs are widely studied due to their value in cancer diagnosis, prognosis, and oncology studies. The major challenges with CTCs lie in their extremely low concentration in blood, thus requiring an effective enriching system to enable downstream analyses.

The immunomagnetic assay has proved to be a promising CTC detection tool with high sensitivity and throughput. Key factors related to the immunomagnetic assay include the capture rate, which indicates the

sensitivity, and distributions of target cells after capture, which impact the cell integrity and other biological properties.

In this dissertation, we build a sedimentation model, a partial viscosity model, and a cell-tracking model to address the principle of the immunomagnetic cell separation. We examine the channel orientations and determine the favorable inverted condition. In addition, we develop a micromagnet approach to modulate the in-channel magnetic field toward enhanced cell detection and distribution. Through numerical studies, we calculate the magnetic field generated by the thin-film micromagnets, determine its effective ranges, and demonstrate its value in optimizing cell distribution. In the experimental demonstration, we present two types of micromagnets based on e-beam Ni deposition and inkjet printing technology, respectively. In the screening experiments, the Ni micromagnet integrated system achieves over 97% capture rate. It shows a 14% increase in capture rate, and a 14% improvement in distribution uniformity compared with plain slides. We also successfully isolate CTCs from metastatic cancer patients with the micromagnet assay. The inkjet-printed patterns yield a similarly high capture rate of 103%. With the pixel permanent magnet array, the inkjet patterns further increase the distribution uniformity for 20%.

The proposed models lay the theoretical foundations for future modification of the immunomagnetic assay, and the micromagnet-integrated system provides a promising tool for translational applications in cancer diagnose and clinical cancer management.

# Table of Contents

<b>Acknowledgments</b>	<b>v</b>
<b>Abstract</b>	<b>vii</b>
<b>List of Tables</b>	<b>xii</b>
<b>List of Figures</b>	<b>xiii</b>
<b>Chapter 1. Introduction</b>	<b>1</b>
1.1 Metastasis and Circulating Tumor Cells . . . . .	2
1.1.1 Cancer metastasis . . . . .	3
1.1.2 Circulating Tumor Cells . . . . .	4
1.2 Rare cell detection systems . . . . .	7
1.2.1 Physical separation . . . . .	8
1.2.2 Hydrodynamic sorting . . . . .	8
1.2.3 Dielectrophoretic separation . . . . .	9
1.2.4 Immunoassay . . . . .	10
1.2.5 Magnetic activated cell sorting . . . . .	12
1.3 Downstream analyses with CTCs . . . . .	20
1.4 Major contribution and dissertation organization . . . . .	23
<b>Chapter 2. Multiphysical Modeling and Theoretical Analyses</b>	<b>26</b>
2.1 Immunomagnetic assay . . . . .	26
2.1.1 Principle of operation . . . . .	26
2.1.2 Physics of magnetic separation . . . . .	27
2.2 Micro-environment simulation . . . . .	32
2.2.1 Blood sedimentation model . . . . .	33
2.2.2 Partial viscosity model . . . . .	36

2.2.3	Target cell tracking algorithm . . . . .	37
2.3	Microscale magnetic field modulation . . . . .	38
2.3.1	Micromagnet magnetization . . . . .	40
2.3.2	Micromagnet theoretical characterization . . . . .	41
2.3.3	Effect of micromagnet on CTC detection . . . . .	43
2.4	Summary . . . . .	45
<b>Chapter 3. Micromagnet Design, Fabrication and Integration</b>		<b>46</b>
3.1	Micromagnet overview . . . . .	47
3.2	Deposited thin-film micromagnets array . . . . .	53
3.2.1	Fabrication principle . . . . .	54
3.2.2	Fabrication results . . . . .	55
3.3	Inkjet printed micromagnets . . . . .	57
3.3.1	Fabrication principle . . . . .	58
3.3.2	Fabrication results . . . . .	59
3.4	Screening system . . . . .	61
3.4.1	Rotational screening stage . . . . .	62
3.4.2	Permanent magnet configuration . . . . .	64
3.5	Summary . . . . .	70
<b>Chapter 4. Results and Discussions</b>		<b>71</b>
4.1	Figures of merit . . . . .	72
4.2	Micro-environment analysis and CTC detection . . . . .	73
4.2.1	Blood characteristics measurement . . . . .	73
4.2.2	RBC sedimentation modeling results . . . . .	78
4.2.3	Computational analysis of rare cell isolation . . . . .	80
4.2.4	Experimental verifications . . . . .	86
4.3	Micromagnet characterization . . . . .	88
4.3.1	Micromagnetic field generation . . . . .	88
4.3.2	Impact of micromagnets on CTCs detection . . . . .	91
4.4	Screening results - Ni micromagnet . . . . .	93

4.5	Screening results - Inkjet micromagnets . . . . .	101
4.6	Summary . . . . .	106
<b>Chapter 5.</b>	<b>Conclusion and Future Work</b>	<b>108</b>
5.1	Conclusion . . . . .	108
5.2	Future work . . . . .	111
<b>Appendices</b>		<b>117</b>
<b>Appendix A.</b>	<b>Experimental protocols</b>	<b>118</b>
<b>Bibliography</b>		<b>127</b>

## List of Tables

3.1	Micromagnet designs, fabrications, characteristics and applications . . . . .	52
4.1	Pathology information and screening results using the Ni micromagnet-integrated immunomagnetic assay for patient studies. . . . .	100
A.1	Inkjet micromagnet fabrication waveform parameters . . . . .	126

## List of Figures

1.1	Steps in the process of metastasis. Cancer cells go through a series steps of local invasion, circulation, adhesion, extravasation before proliferating to form metastasis at a distant location. . . . .	4
1.2	CTCs and blood cell frequencies in blood. . . . .	5
1.3	Average cell diameter of some typical cancer cell lines. . . . .	7
2.1	Physical model and scaling law of the immunomagnetic cell separation system. Due to the attachment of the magnetic nanoparticles, motions of CTCs are dominated by the magnetic force. Reducing the height (H), increasing the magnetic field (B), and increasing the cross-section area ( $W \times L$ ) can help improve the separation efficiency. . . . .	27
2.2	Parameters that affect the detection efficiency of the immunomagnetic assay. . . . .	31
2.3	Red blood cell sedimentation model. RBC sedimentation in each control volume is given as a relative velocity $\Delta v_{RBC}$ of the RBCs to the medium and is expressed as a function of the volume RBC rate $\rho_{RBC}$ . . . . .	34
2.4	Partial viscos model: viscos force acting on a rare cell is the vector summation of the viscos force from the medium and the RBCs, each works in the same direction as its respective relative velocity. . . . .	37
2.5	Schematic of the patterned thin film micromagnet design and magnetization. (a) Patterned thin film micromagnet are integrated on the substrate and magnetized by the permanent magnets. (b) Magnetization process of the soft-magnetic micromagnets using the theory of magnetic anisotropy and demagnetizing field. . . . .	39
2.6	Analytical models to calculate the magnetic field generated by the thin-film micromagnets. (a) a single micromagnet element magnetized along the long axis. (b) an array of micromagnet elements aligned linearly on the substrate. . . . .	42

2.7	Analytical model of the microchip based immunomagnetic assay. (a) 2D model represents the microchip for rare cells detection. Liquid flow inside the channel follows standard parabolic profile. Permanent magnets are placed below the channel for attraction. (b) Magnetic field inside the microchannel generated by the permanent magnets. . . . .	44
3.1	Micromagnet technologies used for cell separation. (a) Micromagnetic strips made with nickel. (b) Array of nickel micro-posts. (c) shrink-induced groove micromagnet. (d) Thermally patterned micromagnets. . . . .	51
3.2	Fabrication process of the micromagnet using thermal desposition. Chromium is firstly deposited as adhesion layer, after which Nickel is deposited to form the magneti structure. At last, lift-off technique is used to remove the rest parts. . . . .	54
3.3	Design of the micromagnet array and key periodicity parameters. . . . .	55
3.4	SEM image of the nickel micromagnets fabricated using e-beam deposition. Inset shows a zoom-in image. . . . .	56
3.5	Observations of the CTCs being captured by the nanoparticles aggregated around the Ni micromagnet element. . . . .	57
3.6	Fabricating micromagnets using inkjet printing technology. Ink mixed with magnetic nanoparticles are printed on the substrate following a defined pattern. The substrate is then heat up to evaporate the ink liquid, and the nanoparticles are left behind and self-assemble the magnetic patterns. Finally, SiO <sub>2</sub> is deposited using PECVD as the protecting layer. . . . .	59
3.7	SEM image of the inkjet printed micromagnets. Inset shows the zoom-in view of the a printed pattern. . . . .	60
3.8	AFM measurement of the inkjet printed micromagnet pattern. The peak thickness of the pattern at the edge is ~300 nm. . . . .	61
3.9	Rotational stage to control the orientations of the microchip during the screening process. Inverted orientation reduces the sedimentation layer on top of the capture plane, and facilitates the cell separation in the channel. . . . .	63
3.10	Two types of permanent magnet configurations. (a) Three parallel design. (b) 6×6 pixel array with inserted spacers. . . . .	64

3.11	Magnetic field simulation results of the (a) three-parallel, and (b) pixel permanent magnet arrays. . . . .	65
3.12	Magnetic potential energy of target cells in (a) three-parallel, (b) pixel permanent magnet array. The logarithmic value of the magnetic potential energy in (c) three-parallel, (d) pixel permanent magnet array. . . . .	68
4.1	Fluorescent panel of COLO 205 and WBCs. COLO205 are CK+, DAPI + and CD45+, while WBCs have different expressions CD-, DAPI+ and CD45+. PC3, SK-BR-3 and MCF-7 all exhibit similar fluorescent signals to COLO205. . . . .	74
4.2	Red blood cell sedimentation rate measurement schematic. The sedimentation rate is defined as the growth rate of the sedimentation length $L$ in the tube. . . . .	75
4.3	Measured RBC sedimentation length changes for different volume RBC rates ( $\rho_{RBC} = 0.5, 0.25, 0.13, 0.06, 0.03, \text{ and } 0.01$ ). . . . .	76
4.4	Measured blood viscosity as a function RBC volume rate $\rho_{RBC}$ at different shear rates ranging from 2 to $750 \text{ s}^{-1}$ . Linear fit for each viscosity plot is also shown. . . . .	77
4.5	Comparative experiments of blood sedimentation in a bent tube. Photographs (preferred to be viewed in color) taken at (a) 20, (b) 80, and (c) 140 s. Simulation results at (d) 20, (e) 80, and (f) 140 s. . . . .	79
4.6	Configuration of the microfluidic immunomagnetic separation device. (a) Three-dimensional model created for a finite element analysis software <i>COMSOL</i> . (b) Flow velocity magnitude [mm/s] calculated with the sample flow rate of $Q = 10 \text{ mL/h}$ . . . . .	81
4.7	Simulated RBC sedimentation pattern inside the microchannel for (a) upright and (b) inverted orientations at the center $y$ plane at the time of 20, 40 and 80 s. Three-dimensional illustration of the sedimentation patterns in (c) upright and (d) inverted at the times of 270 s. Upright channel makes a thicker sedimentation layer on the bottom substrate and the corner near the inlet. . . . .	82

4.8	Side-view cell trajectories of the CTCs that are released at $t = 270s$ for the (a) upright and (b) inverted channels respectively. 3D views of the trajectories are also shown for the upright and inverted channels. Position of the magnets (cyan line) and shape of the microchannel (black lines) are included in the figures. . . . .	84
4.9	(a)-(d) RBCs sedimentation pattern calculated for the four control conditions (1-4) with different channel orientations, flow rates and channel designs at the time of $t = 270s$ . . . . .	85
4.10	(a)-(d) Simulated maps of the captured CTCs compared for the four conditions (1-4). In the simulation, 150 cells are released randomly from the inlet of the microchannel. . . . .	86
4.11	(a)-(d) Experimental maps of the captured CTCs compared for the four conditions (1-4). In the experiment, an average of 150 cells are spiked into blood. . . . .	87
4.12	Magnetic field and gradient calculated for a single micromagnet element (a) $B_x$ , (b) $B_y$ , and the magnetic field gradient (c) $\nabla B_x^2$ and (d) $\nabla B_y^2$ . The gray box indicates the lateral position of the micromagnet. The curves are plotted along horizontal lines ( $-40\mu m < x < 40\mu m$ ) with different heights ( $h = 5\mu m, 10\mu m$ and $15\mu m$ ) on top of the micromagnet. . . . .	89
4.13	Magnetic field (a) and magnetic field gradient (b) of an linear array of three micromagnets. The data are plotted $10\mu m$ on top of the micromagnet array. . . . .	91
4.14	Simulation results of the impacts of micromagnets on rare cell detection. (a) Sample cell trajectories in the microfluidic channel. (b) distribution histogram of the captured CTCs of micromagnet slide and (c) plain slide. . . . .	92
4.15	Ni micromagnet screening experimental results with COLO205 cells. (a) Overlay of fluorescence images and bright field images of CK-stained COLO205 cells (green) captured by Ni micromagnets. (b) SEM images of COLO205 cells captured next to or on top of the Ni micromagnet. . . . .	94
4.16	Ni micromagnet cell screening results. (a) Capture rates for the four cell lines: COLO205, PC3, SK-BR-3 and MCF-7. (b) Capture rate comparison between micromagnet slides and plain slides using COLO205 and PC3 cells as the screening targets. . . . .	95

4.17	Breakdown analysis of the spiked COLO 205 and PC3 cells based on how they are captured on plain and micromagnet slides respectively. . . . .	97
4.18	Micromagnet distribution analysis of the spiked experiments using COLO205. (a) Locations of the captured COLO205 cells on plain slide and micromagnet slide. (b) Distribution histogram of the captured CTCs from micromagnet slide and plain slide respectively. . . . .	98
4.19	Overlay of fluorescence image and bright field image of CTCs from patient blood samples captured by micromagnets. . . . .	99
4.20	(a) Magnetic fluorescent beads screening results with the inkjet printed patterns. (b) Relative fluorescent intensity profile exhibits regular repetition, with periodicity equal to the value of the printed patterns. . . . .	102
4.21	Brightfield and fluorescent images of the COLO205 cells found on the inkjet printed slides. Cells are either directly captured by the printed patterns or indirectly trapped by the magnetic nanoparticle aggregation around the printed patterns. . . . .	103
4.22	Cell screening results with COLO205 on patterned and plain slides. (a) Map and histogram on the printed slide. Blue cells are captured by the printed patterns, while orange cells are captured by the permanent magnets. (b) Map and histogram on plain slide. . . . .	105
5.1	Dissertation contribution. . . . .	111
5.2	Ciliated micropillar based CTC detection. (a) Schematic of the ciliated micropillar based CTC detection. The micropillars have one affinity domain that binds to cancer cells based on antibody-antigen bonding. The magnetic domain on the tip of the micropillar provides the momentum to the CTC-pillar complex. (b) SEM of the fabricated ciliated micropillars. (c) Preliminary results of the micropillar screening experiments - the cancer cell is captured due to the attachment with the micropillars. . . . .	114

5.3	Multi-target immunomagnetic CTC phenotyping. (a) Concept of the multi-target detection. (b) Simulated cell trajectories with three targets labeled with different amount of nanoparticles. (c) Simulated cell trajectories with three targets labeled with nanoparticles of different diameters. (d) Conceptual demonstration using two types of ferromagnetic nanoparticles (6 nm and 100 nm). The maximum difference in capture distance is 19%. . . . .	116
A.1	Grids on the hemacytometer. Average number of cells found in area 1~4 multiplied by $3 \times 10^4$ is the number of cells per mL in the original cell suspension. . . . .	120
A.2	Printing waveform of the inkjet printing instrument. . . . .	126

# Chapter 1

## Introduction

According to data from the American Cancer Society in 2014, cancer is the second-most common cause of death in the United States, exceeded only by cardiovascular diseases and accounting for nearly one of every four deaths. In 2014, about 585,720 Americans are expected to die of cancer, almost 1,600 people per day. One out of every two men and one out of every three women will experience some type of cancer in the course of their lives. [1, 2] Specifically, among the estimated new cancer cases, prostate (27%), lung and bronchus (14%), and colon and rectum cancers (8%) are at the top of the list for men, while breast (29%), lung and bronchus (13%), and colon and rectum (8%) are the three most frequently occurring cancer types for women. And globally, more people die from cancer every year than die from AIDS, tuberculosis and malaria combined. By 2020, we expect the number of new cancer cases to rise to 16.8 million, which will further increase to 27 million by 2030. [3]

To address the global cancer challenge, emerging technologies have been developed for cancer treatment, such as surgery, chemotherapy, and radiotherapy. In addition, a huge amount of effort is being dedicated to

developing cancer diagnoses, especially early-stage detection methods, because the effectiveness of the treatment is influenced by the stage at which cancers are diagnosed. Cancers are most responsive to treatment at early stages, and patients tend to have higher survival rates. Among all, Circulating tumor cells (CTCs), referring to the cancer cells that have escaped from primary tumor sites and circulate in the peripheral bloodstream, have been demonstrated to be an important indicator of carcinoma progression and metastasis, and can potentially be used as a early cancer detection tool.

Here, we begin with the background of cancer metastasis and the significance of studying CTCs. We then evaluate several existing CTC enriching systems with a focus on the immunomagnetic assay. Through theoretical modeling of the immunomagnetic assay from multiple physical perspectives, we propose to optimize the separation efficiency of the assay by manipulating local viscosity and modulating the near-field magnetic field with novel device implementation. Related concepts, designs, fabrication techniques, and characterization results are presented. In the end, we provide the experimental results using the new device in processing samples from both cultured cancer cells and cancer patients.

## **1.1 Metastasis and Circulating Tumor Cells**

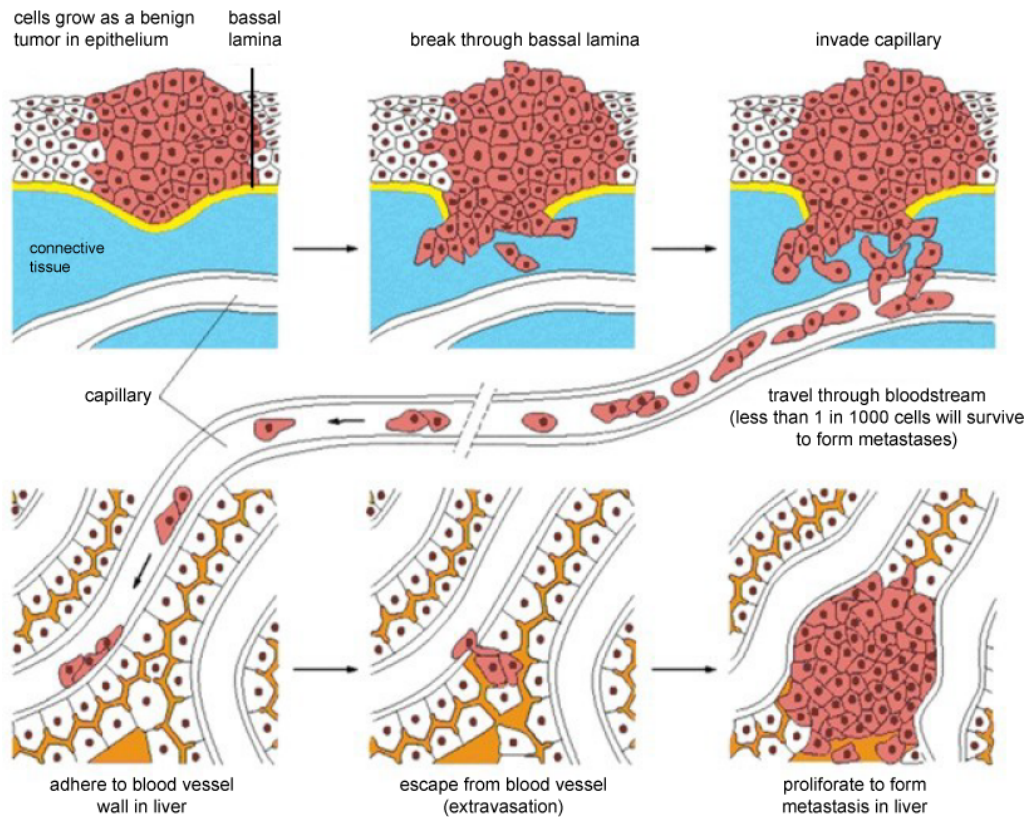
*“Cancer”* refers to a group of chronic diseases characterized by the uncontrolled growth of abnormal cells within the body. Normally, cells divide and replicate to replace worn-out cells or to repair some form of

injury to tissues of the body. After a certain period, normal cells wear out and die. However, cancer cells behave entirely differently - they keep growing, dividing and creating more abnormal cells, which eventually outlive normal cells. The abnormal cells often spread to other body parts, invading other biological organs. When they do spread, that is called metastasis. [3] If the spreading gets out of control, it can result in death.

### **1.1.1 Cancer metastasis**

Metastasis is the most lethal aspect of cancer, leading to more than 90% of cancer-associated deaths. By spreading throughout the body, cancer becomes almost impossible to eradicate through either surgery or radiotherapy. As shown in Figure 1.1 (adopted from [4], page 1221), metastasis is a multi-step process: the cancer cells have to invade local tissues and vessels, move through the circulation system (either blood circulation or lymphatic system), leave the vessels, and then establish new cellular colonies at a distant site. However, each of these events is complex, and most of the molecular mechanisms involved are not yet fully understood. [4]

In order to metastasize, cancer cells must break free of constraints that keep normal cells in their proper places and prevent them from invading neighboring tissues. This invasiveness is thus one of the defining properties of malignant tumors. Although the underlying molecular changes are not fully clear, it is believed that the invasiveness requires a disruption of the adhesive mechanisms that tether normal cells to their proper neighbors



[4] Alberts et al. *Molecular Biology of the Cell*. 2008

Figure 1.1: Steps in the process of metastasis. Cancer cells go through a series steps of local invasion, circulation, adhesion, extravasation before proliferating to form metastasis at a distant location.

and to the extracellular matrix. For carcinoma, this process resembles the *epithelial-to-mesenchymal transition (EMT)*.

### 1.1.2 Circulating Tumor Cells

Circulating tumor cells (CTCs) are cancer cells that have escaped the primary tumor site and now circulate in the peripheral bloodstream (as

shown in Figure 1.1). In 1989, English surgeon *Dr. Stephen Paget* first used the “seed and soil” theory to explain cancer metastasis. Here the “seed” is the CTCs and “soil” is the body tissues. [5] Now it is widely accepted that CTCs in the blood originate from solid tumors, and the presence of viable CTCs can be an important indicator of carcinoma progression and metastasis. Despite the fact that detection and characterization of these cells can be a promising method for both diagnosis and clinical management of cancer, there are two major challenges that need to be resolved to fully exploit the potential of CTCs.

- Rareness

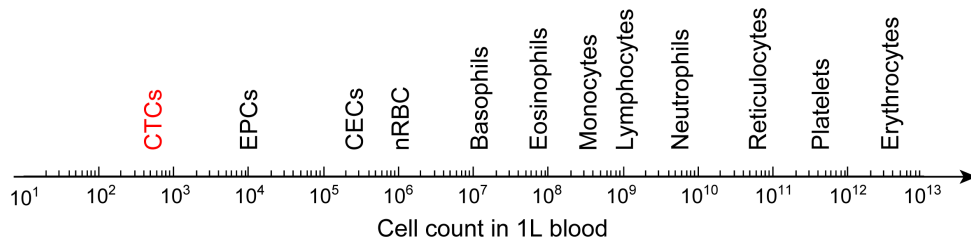


Figure 1.2: CTCs and blood cell frequencies in blood.

To complete the metastasis process, the detached cancer cells must go through a complex, slow, and inefficient process. It needs the particular stem-cell character that will enable them to divide without limit, the ability to settle and survive in an alien environment to proliferate, and being resistance to apoptosis. All of these restraints make CTCs an extremely rare event in blood. [4] It is estimated that, among the cells that detach from the primary tumor, only 0.01% translate into viable CTCs that can form metastasis. [6] As

shown in Figure 1.2, CTCs are found in frequency on the order of  $10^2 \sim 10^3$  per 1L of blood. In contrast, the same amount of blood contains billions ( $10^9$ ) of white blood cells and trillions ( $10^{12}$ ) of red blood cells. To overcome the limitations of low concentration, it is imperative to have enriching systems that can isolate and preserve CTCs before any further molecular studies are conducted.

- Heterogeneity

Many of the existing CTC enrichment systems distinguish CTCs from background cells based on the surface biomarker recognition or the size differentiation. However, the heterogeneity of CTCs in biomarkers and sizes hinders the performance of these technologies.

Specifically, the biomarker expressions vary among different cancer types. So far, EpCAM, EphB4, EGFR, CEA, HER2, and MUC-1 have all been adopted to do CTC separation from breast and colon cancer patients. [7] Even for the same cancer cell line, the biomarker expression may vary. For example, the most commonly used epithelial cell surface marker - EpCAM - is not expressed or is expressed at a low level in some tumors and may be down regulated during the *EMT* transition. [8] Therefore, discovering more biomarkers relevant to CTCs and developing multiplex labelings are necessary to improve the efficacy of these CTC detection assays. [9]

The size-based isolation methods are generally based on the assumption that CTCs are larger than the surrounding normal blood cells. However,

as shown in Figure 1.3, the average diameters of different cell lines differ. It is hard to differentiate some relatively smaller CTCs, such as NCI-H69 from leukocytes (typical diameter  $\sim 12 \mu m$ ). [10] In addition, the size of the CTCs may show some dynamic changes under different conditions. For example, CTCs found from patients ( $7.97 \mu m$ ) are significantly smaller than cultured cancer cells ( $13.38 \mu m$ ), with a more elongated shape. [11] These variations make it even more difficult to select an appropriate size threshold for accurate cell separation.

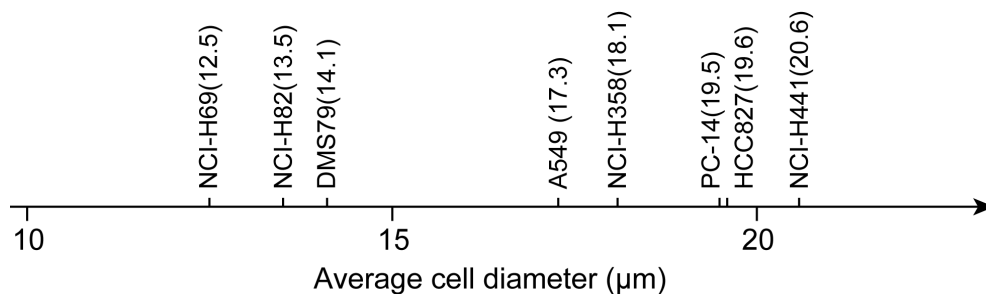


Figure 1.3: Average cell diameter of some typical cancer cell lines.

## 1.2 Rare cell detection systems

Over the past decade, CTC detection has been an exciting field, and many technologies have been proposed and successfully demonstrated. [12–16] Based on the separation mechanisms, these technologies can be categorized as (1) physical parameters based separation (size and density gradient, dielectrophoretic separation, and hydrodynamic separation) and (2) affinity mediated separation (immunoassay and immunomagnetic separation). In this section, we will introduce and evaluate these methods.

### **1.2.1 Physical separation**

Separation based on physical parameters distinguishes CTCs from normal blood cells by relying on one or more intrinsic properties of the CTCs (such as size, density, deformability, and electrical charges) without external labels. [17–20] The size filtration method, such as the microcavity array, works under the assumption that carcinoma cells are generally larger than normal blood cells. [21] Density gradient centrifugation based cell enrichment is based on the differences in cellular buoyant density. [22] There are also techniques performing CTCs separation based on cell deformability, such as the micro-isolation well design that achieves >80% capture efficiency for breast and colon cancer cells. [23] Although filter based approaches are relatively simple and straightforward and are not limited by cell types, these techniques cannot differentiate between cancer cells and normal blood cells that are physically similar. Besides, when passing through the filtration systems, CTCs may potentially be damaged or lost due to the increased shear stress. Additionally, low pore density and pore fusion of the filter structures may limit the flow rate and fundamentally hinder the system throughput. [24]

### **1.2.2 Hydrodynamic sorting**

A promising alternative to the filtration system is to separate cells in a streamline by manipulating the hydrodynamic forces applied on cells. Cells with different sizes or shapes behave differently in the streamline and

can be sorted accordingly. [25,26] The continuous deterministic flow array is one of the earliest methods used to separate blood components based on the hydrodynamic size. The streamline of the object is dependent on the relation between the its diameter and the micro-post offset spacing. [27,28] A microscale vortices based CTCs separation system has been demonstrated using size as the biomarker, in which cancer cells with larger diameters migrate to and are enriched in the expansion-contraction trapping reservoirs while smaller cells freely pass through the reservoir region. The separation is due to the lift forces that cells encounter are different. [29] Additionally, the spiral microchannel design focuses larger CTCs against the inner wall of a curvilinear chamber and use the inherent Dean vortex flow to collect the CTCs in the inner outlet. [30–32] In asymmetric pinched flow fractionation, cells with different sizes and shapes move along different streamlines and enter different collection outlets. [33] Hydrodynamic separation operates with high flow rates and does not suffer from an increased shear stress, because no physical filtration is present. However, to keep the carrier liquid consistent in properties such as viscosity, the sample usually needs to be diluted appreciably before being screened, which limits the separation efficiency and throughput.

### **1.2.3 Dielectrophoretic separation**

Electrical properties of cells can also be used to perform separation. [34,35] When an external alternating current electric field is applied, cells are

polarized by the field and affected by the applied dielectrophoretic (DEP) force. The bottom of the liquid chamber is lined with an inter-digitated microelectrode array. When inside the channel, cell equilibrium height in the parabolic fluid-flow profile is determined by the balance of DEP levitation forces generate by the inter-digitated microelectrodes and the sedimentation force. Cells are lifted to different heights and are transported with different velocities in the parabolic flow profile. Cells that are farther from the bottom electrode are carried faster by the fluid. Therefore, blood cells move faster near the center, whereas CTCs move slower near the edge, and become separated thereby. [36] The existence of different components can usually be read out from the multiple peaks in the time dependency cell fractogram passing through the detection window.

DEP systems are appealing because a large amount of blood sample can be treated in a flow-through device without labeling, and target cells can be collected for further analyses. However, to increase the separation resolution, a large chamber size is preferred, and a DEP system usually requires an external power supply, both of which lower the portability of the system.

#### **1.2.4 Immunoassay**

Other than the physical parameters, CTCs can also be differentiated from normal blood cells based on the surface biomarkers. In the immunoassays, affinity ligands are used to provide the capture force for cell

separation. Due to the highly selective nature of antibody-antigen interactions, immunoassays usually display better sensitivity and specificity than physical separations.

Immunoassay is first demonstrated with the three-dimensional micro-post structures (the “CTC-chip”). The micro-posts are coated with cancer-specific antibody (anti-EpCAM), and successfully identify CTCs in the peripheral blood of patients with metastatic lung, prostate, pancreatic, breast and colon cancers with >90% accuracy. [37] Afterwards, a number of devices with carefully engineered three-dimensional in-channel structures are developed to increase the separation efficiency. [38] The “herringbone-chip” applies passive mixing of blood cells through the generation of microvortices to increase the effective interactions between target CTCs and the antibody-coated chip surface. The system increases the capture efficiencies for 26.3% on average compared with the CTC-chip, especially at higher flow rates. [39]

To overcome the limitations of using EpCAM as the major biomarker for CTCs detection, while in fact the amount of EpCAM expression on tumor cells varies largely and depends on the cell types, aptamers have been introduced to improve the versatility of CTCs detection. Since aptamers can easily be modified for any subpopulation of CTCs, and they can be easily immobilized within a device, multiple types of CTCs can be detected at the same time. [40,41] In the meantime, ensemble aptamers and antibodies on the same substrate and create a multivalent adhesive domain could further increase both the efficiency and purity of CTCs separation. [42]

However, the affinity mediated immunoassays are still limited by the relatively slow transport of target cells to the capture surface. Besides, selecting an appropriate shear stress that can both facilitate reactions between CTCs and surface molecules, and dissociate the non-specific bonds to remove non-target cells is difficult. To address these challenges, a fluid-permeable nanoporous membrane has been recently integrated to the immunoassay to promote surface reactions and reduce non-target fouling. The nanoporous structure enhances transport as streamlines are diverted toward the surface, and eventually significantly increases the CTCs capture rates at high flow rates. [43,44]

### **1.2.5 Magnetic activated cell sorting**

In systems such as fluorescence-activated cell sorting (FACS) and magnetic-activated cell sorting (MACS), affinity ligands are used as a labeling mechanism. FACS has been widely used in past decades; the method sorts a heterogeneous mixture of cells into multiple containers based on fluorescent signals. [45] Recent developments in nanotechnology have enabled miniaturized FACS systems based on microfluidics and pulsed lasers. [46,47] However, FACS is usually designed to sort cells with large sub-populations and lacks the sensitivity to separate cells as rare as CTCs.

In a MACS system, magnetic force is applied to separate CTCs. The magnetic momentum of the cancer cells comes from the magnetic tags that are conjugated selectively to cancer cells through antibody-antigen bindings.

Depending on the desired field intensity, either permanent magnets [48] or electromagnets [49] can be used to provide the magnetic attraction. Compared with other CTCs enrichment methodologies, an immunomagnetic assay has several advantages that make it especially promising regarding translational applications.

**Selectivity:** Similar to affinity mediated immunoassays, immunomagnetic assays have good sensitivity that arises from antibody-antigen binding.

**Specificity:** Using magnetic force as the retaining force, immunomagnetic assay increases the contrast between target and non-target cells in terms of the surface binding.

**Throughput:** Immunomagnetic assay requires no direct contact between CTCs and surface molecules. The large working range of magnetic attraction allows for large chamber size and high throughput.

**Tunability:** The magnetic field can be easily and accurately modulated, especially when an electromagnet is used as the magnetic field source.

**Integration:** Magnetic attraction can be integrated with other separation methods due to the large effective range. [50]

Various immunomagnetic assays have been developed for cell separation purposes in the past decades. With the progress in microfabrication technologies, there is a trend toward miniaturization because it provides better confinement of the magnetic force and other related factors on a small

scale. In the following review sections, we follow the order of the scale of the immunomagnetic devices, from macroscale to microscale.

### **Macroscopic magnetic activated separation system**

In conventional magnetic activated cell separation systems, samples are stored in conical tubes and the screening/flushing steps are usually done manually. Cells labeled with supermagnetic microbeads are attracted to the tube wall, and unlabeled cells are eluted. Once the external magnetic field is removed, the labeled cells can be released. [51] Bulky permanent magnets provide the magnetic field and are arranged either as dipole or quadrupole separators. Dipole separators drive cells across the streamlines with a constant magnetostatic energy gradient, while quadrupole separators deflect and capture cells in the radial direction. Separating rare cell samples with a conventional MACS system is usually a time-consuming process with low throughput because the system is manually operated and the magnetic field intensity is typically limited. [52]

Recently, a new magnetic cell sorting system - *MagSweeper* technology is reported. In the system, magnetic rods covered with plastic sheaths are swept through the well to magnetically attract microbead-labeled target cells. [53,54] The diluted blood samples are pre-labeled with magnetic particles, and the samples are loaded into the capture wells. Sheath-covered magnetic rods are swept a few millimeters above the bottom of the wells. Loosely bound contaminating cells are removed, while the sheathed rods

are washed. An external magnetic field is applied to facilitate the release of labeled cells and the excessive magnetic particles. Using multiple rods, the system can process different samples at the same time. However, during the screening process, sheaths considerably reduce the magnetic force on the magnetic rods and may lower the capture efficiency.

*CellSearch<sup>TM</sup>*, a commercial system used to detect CTCs, is also based on the magnetic separation. *CellSearch<sup>TM</sup>* is among the few systems that have been approved by the U.S. Food and Drug Administration (FDA) for clinical diagnostics of breast, colorectal, and lung cancers. The system includes cell preservation tube, cell profiling kit, and a semi-automated sample scanning system. CTCs labeled with magnetic ferrofluids nanoparticles conjugated with EpCAM are isolated from whole blood samples by external magnets. [55] *CellSearch<sup>TM</sup>* has been widely used to study the correlation between the CTC counts and the survival rates of patients with breast, prostate and colorectal cancers. [56–62] The limitations of the *CellSearch<sup>TM</sup>* system include the fixed target assay designed only for EpCAM expression which may lead to low capture efficiency in many clinical cases. Besides, instead of collecting captured cells, the system re-suspends the captured cells in the original screening solution after fluorescence imaging. It is difficult for the captured cells to be retrieved on slides for further analyses.

Conventional MACS plays significant roles in cancer biology and clinical studies, as revealed by the high level of interest and research activities in CTCs. The field has been expanding remarkably fast in the past

few years, and the enrichment techniques are continuously improved. At present, the conventional MACS system cannot perform as needed for sophisticated molecular studies. In addition, the bulky size and low portability restrict their applications for point-of-care medical systems.

### **Microscopic based immunomagnetic assay**

With the recent advancement of micro and nano-fabrication techniques, researchers are able to make miniaturized tools to observe, measure, and manipulate extremely small objects. Combining microfluidic technologies, which is known for being able to provide precise control of the flow behavior, transportation, and biological interactions in a microchannel environment, with immunomagnetic assay has been well pursued for separation of rare cells. Similar to the conventional MACS system, microscopic immunomagnetic assay uses magnetic beads or particles that are conjugated with cancer specific antibodies to label target cancer cells and uses an external magnetic field for isolation.

Depending on the direction of the magnetic field, the microscopic immunomagnetic assays work either in a retaining mode, where CTCs are captured and fixed on a solid substrate; or in a deflection mode, where CTCs are magnetically driven to different streamlines to be collected at different outlets. There are also hybrid microchannels being reported that consist of multiple functionalities or separating mechanisms integrated on the same chip.

Early work on combining microfluidic and immunomagnetic assays to study cells in the retaining mode begin with analytical magnetapheresis. It is proposed to compare magnetic properties of iron-rich protein (ferritin)-labeled human lymphocyte and magnetite-doped dynabeads. When flow through the microchannel over permanent magnets at a controlled flow rate, magnetized cells and dynabeads are magnetically attracted to the interpolar gap of the magnets, and can be used for microscopic analyses. [63]

Recent work on a microchip-based immunomagnetic separation system in retaining mode has been successfully demonstrated with CTCs. [48, 64] During the screening process, magnetic nanoparticle-labeled CTCs in whole blood sample are pumped into the microchip and are captured on the channel substrate. Normal blood cells such as red blood cells (RBCs) and white blood cells (WBCs) are able to escape the magnetic entrapment. The system yields high capture efficiency and throughput with blood samples from breast, prostate, and lung cancer patients. It also discovers clusters of CTCs, which might be clinically important.

The deflection channel is another cell sorting scheme. A stack of permanent magnets are placed close to a microfluidic channel on the side face to do sorting based on ferrohydrodynamics in a continuous-flow device. [65] Different targets are deflected, and can be collected at different outlets. It is demonstrated with *Escherichia coli* and *Saccharomyces cerevisiae*, as well as fluorescent polystyrene microparticles. However, the device needs to be further optimized in terms of separation sensitivity for target cells with

small differences for clinical applications.

Viable CTCs can be retrieved using an immunomagnetic assay for cell culture. Integration of micro-chambers with a microfluidic magnetic separation device is developed to isolate CTCs suspended in whole blood sample from mammary cancer-bearing mice. The isolated CTCs can then be retrieved and cultured. The device is composed of a tilt inlet channel at a certain angle in a main microfluidic channel with two rows of dead-end side chambers to store attracted CTCs and protect them from being damaged by shear stress. The device displays good isolation efficiency (87%) using spiked mouse metastatic M6C breast cancer cells. [66]

As we mentioned previously, the far-field property of the magnetic field allows integration with other functional components to achieve better separation performances. A microfluidic chip (“CTC-iChip”) containing three separation stages, namely debulking, inertial focusing, and immunomagnetic separation, is fabricated for CTC detection. [67, 68] The system incorporates three microfluidic functions to replace bulk RBC lysis and centrifugation, hydrodynamic sheath flow in flow cytometry, and magnetic-activated cell sorting in serial. Specifically, hydrodynamic size-based filtration is performed in the first stage using an array of micropillar structures, in which RBCs, platelets, plasma proteins, free magnetic beads, and other blood components are discarded through the top outlet. The remaining CTCs and WBCs are then flowed to the second stage for inertial focusing before going to the third stage where immunomagnetic separation

is performed. The developed CTC-iChip is capable of immunomagnetically sorting epithelial and non-epithelial cancer cells in both negative and positive modes. It exhibits high capture efficiency for different human cancer cell lines expressing different levels of EpCAM, even for MDA-MB-231 - a “triple-negative” mesenchymal breast cancer cell line.

In addition to the integration in serial, immunomagnetic assay can be combined with other principles in parallel. A micro-aperture chip system is proposed to combine magnetic separation with size-based filtration. [69] A magnetic field draws the magnetic bead-bound cells toward the microchip which contains apertures that allow passage of unbound beads while trapping the target cells. It is particularly effective in removing the excessive magnetic nanoparticles in the system for better cell observation.

From macroscopic to microscopic, the downscaled immunomagnetic system provides better control of the flow field and magnetic field. Miniaturization also offers advantages such as better separation performance, low material consumption, and high protability, all of which are critical for potential mobile healthcare applications. However, the miniaturization is limited by the need to avoid cell clogging and the desire to keep a substantial system throughput to reduce the testing time.

### 1.3 Downstream analyses with CTCs

Microscopic immunomagnetic assay enables the researcher to capture and retrieve viable CTCs. It opens up opportunities to perform more in-depth studies with the CTCs. Meanwhile, with the development of cell profiling techniques, such as FISH, PCR, RT-PCR, plenty of information have been extracted from CTCs. In this section, we will review some of the significant work regarding downstream analyses of CTCs and introduce its contributions to biological and clinical studies of cancer.

Specifically, we will cover (a) estimation of the metastatic progression and survival rates, (b) stratification and real-time monitoring of therapies, and (c) identification of therapeutic targets and resistance mechanisms. In the end, we outline the requirements posted on CTCs separation technology in order to better carry on the downstream analyses, which lay the foundation for this dissertation.

#### **Estimation of the metastatic progression and survival rates.**

The number of CTCs found from blood samples can be used to estimate the metastatic progression and survival rates of the patients. Metastatic breast cancer patients can be determined as favorable ( $<5$ ) and unfavorable ( $\geq 5$ ) based on Kaplan Merier probability of the CTC counts at monthly interval after initiation of therapy. The difference in survival rates between the favorable and unfavorable groups is highly significant ( $p\text{-value} \leq 0.0070$ ). Besides, changes in CTC counts after treatment can alter survival prospect-

s. CTCs are acquired using *CellSearch*<sup>TM</sup> from 7.5 mL of patient blood. The results indicate that patients with persistent CTC counts have the worse outcome and strongly suggest they are on a futile therapy. The same methods can be applied with colorectal and prostate cancer patients. [56]

### **Stratification and real-time monitoring of therapies**

*EMT* transition - the process of adherent epithelial cells becoming a migratory mesenchymal state has been considered to be a fundamental step in tumor metastasis. In general, primary tumor cells simultaneously express mesenchymal and epithelial markers, but mesenchymal cells are highly enriched in CTCs. Therefore, monitoring the dynamic change of the biomarkers on mesenchymal CTCs can be used for stratification and real-time monitoring of therapies and disease progression. Longitudinal monitoring the EMT features (E&M markers) in CTCs from a ER/PR<sup>+</sup> lobular breast cancer patient showed the patient had initially responded to a regimen of PI3K+MEK, developed resistance, and then responded transiently to standard chemotherapy. The color-coded quantification of EMT features show excellent agreement with the disease progression and therapy response. It demonstrates the clinical importance of CTC as a potential biomarker for cancer management. [70,71]

## Identification of therapeutic targets and resistance mechanisms

Sub-microgram RNA-based sequencing method can be used to generate gene expression profile of CTCs. In the study of pancreatic CTCs, Wnt2 is found to be consistently enriched in CTCs. The existence of Wnt2 is confirmed using fluorescent RNA *in-situ* hybridization (RNA-ISH) technique. In the functional consequence test, Wnt2 is found to promote anchorage-independent cell survival and may contribute to metastasis in human pancreatic cancer. In the inhibitor test, TAK1 (TGF- $\beta$  activated kinase 1) is found to be capable of abrogating Wnt2-induced tumor spheres, without suppressing baseline formation, thus can be a potential drug target for metastasis suppression. [72] Therefore, molecular analysis of CTCs may identify candidate therapeutic targets for cancer treatment and resistance mechanisms.

Molecular analyses of CTCs have been a highly active research area. There are many other exciting work, such as detection of mutations in EGFR in circulating lung cancer cells offers the possibility to track the changes in tumor genotypes during treatment, [73] and studying the phenotype-dependent effects of EpCAM expression to implicate EpCAM-based targeting strategy. [74] Besides, CTCs can be used as a non-invasive liquid-biopsy to study the heterogeneity of cancer cells [54] and eventually aid the development of personalized therapies. [75–77]

However, to overcome the limitations from the rareness and fully exploit the potential of CTC, huge challenges are posted on the enriching tech-

nologies. Currently, there are two major areas that attract lots of dedication. **(1) Efficient separation.** Since CTC is such a rare event in blood, it is always important to optimize the separation system in the sensitivity, specificity, versatility and stability. **(2) Convenient identification.** Although advanced techniques like fluorescent *in-situ* hybridization (FISH), PCR can be used for cell identification, immuno-fluorescent imaging is still the most widely-adopted method due to its simplicity and straightforwardness. Therefore, the separation system needs to maintain cell integrity, facilitate the cellular imaging, and avoid negative factors such as fluorescent quenching.

## 1.4 Major contribution and dissertation organization

In the dissertation, we build an immunomagnetic assay for efficient rare CTCs detection. We start with deriving the theoretical models to simulate the magnetic-driven motions of CTCs, which provides quantitative guidance in the system design. Then we present the design, the fabrication of a microscale magnetic structure, and the integration with the immunomagnetic assay as an enhanced platform. In the end, experiments with different cancer cell lines are carried out to evaluate the system.

Specifically, the major contributions of this dissertation include the following:

First, modeling and theoretical analyses of the immunomagnetic assay. We develop multi-physical models to address the governing physics

of magnetic separation. Then we build a blood sedimentation model to simulate the mechanical motion of the red blood cells within microchannels and a partial-viscosity model to investigate the impact of the changes in the micro-environment on rare cell separation. In addition, we derive the principles for the implementation of micro-scale magnetic structures, and demonstrate its value in altering the distribution of the captured cells.

Second, design and fabrication of micromagnet-integrated microchip system for rare cell detection. We design and fabricate a thin-film microscale magnetic structure with a traditional e-beam deposition technique to modulate the local magnetic field. In addition, we develop the inkjet-printing technology as a flexible alternative approach to fabricate micromagnets for magnetic activated patterning and separations.

Third, experimental analyses of the micromagnet-integrated assay in detecting multiple types of rare CTCs. We test the micromagnet-integrated immunomagnetic assay with cultured breast, prostate and colon cancer cells to characterize the capture capabilities. The experimental results match the theoretical predictions well. On average, the Ni-micromagnet integrated system achieves over 97% capture rates with four types of cancer cell lines: COLO205, SK-BR-3, MCF-7, and PC3. Compared with plain slides, the Ni micromagnet slides increase the capture rate by 14% on average. It also improves the distribution uniformity by  $14\pm 8\%$ . The Ni micromagnet integrated system has also been used to study clinical samples, and successfully isolate CTCs from four types of metastatic cancers patients (breast, prostate,

lung, and colon cancers). The inkjet printed patterns yield a similarly high capture rate of  $103\pm 1\%$ , a  $35.5\pm 16.5\%$  increase compared with plain slides. With the help of a newly designed pixel permanent magnet array, the inkjet patterns further increase the distribution uniformity by 20%.

In this dissertation, Chapter 1 introduces the motivation and background of CTC studies, with substantial reviews of existing technologies for CTC separation and downstream analyses. Chapter 2 presents the multi-physical modeling of the immunomagnetic assay, together with the theoretical framework of the micro-environment analysis and microscale magnetic field modulation. The fabrication and device characterization of the micro-magnets, and its systematical integration are presented in Chapter 3, while Chapter 4 presents both the simulation and experiment results in using the proposed device for screening CTCs from spiked and clinical samples. Finally, Chapter 5 summarizes the thesis and discusses future work.

## Chapter 2

### Multiphysical Modeling and Theoretical Analyses

This chapter presents the theoretical framework of the immunomagnetic assay from multiple physical perspectives. Starting from the governing physics of magnetic cell separation and the scaling law of the immunomagnetic assay, we identify two important parameters - local viscosity and magnetic field - that are closely related to the separation efficiency. We then build a set of models, including the blood sedimentation model, the partial viscosity model, and the cell tracking model, to quantify the impact of local viscosity on cell separation. Also, we introduce the analytical model of the micromagnets' implementation to characterize the magnetic field generation and the impact on the immunomagnetic assay. The theoretical investigations lay the foundation for the device design and fabrication.

#### 2.1 Immunomagnetic assay

##### 2.1.1 Principle of operation

The principle of the immunomagnetic assay is shown in Figure 2.1. CTCs are conjugated with magnetic nanoparticles through cancer specific antibodies (such as anti-EpCAM) before being pumped into the microchan-

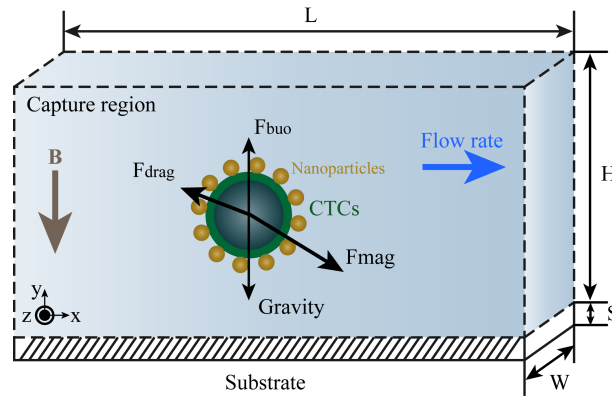


Figure 2.1: Physical model and scaling law of the immunomagnetic cell separation system. Due to the attachment of the magnetic nanoparticles, motions of CTCs are dominated by the magnetic force. Reducing the height ( $H$ ), increasing the magnetic field ( $B$ ), and increasing the cross-section area ( $W \times L$ ) can help improve the separation efficiency.

nel. When inside the channel, which is placed within strong external magnetic field, the CTCs are subject to the gravitational force ( $G$ ), buoyancy force ( $F_{buo}$ ), magnetic attractive force ( $F_{mag}$ ) and the hydrodynamic force ( $F_{drag}$ ). Due to the attachment of the nanoparticles, the magnetic force largely overweighs other forces. Therefore, the CTCs can be magnetically attracted, retained on the substrate of the microchannel, and get separated thereby. In the meantime, normal hematocyte cells flow out of the microchannel unaffected.

### 2.1.2 Physics of magnetic separation

The physical principles of immunomagnetic assays evolve over the length-scale. To elucidate key design parameters, we discuss the scaling

laws of the immunomagnetic assay. Consider a virtual immunomagnetic capture region as shown in Figure 2.1, with length ( $L$ ), width ( $W$ ), height ( $H$ ) and substrate thickness ( $S$ ). If the dimensions of the permanent magnets are greater than the capture region, the magnetic field within the region falls off inversely with the square of the distance to the magnets ( $y$ ):

$$B(y) \propto \frac{B_0}{(S + y)^2} \quad (0 < y < H) \quad (2.1)$$

Here  $B_0$  is the magnetic field generated by the magnetic flux source, i.e. the permanent magnets. The average time ( $\tau$ ) a cell stays inside the capture region can be estimated using the flow rate ( $FR$ ) and the dimensions of the region:

$$\tau = \frac{W \cdot H \cdot L}{FR} \quad (2.2)$$

The magnetic force acting on a magnetic nanoparticle ( $F_{\text{mag}}$ ) is dependent on the magnetic dipole momentum  $\mathbf{m}$  of the particles and the magnetic field  $\mathbf{B}$ :

$$F_p = (\mathbf{m} \cdot \nabla)\mathbf{B} \quad (2.3)$$

The total magnetic momentum of a nanoparticle can be expressed using:

$$\mathbf{m} = \frac{V_p \Delta\chi_p}{\mu_0} \mathbf{B} \quad (2.4)$$

Here  $V_p$  is the volume of a single nanoparticle,  $\Delta\chi_p$  is the volume magnetic susceptibility of the magnetic nanoparticles,  $\mu_0 = 4\pi \times 10^{-7} \text{ T}\cdot\text{m}\cdot\text{A}^{-1}$  is the magnetic permeability of vacuum. We assume  $\nabla \times \mathbf{B} = 0$ , and the magnetic force on a single nanoparticle can be simplified to :

$$F_p = \frac{V_p \Delta\chi_p}{2\mu_0} \nabla B^2 \quad (2.5)$$

Therefore, the magnetic force on a target cell ( $F_c$ ) is the summation of the forces from all the particles:

$$F_c = N \cdot F_p \quad (2.6)$$

where  $N$  is the amount of labeling particles on a single cell.

When the magnetic force drives cells along the laminar flow inside the capture region, the hydrodynamic drag force can be calculated using Stoke's equation:

$$F_{drag} = 6\pi\eta R\Delta v \quad (2.7)$$

To simplify the calculation, we assume a quasi-static cell motion, neglecting the accelerating period, equating the drag force to the magnetic force:

$$F_{drag} = F_c \quad (2.8)$$

And we can get the expression of the instant relative velocity of the target cell:

$$\Delta v = \frac{R_c^2 \Delta \chi_c}{9\mu_0 \eta} \nabla B^2 \quad (2.9)$$

Here  $R_c$  is the hydrodynamic radius of the cells,  $\eta$  is the viscosity of the medium, and  $\Delta \chi_c$  is the effective magnetic susceptibility of the target cells, represented using:

$$\Delta \chi_c = N \cdot \frac{R_p^3}{R_c^3} \cdot \Delta \chi_p \quad (2.10)$$

We can calculate the average velocity of the cells by averaging over the height of the microchannel.

$$v_{ave} = \frac{1}{H} \cdot \frac{R_c^2 \Delta \chi_c}{9\mu_0 \eta} \int_0^H \nabla B^2(x) dx \quad (2.11)$$

In the theoretical consider, a successful capture is defined that - within the time  $\tau$  the vertical distance moved by the cells is equate to the height of the capture region:

$$\tau \cdot v_{ave} = H \quad (2.12)$$

Based on the Equation 2.12, we calculate the required magnetic field intensity for successful magnetic separation:

$$B_0 = \frac{9\mu_0\eta}{R_c^2\Delta\chi_c} \cdot \frac{H \cdot FR}{W \cdot L} \cdot \frac{1}{(S + H)^{-4} - S^{-4}} \quad (2.13)$$

We assess the immunomagnetic assay based on the required minimum magnetic field ( $B_0$ ). The parameters that help reduce the value of  $B_0$  lower the physical barrier for cell isolation. In contrast, parameters that increase the value of  $B_0$  make the cells less likely to be captured. Thus, we can divide all the parameters into two groups, based on the effect on CTC detection efficiency, as shown in Figure 2.2.

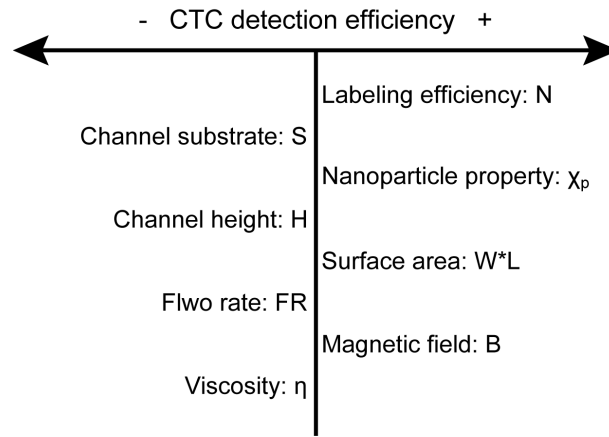


Figure 2.2: Parameters that affect the detection efficiency of the immunomagnetic assay.

According to Figure 2.2, there are several ways to improve the CTC detection efficiency, such as decreasing the screening flow rate ( $FR$ ), using stronger magnetic tags ( $\chi_p$ ), and increasing the labeling efficiency ( $N$ ).

However, from the perspective of scale, the system can be optimized by decreasing the height ( $H$ ) and increasing the surface area ( $W \times L$ ) of the device. It inspired us to scale down the device, and adopted the microchip approach with large flat hexagon chamber geometry. [48]

Meanwhile, we identify two additional parameters that can potentially be adjusted to increase the CTC detection efficiency - the viscosity ( $\eta$ ) and the magnetic field ( $B$ ). Viscosity is decided by the screening medium - blood and its cellular components. While the magnetic field is affected by the permanent magnets outside the channel, and the microscale magnetic structures we propose to implement inside the channel. In the following parts, we introduce the theoretical endeavors in investigating these two factors.

## **2.2 Micro-environment simulation**

In the previous theoretical considerations of the immunomagnetic assay, blood is simply treated as a viscous Newtonian medium, [63] which is sufficient to roughly estimate the blood flow and device functionality for certain applications. However, it does not represent the essential phenomena found in rare cell separation processes. Non-Newtonian behavior of blood caused by the particulate nature of blood cells can significantly change the viscosity of the microenvironment inside the microchannel and affect the performance of the blood-handling devices. There are also methods using the lattice Boltzmann model, [78] or the moving particle semi-implicit (MPS)

model, to study the motion of blood cells, [79] but they are usually limited in the required high computational power and the number of cells can be analyzed (typically fewer than 100). We propose to construct a hybrid mathematical model to describe the change of the local microenvironment due to nonlinear mechanical motions of blood cells, and evaluate the efficacy of the immunomagnetic rare cell separation process. [80]

### 2.2.1 Blood sedimentation model

Blood consists of blood plasma and hematocyte cells, including red blood cells (RBCs), white blood cells (WBCs) and platelets. Among all, RBCs make up about 40% of the blood's volume. Thus, blood has to be treated as a non-Newtonian fluid. To study the relation between microenvironment and CTCs detection, we first construct a theoretical model to simulate RBCs sedimentation. As is shown in Figure 2.3, we divide the flow space into multiple cubic control volumes. The flow vector ( $V_{med}$ ) of the medium, RBC sedimentation velocity ( $\Delta v_{RBC}$ ), and volume RBC rate ( $\rho_{RBC}$ ) are defined for each control volume.  $\Delta v_{RBC}$  is defined as an average, relative velocity to the medium and is defined only in the direction of gravity. RBCs transport between adjacent control volumes for each time step is calculated based on these three parameters.

On the basis of the model described above, we develop a procedure to calculate the behavior of RBCs in the microfluidic flows. First, we calculate the flow field of the medium using finite element analysis software

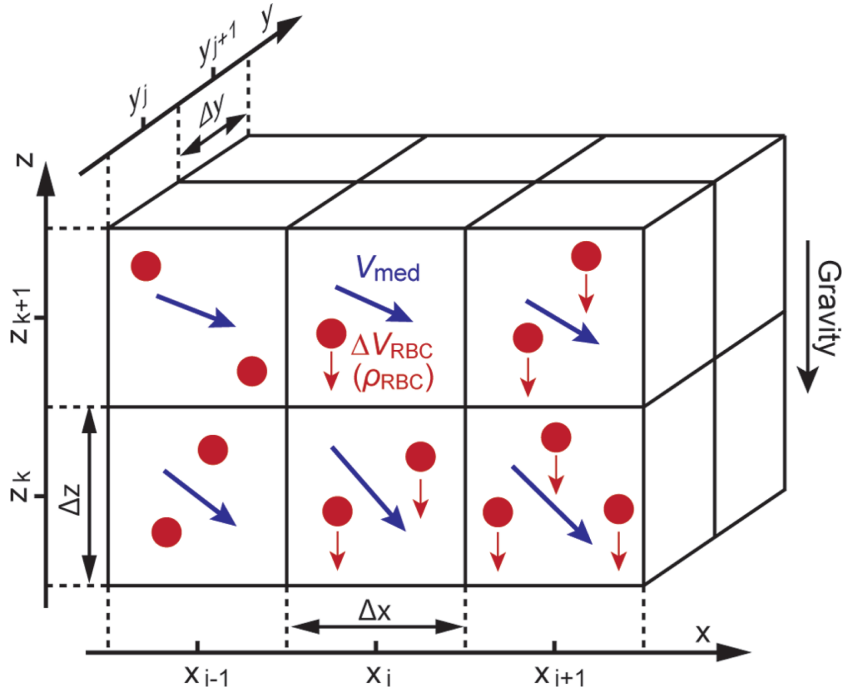


Figure 2.3: Red blood cell sedimentation model. RBC sedimentation in each control volume is given as a relative velocity  $\Delta v_{RBC}$  of the RBCs to the medium and is expressed as a function of the volume RBC rate  $\rho_{RBC}$ .

*COMSOL*, and then segment the flow field into the same control volumes. We assume the macroscopic medium flow  $V_{med,u}$  ( $u = x, y, z$ ) is not affected by the RBCs motion. For each time step, the local volume RBC rate is updated using the RBCs flux from neighboring control volumes. The RBC flux is calculated based on the volume RBCs rate and RBCs flow velocity, which is given as the summation of medium flow velocity and the average sedimentation velocity  $\Delta V_{RBC}$  of RBCs relative to the medium.  $\Delta V_{RBC}$  is a function of  $\rho_{RBC}$  and is only considered in the  $z$ -direction. The absolute velocity of RBCs can be expressed as:

$$\begin{aligned}
v_{RBC,x} &= v_{med,x} \\
v_{RBC,y} &= v_{med,y} \\
v_{RBC,z} &= v_{med,z} + \Delta v_{RBC}(\rho_{RBC})
\end{aligned} \tag{2.14}$$

Consequently, the RBCs flux  $\Phi_u(u = x, y, z)$  at an interface between neighboring control volumes is expressed as:

$$\Phi_u = \rho_{RBC} \cdot v_{RBC,u} + D \cdot \frac{\partial \rho_{RBC}}{\partial u} \quad (u = x, y, z) \tag{2.15}$$

Here  $D$  is the diffusion constant. If we estimate the value of  $D$  by the Einstein-Stoke equation

$$D = \frac{K_B T}{6\pi\eta R_{RBC}} \tag{2.16}$$

where  $K_B = 1.38 \times 10^{-23} \text{kg} \cdot \text{m}^2 \cdot \text{s}^{-2} \cdot \text{K}^{-1}$  is the Boltzmann constant,  $T = 300\text{K}$  is the absolute temperature,  $\eta \approx 5 \times 10^{-3} \text{Pa}\cdot\text{s}$  is the medium viscosity and  $R_{RBC} \approx 5 \times 10^{-6} \text{m}$  is the radius of the sphere particle. Given the typical height of the channel is  $500 \mu\text{m}$ ,  $\rho_{RBC} \approx 0.5$ ,  $V_{RBC,u} \approx 10 \times 10^{-6} \text{m/s}$ , the two terms in Equation 2.15 are estimated to be

$$\rho_{RBC} \cdot V_{RBC,u} \approx 5 \times 10^{-6} \text{m/s} \tag{2.17}$$

$$D \frac{\partial \rho_{RBC}}{\partial u} \approx 9 \times 10^{-12} \text{m/s} \tag{2.18}$$

The diffusion term is much less than the flux term, so we neglect the diffusion term in the following calculations.

Then we define  $\Delta\rho_{RBC}$  as the change of the volume RBC rate in a control volume  $\Delta x\Delta y\Delta z$  at a step time  $t \rightarrow t + \Delta t$ , it satisfies

$$\Delta\rho_{RBC}\Delta x\Delta y\Delta z = (\Phi_x^+ - \Phi_x^-) \cdot \Delta y\Delta z\Delta t + (\Phi_y^+ - \Phi_y^-) \cdot \Delta x\Delta z\Delta t + (\Phi_z^+ - \Phi_z^-) \cdot \Delta x\Delta y\Delta t \quad (2.19)$$

Where  $\Phi_u^+, \Phi_u^-$  ( $u = x, y, z$ ) stands for the flux in and flux out at  $u = u_i - (\Delta u/2)$  and  $u = u_i + (\Delta u/2)$  ( $u = x, y, z$ ). Thus, the volume RBC rate of each control volume can be instantly updated using the following equation

$$\rho_{RBC}(t + \Delta t) = \rho_{RBC}(t) + \frac{\Phi_x^+ - \Phi_x^-}{\Delta x} \cdot \Delta t + \frac{\Phi_y^+ - \Phi_y^-}{\Delta y} \cdot \Delta t + \frac{\Phi_z^+ - \Phi_z^-}{\Delta z} \cdot \Delta t \quad (2.20)$$

### 2.2.2 Partial viscosity model

To address the impact of the local viscosity change due to RBCs sedimentation on rare cell detection, we build a partial viscosity model. The model considers that the viscous force acting on a rare cell is the vector summation of partial viscous forces from the medium and the RBCs, each of them works in the same direction as its respective relative velocity to the cells. This is an expanded interpretation of the Einstein's viscos model, in which viscosity is considered to be linearly correlated to the volume rate of particles. [81]

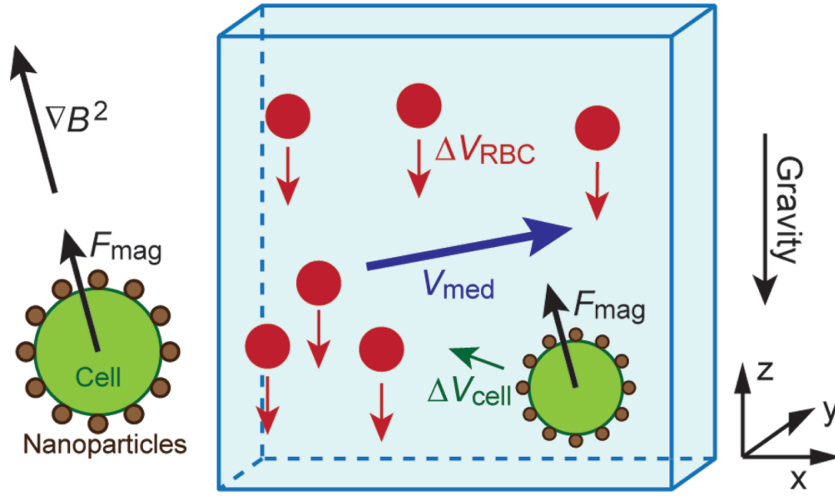


Figure 2.4: Partial viscos model: viscos force acting on a rare cell is the vector summation of the viscos force from the medium and the RBCs, each works in the same direction as its respective relative velocity.

To describe the extra viscous force from the RBCs, we introduce a term - partial viscosity  $\Delta\rho_{RBC}$ , as a function of the volume RBCs rate  $\rho_{RBC}$ . The partial viscosity  $\Delta\rho_{RBC}$  represents the contribution of viscous force from RBCs, which has an independent flow vector  $V_{RBC} = V_{med} + \Delta V_{RBC}$  different from the medium flow vector  $V_{med}$ . The expression of drag force in Equation 2.7 needs to be modified to:

$$F_{drag} = 6\pi R_{cell} \Delta v_{cell} \cdot \eta_{med} + 6\pi R_{cell} (\Delta v_{cell} - \Delta v_{RBC}) \cdot \Delta \eta_{RBC}(\rho_{RBC}) \quad (2.21)$$

### 2.2.3 Target cell tracking algorithm

We touched a little about the algorithm of tracking the target cells in Section 2.1.2, here we elaborate the procedure of calculating the trajectories

of the rare cells that are separated from blood.

Under the quasi-static motion assumption, now with the modified drag force expression considering the partial viscous force from RBCs, we can calculate the instant relative velocity of the target cells as:

$$\Delta v_{cell} = \frac{F_{mag} + 6\pi R_{cell} \Delta v_{RBC} \Delta \eta_{RBC}}{6\pi R_{cell} \cdot (\eta_{med} + \Delta \eta_{RBC})} \quad (2.22)$$

Thus, the absolute velocity of the cell is given as the vector summation of the medium flow velocity and the relative velocity:

$$\vec{v}_{cell} = \vec{v}_{med} + \Delta \vec{v}_{cell} \quad (2.23)$$

For each step time  $t \rightarrow t + \Delta t$ , the position of the cell can be updated based on the previous position and the instant velocity

$$\begin{aligned} x(t + \Delta t) &= x(t) + \vec{v}_x \cdot \Delta t \\ y(t + \Delta t) &= y(t) + \vec{v}_y \cdot \Delta t \\ z(t + \Delta t) &= z(t) + \vec{v}_z \cdot \Delta t \end{aligned} \quad (2.24)$$

### 2.3 Microscale magnetic field modulation

Two important factors associated with immunomagnetic assay include the capture rate, which indicates the sensitivity of the system, and distributions of target cells after capture, which impact the cell integrity and

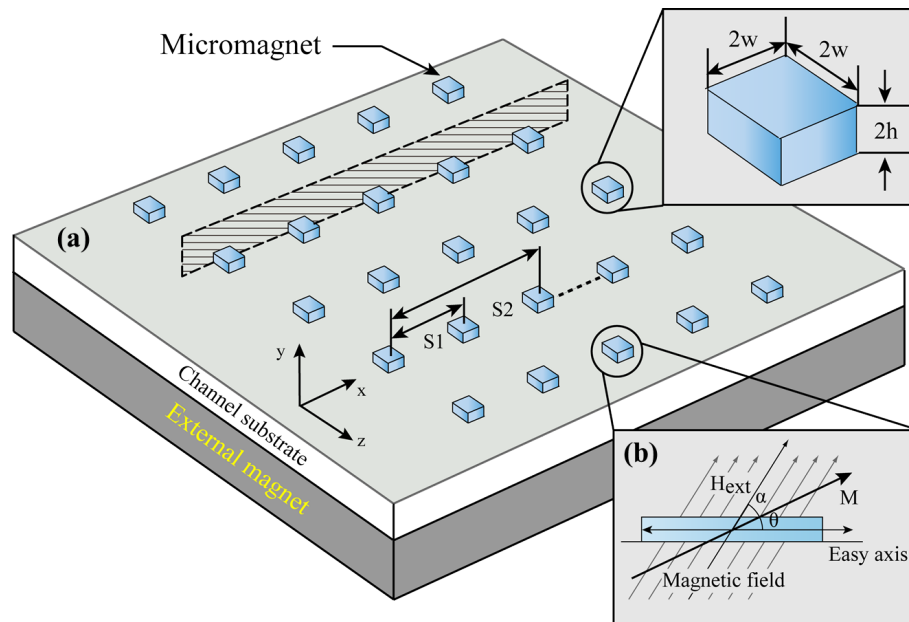


Figure 2.5: Schematic of the patterned thin film micromagnet design and magnetization. (a) Patterned thin film micromagnets are integrated on the substrate and magnetized by the permanent magnets. (b) Magnetization process of the soft-magnetic micromagnets using the theory of magnetic anisotropy and demagnetizing field.

other biological properties that are critical to downstream analyses. However, in a conventional magnetic activated system, the efficacy of the magnetic field generated by permanent magnets (usually on the scale of centimeters or millimeters) is limited by the low value of the magnetic field gradient and the low density of traps. Consequently, the target cells tend to be captured and aggregated in a confined area. The aggregation may directly impact the structural integrity of cells or quench the fluorescent signals from the target cells, all of which may interfere with cell identifying and profiling and weaken the strength of the immunomagnetic assay.

Here, we present a theoretical framework of implementing a microscale magnetic structures to modulate the local magnetic field toward enhanced capture and distribution of rare cancer cells. Through the design of a two-dimensional micromagnet array, we characterize the magnetic field generation and quantify the impact of micromagnets on rare cell separation.

### 2.3.1 Micromagnet magnetization

Figure 2.5(a) illustrates the concept of the thin-film micromagnet approach. Ferromagnetic coatings (such as nickel, iron and cobalt) are integrated on the substrate of a microchannel. The geometries and layouts of the micromagnet array can be defined using microfabrication techniques such as photolithography. The entire device is placed on top of a permanent magnets array. After being magnetized by the external magnetic field, the ferromagnetic element generates strong localized field to increase the magnetic force applied on the target cells.

The magnetization process of soft magnetic materials has been well established using the concept of magnetic anisotropy and demagnetizing field, as is shown in Figure 2.5(b). [82] Briefly, upon application of an external magnetic field ( $\vec{H}_{ext}$ ) with an angle ( $\alpha$ ) to the net magnetization  $\vec{M}$  of the sample,  $\vec{M}$  is rotated by the torque exerted by  $\vec{H}_{ext}$  with an angle ( $\theta$ ) from the equilibrium direction, which is usually the long axis. In a permanent magnet analysis, for magnetic structure with large aspect ratio (our case  $20 \mu m:200 nm=100:1$ ), shape anisotropy plays a dominate role in the magnetization

process. Therefore, the assumption  $\theta = 0$  is made to simplify the calculation, and only magnetization along the long axis is considered. We incorporate the magnetic anisotropy theory to describe the in-plane magnetization process to fit in our thin-film structure.

### 2.3.2 Micromagnet theoretical characterization

To quantify the strength of the micromagnets, we adopt an analytical model to describe the magnetic field generated by soft magnetic structure with rectangular shape. [83] In a simplified two-dimensional model (as shown in Figure 2.6(a)), a rectangular element (width  $2 \times w$ , height  $2 \times h$ ) centering with respect to the origin in the x-y plane is magnetized by an external magnetic field  $\vec{H}_{ext}$ . Assuming  $\vec{H}_{ext}$  is strong enough to magnetize the micromagnet to saturation ( $\vec{M} = \vec{M}_{es}$ ,  $\vec{M}_{es}$  is the saturation magnetization of the material) along the X direction, the magnetic field generated by this soft magnetic element can be calculated using:

$$B_x = \frac{M_{es}\mu_0}{2\pi} \left\{ \tan^{-1} \left[ \frac{2w(-y+h)}{(-y+h)^2 + x^2 - w^2} \right] - \tan^{-1} \left[ \frac{2w(-y-h)}{(-y-h)^2 + x^2 - w^2} \right] \right\} \quad (2.25)$$

$$B_y = \frac{M_{es}\mu_0}{4\pi} \left\{ \ln \left[ \frac{(-y+h)^2 + (x-w)^2}{(-y+h)^2 + (x+w)^2} \right] - \ln \left[ \frac{(-y-h)^2 + (x-w)^2}{(-y-h)^2 + (x+w)^2} \right] \right\} \quad (2.26)$$

Please note that we modified the magnetization direction and geometry notations from the original model in order to be consistent with the

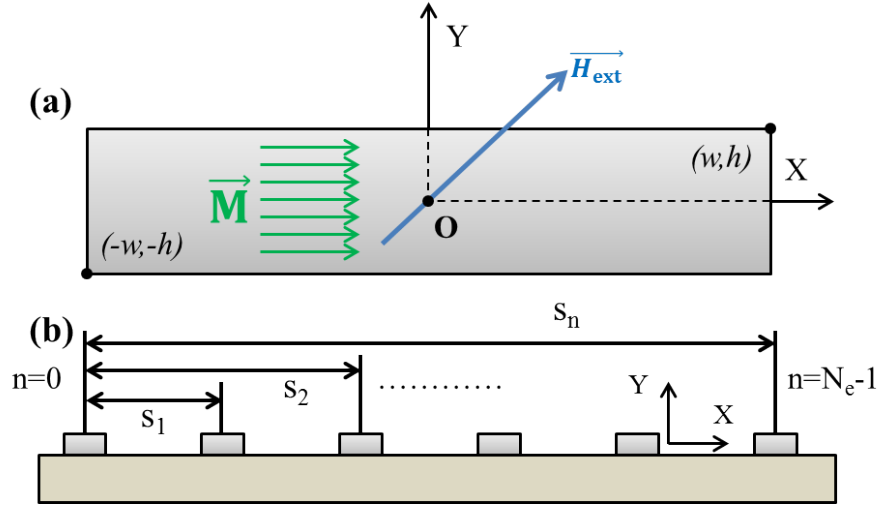


Figure 2.6: Analytical models to calculate the magnetic field generated by the thin-film micromagnets. (a) a single micromagnet element magnetized along the long axis. (b) an array of micromagnet elements aligned linearly on the substrate.

conditions in our design.

Equation 2.25, 2.26 can be used to calculate the magnetic field generated by a single micromagnet. For an array of micromagnets, the total magnetic field can be computed based on super-position theory. The total magnetic field is simply the linear summation of magnetic field generated by each micromagnet within a certain range. Consider an array of  $N_e$  elements (indexed with  $n = 0, 1, 2, 3, \dots, N_e-1$ ) with the first element centered with respect to the origin, and all the other micromagnets linearly positioned along the x-axis with distance  $s_n$  to the first element as illustrated in Figure 2.6(b). Please note that Figure 2.6(b) is essentially the cross-section shown in Figure 2.5(a). The  $n^{\text{th}}$  element is centered at  $x = s_n$  on the x-axis, whose

magnetic field can be calculated by shifting the coordinate system used in the  $0^{th}$  component as follows:

$$B_x^{(n)}(x, y) = B_x^{(0)}(x - s_n, y) \quad (2.27)$$

$$B_y^{(n)}(x, y) = B_y^{(0)}(x - s_n, y) \quad (2.28)$$

Eventually, the total field of the element array can be obtained by adding up the field components from all the micromagnet elements:

$$B_x = \sum_{n=0}^{N_e-1} B_x(x - s_n, y) \quad (2.29)$$

$$B_y = \sum_{n=0}^{N_e-1} B_y(x - s_n, y) \quad (2.30)$$

### 2.3.3 Effect of micromagnet on CTC detection

In order to investigate the influence of the micromagnets on the separation of rare cells, we incorporate the micromagnets into a simplified 2D model representing the microchip based immunomagnetic assay, as shown in Figure 2.7(a). The dimensions of the model are identical to those of the real device (channel height = 500  $\mu m$ , width = 17  $mm$ , length = 30  $mm$ ). Cells are released from one side of the channel, with initial positions uniformly aligned from the bottom to the top of the microchannel. Flow field inside

the microchannel follows a standard parabolic flow profile. The magnetic field inside the microchannel is calculated using FEM simulation software (shown in Figure 2.7(b)).

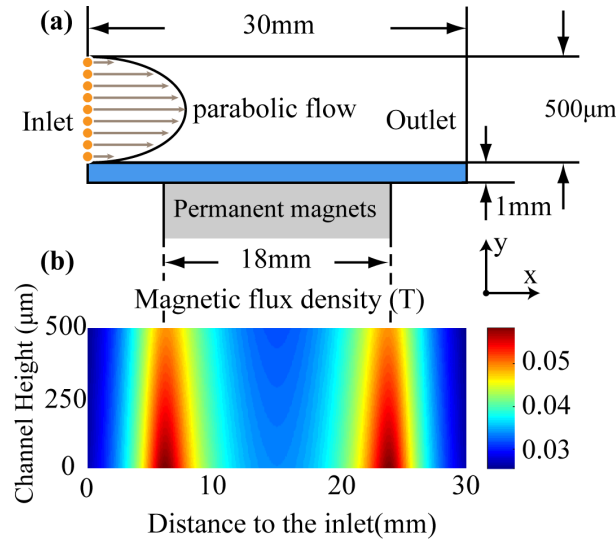


Figure 2.7: Analytical model of the microchip based immunomagnetic assay. (a) 2D model represents the microchip for rare cells detection. Liquid flow inside the channel follows standard parabolic profile. Permanent magnets are placed below the channel for attraction. (b) Magnetic field inside the microchannel generated by the permanent magnets.

To obtain the final locations of the captured cells and study the distribution, we divide the motion of the target cells into two stages - (i) in free space, and (ii) on solid surface after hitting the channel substrate. In the first stage, permanent magnets provide the primary long-range attraction. Motions of the cells can be calculated based on the algorithm in Section 2.2.3. In the second stage, cells continue moving under the combined influence of the permanent magnets and micromagnets. To determine the final capture

locations, we set up the criteria that if the value of the velocity perpendicular to the substrate  $|\vec{v}_y|$  becomes larger than the component parallel to the substrate  $|\vec{v}_x|$  with a factor  $\lambda$ , the cells are fully stopped because the forces on the cells tend to stop them more than pushing forward.

$$|\vec{v}_y| > \lambda \cdot |\vec{v}_x| \quad (2.31)$$

Otherwise, the cells keep moving on the substrate until the condition in Equation 2.31 is met. [84]

## 2.4 Summary

In this chapter, we first introduced the general physics of magnetic separation and its scaling law, which help us identify two important parameters that directly affect the performance of the immunomagnetic assay - the viscosity of the micro-environment ( $\eta$ ) and the magnetic field ( $B$ ). Then we presented the algorithms for red blood cell sedimentation, partial viscosity, and target cell tracking to address the relations between the micro-environment and immunomagnetic cell separation. In the third section, we present the micromagnet design as an approach to modulate the near-field magnetic field, with a detailed introduction of the magnetization principle and the method to calculate the magnetic field generated by the micromagnets. This chapter focuses on presenting the algorithms, and the simulation results are presented in Chapter 4.

## Chapter 3

### Micromagnet Design, Fabrication and Integration

In Chapter 2, we studied the immunomagnetic assay through theoretical simulations and proposed to adjust the viscosity ( $\eta$ ) and the magnetic field ( $B$ ) toward enhanced CTC separation. In Chapter 3, we present the technical approaches to fulfill these adjustments, including fabrication and implementation of the micromagnets, and incorporation of a motion-control module to manipulate the viscosity inside the screening system.

Specifically, we start with reviewing the current status of the research on micromagnets, with introductions of the micromagnetic field generation principles, micromagnet fabrication techniques, and related designs and applications. In the second section, we present two techniques, based on deposition and inkjet-printing technologies, respectively, to fabricate the micromagnets for CTC detection. In the end, we introduce the immunomagnetic screening system, which incorporates a motion control module to manipulate the viscosity distribution, and compare two permanent magnet configurations with distinct layouts.

### **3.1 Micromagnet overview**

The advantages of the micromagnet approach for CTC detection can be summarized into three aspects. First, the ferromagnetic micromagnets, after being magnetized, increase the near-field magnetic field and largely enhance the interactions between target cells and the magnetic field. It is expected to increase the high capture rate. Second, with carefully defined geometry and distribution, micromagnets rearrange the magnetic field in the microchannel, which can potentially help eliminate the aggregation issues (refer to Section 2.3) of the immunomagnetic assay. And third, while miniaturization improves the detection efficiency of the immunomagnetic assay, it lowers the system throughput. In contrast, considering the small size of the micromagnets, they can be easily implemented seamlessly without affecting other functional components or sacrificing the system throughput.

#### **Micromagnetic field generation**

There are two ways to induce the localized micromagnetic field: using micro-electromagnets [85–87] or static micromagnets. [88–90] For chip-scale implementations, the micro-electromagnets often involve the fabrication of 3-dimensional micro-coils on the planar substrate inside the microfluidic channel and the usage of an additional current source to actuate the coil and generate magnetic field. Using electromagnets, the intensity and distribution of the magnetic field can be easily tailored by controlling the actuation current. However, the external power source hinders the portability of the

entire system. Strength of the micro-electromagnet is also limited due to the relatively weak magnetic field and the heating issues.

In practice, the static magnetic approach is more widely adopted due to its simplicity in implementation. Soft magnetic materials can be directly integrated onto the substrate of the microchannel using conventional semiconductor fabrication techniques such as photolithography and deposition. [88, 89] Upon application of an external magnetic field, these ferro-micromagnets can be easily magnetized and generate localized magnetic field that is 100 times stronger than the magnetic fields generated by electromagnets. Besides, using strong permanent magnets (like the NdFeB magnet) as the magnetization field source, the entire device can be made compact.

### **Micromagnet fabrication**

Recent micromagnet fabrication technologies presented in the literatures include: 1) semiconductor fabrication techniques, which usually consist of photo-patterning using a photoresist to define the locations of the micromagnets. The micromagnet elements are integrated through techniques like sputtering, thermal deposition or electroplating, depending on the required size, thickness and resolution. [86–91] 2) Shrink induced micromagnets, in which Ni layer is deposited onto shape memory polymer films. Upon heating, the polymer film shrinks in lateral dimension, causing the Ni film to buckle and wrinkle and forming the micromagnets. [92] 3) Thermo-

magnetically patterned micromagnets, which use heat irradiation through a mask to selectively switch the magnetization direction of a thin film magnet and form an array of oppositely magnetized micromagnets. [93–95] 4) Ferromagnetic material encapsulation, in which PDMS is used to encapsulate ferromagnetic oxide powder into the master template made with SU-8. A micromagnet array is formed upon PDMS demolding from the master template. [96]

### **Micromagnet designs and applications**

Modulating magnetic field is critical in a variety of applications, such as cell proliferation regulating, [97] magnetic particle trapping and manipulating, [98–100], and chemical kinetic modulation. [101, 102] It usually associates with precise confinement of the magnitude and distribution of the magnetic field and gradient. As for separation purposes, several early studies have been reported on the integration of micromagnets with microfluidic systems, as summarized in Figure 3.1. Nickel micro-strips (Figure 3.1(a)) have been fabricated as magnetic conductive tracks to separate leukocytes from whole human blood. [84] Arrays of nickel posts (Figure 3.1(b)) are used in a microfiltration device to separate magnetic beads from non-magnetic beads. [103] Shrink-induced magnetic traps (Figure 3.1(c)) are used to extract DNA samples for qPCR studies. [92] Thermomagnetically patterned micromagnets (Figure 3.1(d)) are used to separate magnetic and non-magnetic micro-particles from a mixed solution. [93] We summarize the fabrication

principles, materials, micromagnet dimensions, capture range and applications in Table 3.1. Here, the capture range is the maximal distance away from the magnetic element where the targets can still be attracted by the micromagnets. Different targets are used in the demonstration experiments, to eliminate the impact of the variations of the targets and only compare the strength of the micromagnets, we estimate the magnetic gradient  $\nabla B^2$ . According to Equation 2.5, the magnetic gradient can be considered as a direct reflection of the magnetic force.

To combine the micromagnet with the immunomagnet CTC detection assay, the fundamental requirement is to enhance the local magnetic force to facilitate surface cell retention. Additionally, an appropriate micromagnet system should (1) minimize possible physical damages to the target cells inside the microchannel; (2) reduce the aggregation of cells and free nanoparticles to avoid fluorescent quenching; (3) provide retrievable cells after capture for subsequent cellular imaging and downstream molecular studies; and (4) have robust fabrication processes that can be scaled up for mass production.

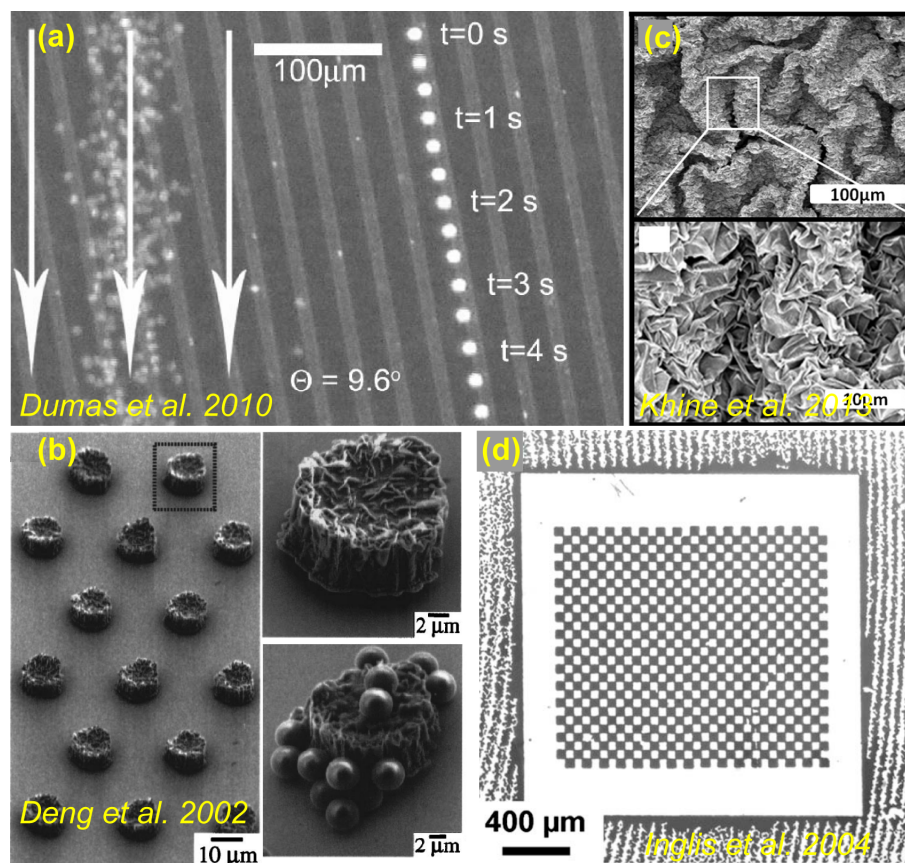


Figure 3.1: Micromagnet technologies used for cell separation. (a) Micromagnetic strips made with nickel. (b) Array of nickel micro-posts. (c) shrink-induced groove micromagnet. (d) Thermally patterned micromagnets.

Table 3.1: Micromagnet designs, fabrications, characteristics and applications

Structure	Fabrication	Materials	Dimension* ( $\mu m$ )	Magnetic <sup>†</sup> gradient ( $\nabla B^2$ )	Effective range ( $\mu m$ )	Applications
Strips	Etching, sputtering	Ni	10(w) $\times$ 2(t) 35 periodicity	50	10	Blood cells separation
Pillars	Photolithography, electrodeposition	Ni	15(w) $\times$ 7(t)	500	50	Microbeads
Chessboard	Laser irradiation, deposition	NdFeB	50~100(w) 1~2(t)	5	40~70	Microparticles
Grooves	Shrinking, deposition	Ni, polyolefin	20(t)	30	60~70	Microbeads, DNA extraction

\* In the dimension column, (t) stands for thickness, (w) indicates width.

† The unit of the magnetic field gradient is  $B^2/m$ .

### 3.2 Deposited thin-film micromagnets array

For rare cancer cell studies, the aforementioned micromagnet structures might not serve the purpose. Since the cancer cells are rather fragile, [18] the relative large thickness ( $>5 \mu\text{m}$ ) of the previous structures might cause physical damages to the cells due to collision. We pursue an ultra-thin structure with sub-micrometer thickness to minimize possible damages to the cells. Additionally, in the demonstrated applications using aforementioned micromagnets to sort targets with large sub-populations, such as white and red blood cells, [84] and magnetic and non-magnetic microbeads, [92, 93] separation efficiency is the major key parameter that matters. However, when it comes to rare cell studies, each captured target cell needs to be individually addressable, structurally distinguishable, fluorescently visible, and potentially retrievable to facilitate downstream analyses. It posts extra requirements on avoiding cell aggregation. Therefore, we adopt an array design, anticipating the array captures cells discretely, and provides a promising tool to generate better distribution of the captured CTCs.

To fabricate the thin-film micromagnets, the first technique we adopt is electron beam physical vapor deposition (EBPVD). EBPVD works by bombarding a target anode with an electron beam given off by a charged tungsten filament under high vacuum. The electron beam causes atoms from the target to transform into the gaseous phase. These atoms then precipitate into solid form, coating the substrate inside the vacuum chamber with a thin layer of the anode material.

### 3.2.1 Fabrication principle

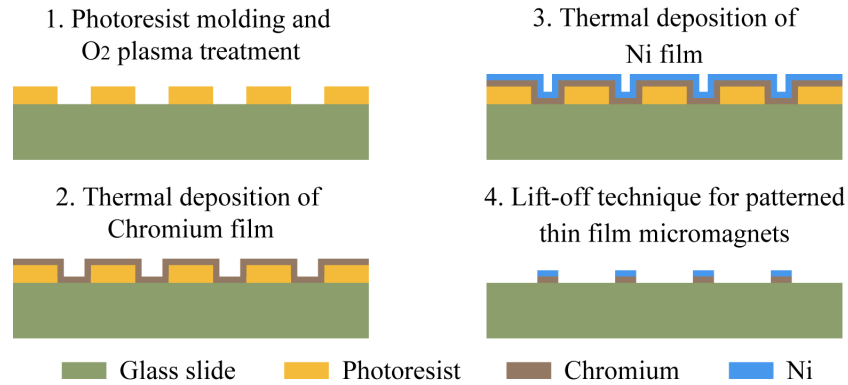


Figure 3.2: Fabrication process of the micromagnet using thermal deposition. Chromium is firstly deposited as adhesion layer, after which Nickel is deposited to form the magneti structure. At last, lift-off technique is used to remove the rest parts.

Figure 3.2 illustrates the micromagnet fabrication process using E-beam deposition. First, positive photoresist is spin-coated onto the standard glass slide. Patterns of the micromagnets are then photo-defined on photoresist by selective exposure to UV light through a photo-mask. The residual photoresist is removed with  $O_2$  plasma. Next, 15 *nm* chromium layer is thermally deposited as the adhesion layer, after which the nickel layer is deposited to form the magnetic structures with a thickness of 200 *nm*. In the final step, lift-off technique is used to remove the photoresist and leaving behind the micromagnet arrays. [104]

### 3.2.2 Fabrication results

The dimension of the fabricated micromagnet element is designed to be  $20\mu\text{m}\times 20\mu\text{m}$ , with a thickness of  $200\sim 250\text{ nm}$ . Figure 3.3 shows one example layout design of the micromagnet array. The periodicity of the micromagnet array varies between  $50\mu\text{m}$  and  $150\mu\text{m}$ . Figure 3.4 shows the SEM image of the fabricated micromagnet array, and the inset shows a zoomed-in view of a single micromagnet element.

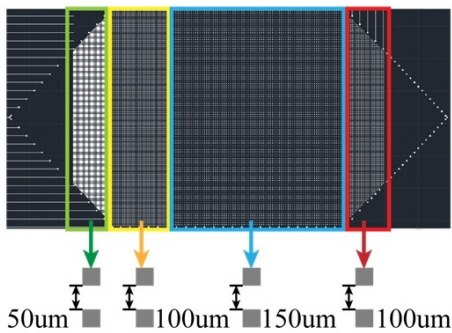


Figure 3.3: Design of the micromagnet array and key periodicity parameters.

To adapt the micromagnet towards different applications, the geometry needs to be carefully tailored. The lateral dimension determines the effective range of individual micromagnets. Larger the size, broader the area get affected. Using advanced fabrication techniques, such as E-beam lithography, the lateral dimension of the micromagnet can be even reduced down to nano-scale. However, given the size of the target CTCs ( $\sim 20\mu\text{m}$ ), nano-scale magnets are not strong enough to hold the cells. Thickness affects the system performance both hydrodynamically and magnetically. On one hand, in-channel structures can be used to disturb the hydrodynamic

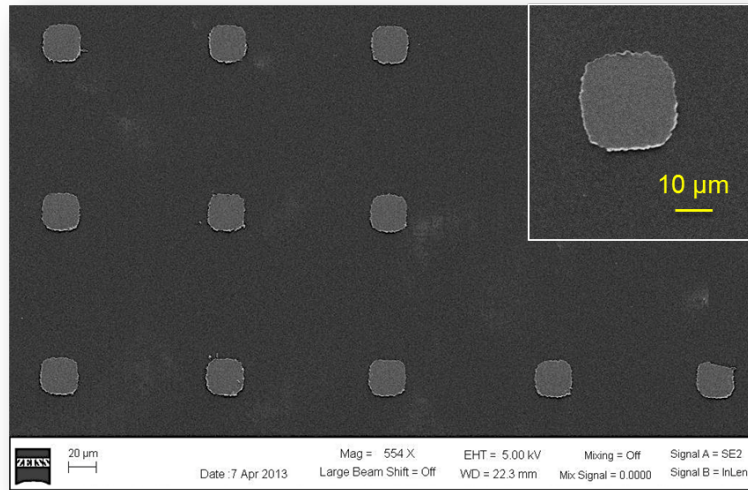


Figure 3.4: SEM image of the nickel micromagnets fabricated using e-beam deposition. Inset shows a zoom-in image.

flow in the channel, creating additional vertical flows as a micro-scale mixer, which increases the interactions between the cells and substrate for better capture. [39, 105] However, thick micromagnets increase the shear stress that might cause damages to the cells. On the other hand, thickness also determines the magnitude of the magnetic force and the working range of the micromagnets. As an array, the micromagnet spatial periodicity can be engineered to adjust the distribution of the captured CTCs. Appropriate spatial periodicity is mainly determined by the effective range of single micromagnet element. Beyond this value, cells are stagnated at the entrance of the micromagnet array. Whereas below this value, the chances of cells hitting a micromagnet on their trajectories become so low that the effect of the micromagnets can almost be neglected. These factors need to be well

balanced in searching for an optimum micromagnet design.

### 3.3 Inkjet printed micromagnets

During the cell screening experiments, we observe cancer cells being captured by the magnetic nanoparticles aggregated around the Ni micromagnets, as shown in Figure 3.5. The aggregation in fact increases the effective range of the micromagnets, and inspire us to directly pattern the magnetic nanoparticles on the substrate as surface magnetic flux sources.

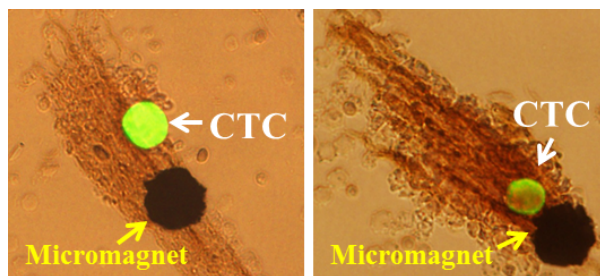


Figure 3.5: Observations of the CTCs being captured by the nanoparticles aggregated around the Ni micromagnet element.

Inkjet printing technology, widely used for hard-copy documents production and high definition photographic printing, is emerging as an alternative patterning technology to traditional photolithography that enables fabrication of two-dimensional or three-dimensional structures with sub-micrometer resolution. This technology is appealing in it being a non-contact, additive patterning and maskless approach. Versatile thin films can be directly written on the substrate, and the design can be easily modified from batch to batch. [106,107]

Inkjet printing technology has been applied in various fields such as electrochemical sensor, [108] biological nanodevices, [109] nanophotonic devices (photonic grating structures), [110, 111] and organic electronics. [112] It has also been used as a versatile patterning technique with cells, polymers [113], and magnetic materials. [114] The working process essentially involves the ejection of a fixed quantity of ink in a chamber, which is sensitive to external voltage, from a nozzle through a sudden, quasi-adiabatic reduction of the chamber volume via piezoelectric action. This sudden reduction sets up a shockwave in the ink, which causes a liquid to eject from the nozzle. The inks have to meet strict physicochemical properties (viscosity, surface tension, adhesion to a substrate etc.) to achieve optimal performance and reliability of the printing process. [115]

### 3.3.1 Fabrication principle

Figure 3.6 illustrates the work flow of using inkjet printing technology to fabricate the micromagnets. Magnetic nanoparticles (*fluidMAG-ARA* from *chemicell* with hydrodynamic diameter of 100 nm) are mixed with medium liquid (mixture of glycerol and water, with ratio of 3:4) of certain viscosity, surface tension to make the printing ink. Commercial inkjet material printer (*Fuji DMP-2800 Dimatrix Materials Printer*) is used to print the ink following a defined pattern on a standard glass slide (pre-heated 60°C). The volume of a single droplet is 10 pL. After printing, the glass is moved to a hot plate (pre-heated to 100°C) to evaporate the medium liquid. The magnetic

nanoparticles remain on the glass slide and self-assemble the micromagnet structures. Eventually, plasma-enhanced chemical vapor deposition (PECVD) is used to coat the entire structure with  $\text{SiO}_2$  (~10 nm) to protect the patterns against the blood flows inside the microchannel.

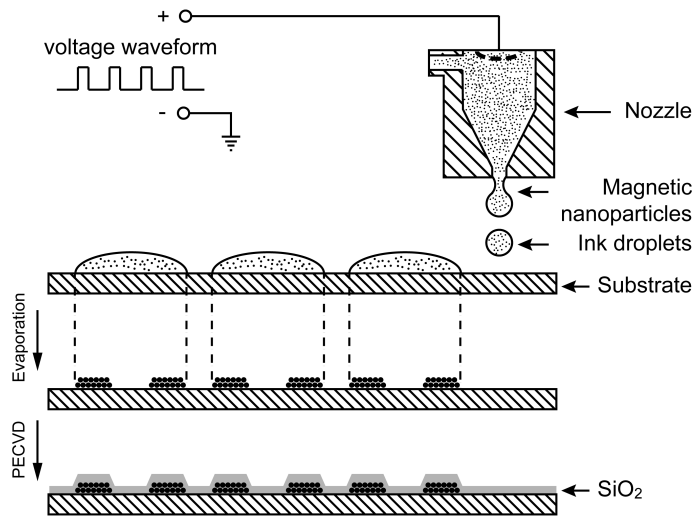


Figure 3.6: Fabricating micromagnets using inkjet printing technology. Ink mixed with magnetic nanoparticles are printed on the substrate following a defined pattern. The substrate is then heat up to evaporate the ink liquid, and the nanoparticles are left behind and self-assemble the magnetic patterns. Finally,  $\text{SiO}_2$  is deposited using PECVD as the protecting layer.

### 3.3.2 Fabrication results

Figure 3.7 shows the SEM images of the inkjet printed micromagnets, and the inset shows the zoom-in view of a printed pattern. The nanoparticles self-assemble into a “ring-shaped” structure. Most of the nanoparticles aggregate around the edges of the ring, and some nanoparticles are scattered

in the middle of the ring. The ring structure is formed because of the thermodynamics in the evaporation stage. The evaporation rate is higher at the edge than the center, which creates outward convective flow and brings the nanoparticles to the edge. [116,117]

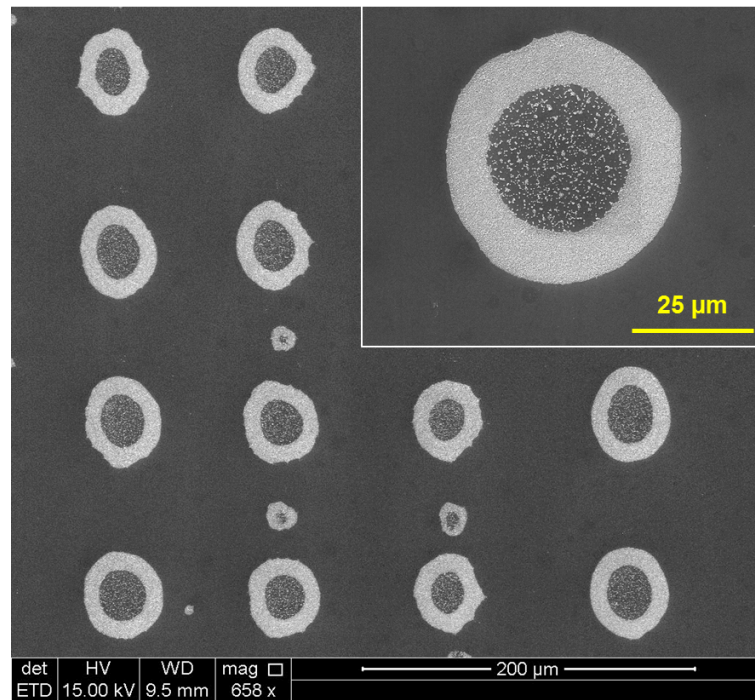


Figure 3.7: SEM image of the inkjet printed micromagnets. Inset shows the zoom-in view of the a printed pattern.

To calibrate the fabricated structure, we take images of the printed pattern using bright-field microscope and perform measurement with *ImageJ*. The outer diameter is determined to be  $48.5 \pm 3.5 \mu m$ , the inner diameter  $25.9 \pm 3.1 \mu m$ , and the width of the edge is  $11.2 \pm 1.3 \mu m$ . The size of one spot is determined by the volume of the droplet comes out of the nozzle. The

periodicity of the printed micromagnet array is measured to be  $150\ \mu\text{m}$ , and it can be set to any value below  $254\ \mu\text{m}$ , as limited by the printer. We also measure the printed pattern with AFM to obtain the morphological information. According to the results shown in Figure 3.8, the peak thickness at the edge is about  $300\ \text{nm}$ . AFM measurement also confirms the ring-shaped geometry we observe in the SEM images.

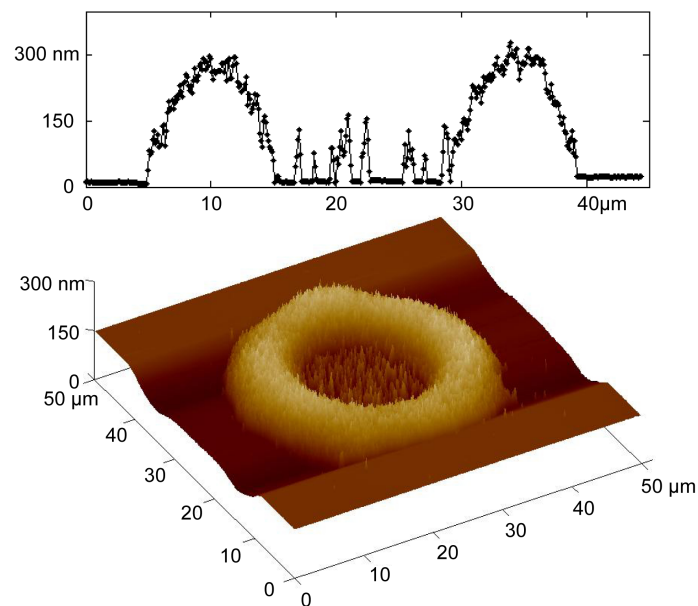


Figure 3.8: AFM measurement of the inkjet printed micromagnet pattern. The peak thickness of the pattern at the edge is  $\sim 300\ \text{nm}$ .

### 3.4 Screening system

As illustrated in Figure 3.9(a), the experiment apparatus consist of a hexagon microchannel (dimension:  $30\ \text{mm}$  in length,  $17\ \text{mm}$  in width, and  $500\ \mu\text{m}$  in height) made of PDMS using standard molding technique (Figure

3.9(b)), a glass slide (integrated with micromagnets) serving as the capture substrate, a reservoir to store the blood samples during the screening, a syringe pump to drive the blood, and three strong permanent magnets (NdFeB, grade N42) placed with alternating orientations to provide the high magnetic gradient. After the screening, the substrate can be peeled off from the PDMS chamber for cell identification and other studies. [48]

#### 3.4.1 Rotational screening stage

To manipulate the microenvironment, we build an automatic working stage with motion control system to dynamically change the orientation of the microchannel between “upright” and “inverted” during the screening processes. The system (shown in Figure 3.9(c)) consists of DC motors and optical position sensor, and is operated using a *LabView* program.

The inverted and upright orientations mainly differ in the relation between the directions of gravity and magnetic attraction (shown as arrows with  $\mathbf{G}$  and  $\mathbf{F}_{\text{mag}}$  in Figure 3.9(c)). In the upright case, gravity and magnetic force are in the same direction. The RBCs, though not affected by the magnetic field, settle down on the capture surface due to gravity-induced sedimentation. As a result, the capture surface is covered by a thick layer of blood cells with high viscosity, which might prevent the CTCs being captured. In contrast, gravity and magnetic force are in opposite directions in the inverted orientation. RBCs tend to sediment to the opposite side of the microchannel, and flow out of the channel. Consequently, the local viscosity

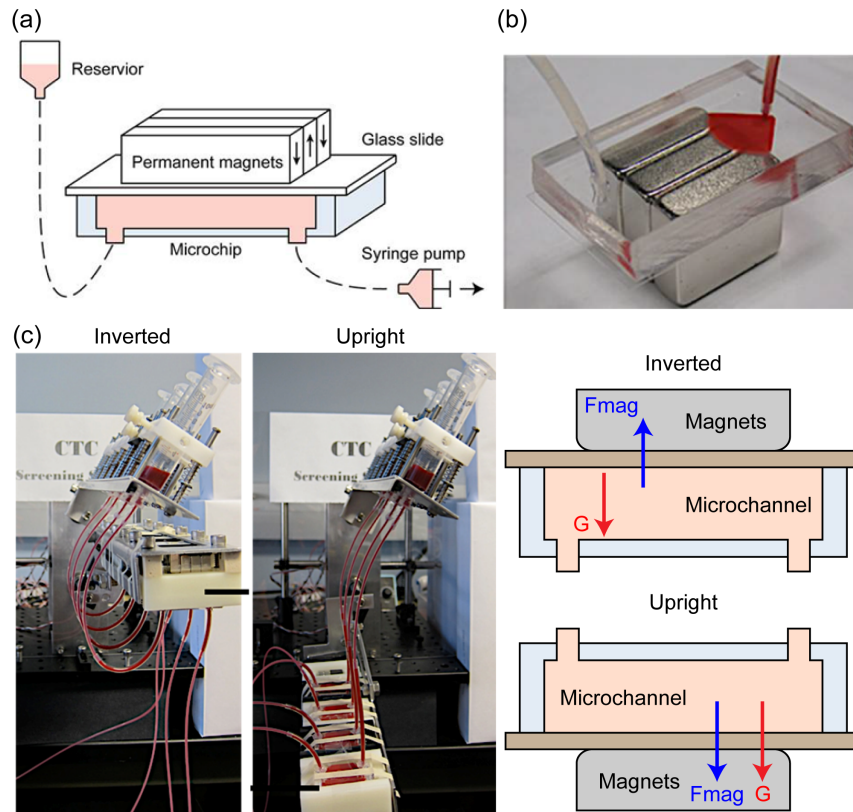


Figure 3.9: Rotational stage to control the orientations of the microchip during the screening process. Inverted orientation reduces the sedimentation layer on top of the capture plane, and facilitates the cell separation in the channel.

near the capture surface would be reduced. We anticipate that keeping the channel in the inverted orientation during the screening would significantly increase the capture rate of the immunomagnetic assay. The effects of this rotational stage will be first be investigated in the theoretical model and then verified through cell screening experiments.

### 3.4.2 Permanent magnet configuration

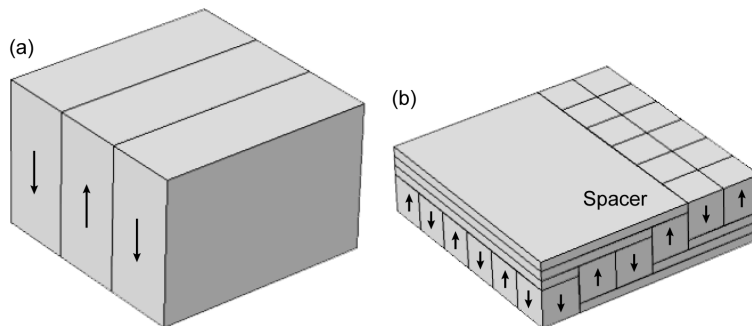


Figure 3.10: Two types of permanent magnet configurations. (a) Three parallel design. (b) 6×6 pixel array with inserted spacers.

The permanent magnet is an important part of the immunomagnetic assay. It provides the external magnetic field for the long-range magnetic attraction. In the meantime, it magnetizes the micromagnets inside the microchannel. Here, we compare two types of permanent magnet array configurations. Figure 3.10(a) shows the “three-parallel” design, consisting of three N42 Neodymium magnets ( $3/4 \times 1/4 \times 1/2$  inch, NB024, *Applied Magnets*) aligned with alternating polarization. It has been used in our previous demonstrations of the immunomagnetic CTC detection. [48] Figure 3.10(b) illustrates the “pixel” design, where thirty-six pieces of N48 Neodymium magnets ( $1/8$  inch cube, NB001-N48, *Applied Magnets*) assemble a 6×6 array with alternating polarizations. In addition, to reduce the magnetic field at the front part of the permanent magnet array, we insert non-magnetic spacers into the pixel array to increase the distance between the magnets and the substrate of the microchannel.

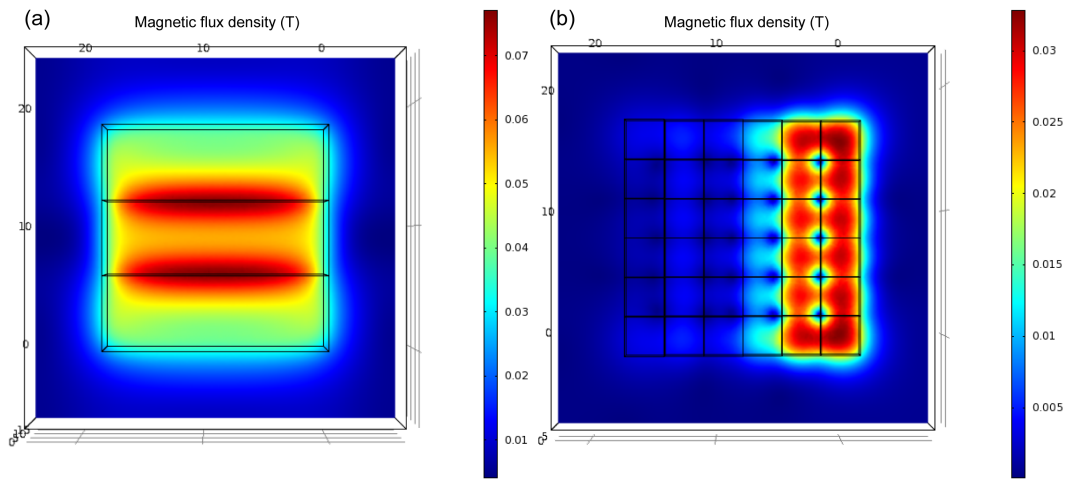


Figure 3.11: Magnetic field simulation results of the (a) three-parallel, and (b) pixel permanent magnet arrays.

We first examine the magnetic field generated by the two types of permanent magnet arrays using *COMSOL<sup>TM</sup>*. Figure 3.11(a) shows the magnetic flux density of the three-parallel design, and Figure 3.11(b) is the result of the pixel permanent magnet array. In the three-parallel design, the peak value of the magnetic flux density is  $\sim 0.07$  T, and it is at the boundary between neighboring magnets. While in the pixel design, the maximum value is  $\sim 0.03$  T, and it locates at the later part of the array, where there is no spacer. The three-parallel design generates a stronger magnetic field due to the relatively large size. However, the pixel design creates a smooth curve of a gradually increased magnetic field from the front to the later part of the array. When we place the permanent magnet array beneath the microchannel, the relatively weak magnetic field in the front part of the array allows the cells to migrate into the later part of the microchannel. This might help

alleviate the cell aggregation in the beginning part of the permanent magnet array.

Furthermore, we use the potential well theory to estimate the impact of the two types of permanent magnet configuration on CTC detection. A potential well is the region surrounding a local minimum of potential energy. Due to entropy, an object tends to stay in the potential well. It can also be used to explain magnetic cell separation. Consider an object of volume  $V$  with a fixed magnetization  $\mathbf{M}$ . It possesses a magneto-static self-energy that is given by:

$$W_s = \frac{\mu_0}{2} \int_V \mathbf{M} \cdot \mathbf{H}_M dv \quad (3.1)$$

where  $\mathbf{H}_M$  is the field in the object due to  $\mathbf{M}$ . If a magnetized object is subject to an applied field  $\mathbf{H}_a$ , it acquires a potential energy:

$$W_a = -\mu_0 \int_V \mathbf{M} \cdot \mathbf{H}_a dv \quad (3.2)$$

This potential energy can be viewed as the work required to move the specimen from an environment with zero field to a region permeated by  $\mathbf{H}_a$ . Equation (3.2) can be used to calculate the force or torque imparted to a magnetized body by an external field. [118]

Now we consider the model of a cell labeled with magnetic nanoparticles in an external magnetic field. Due to the small size of a cell, the variation

the magnetic field applied on the cell can be neglected. The potential energy can be simplified to:

$$W_a = -\mu_0 VMH_a \cos(\theta) \quad (3.3)$$

Here  $\theta$  is the angle between  $\mathbf{M}$  and  $\mathbf{H}_a$ . The magnetization  $\mathbf{M}$  is dependent on the applied magnetic field  $\mathbf{H}_a$  and the volume magnetic susceptibility  $\chi_m$  of the material, given as:

$$\mathbf{M} = \chi_m \mathbf{H}_a \quad (3.4)$$

Substitute Equation (3.4) into (3.3), the potential energy now can be expressed as:

$$W_a = -\mu_0 V \chi_m \cdot H_a^2 \quad (3.5)$$

Given that  $\mu_0$ ,  $V$ ,  $\chi_m$  are all constants for the same type of cell and nanoparticle, the potential energy is totally determined by the intensity of the magnetic field  $H_a$  generated by the permanent magnets. Substitute the expression of the effective magnetic susceptibility of the cell (Equation 2.10), we get the final expression of the magnetic potential energy of the cell as:

$$W_a = -\frac{4}{3} \mu_0 \pi N R_p^3 \chi_p \cdot H_a^2 \quad (3.6)$$

The magnetic permeability  $\mu_0 = 4\pi \times 10^{-7} H \cdot m^{-1}$ , and we assume the radius of the nanoparticle is  $R_p = 50nm$ , and the volume susceptibility of the nanoparticle is  $\chi_p = 5$  (SI unit), and number of labeled nanoparticles is  $N = 2500$ . [48]

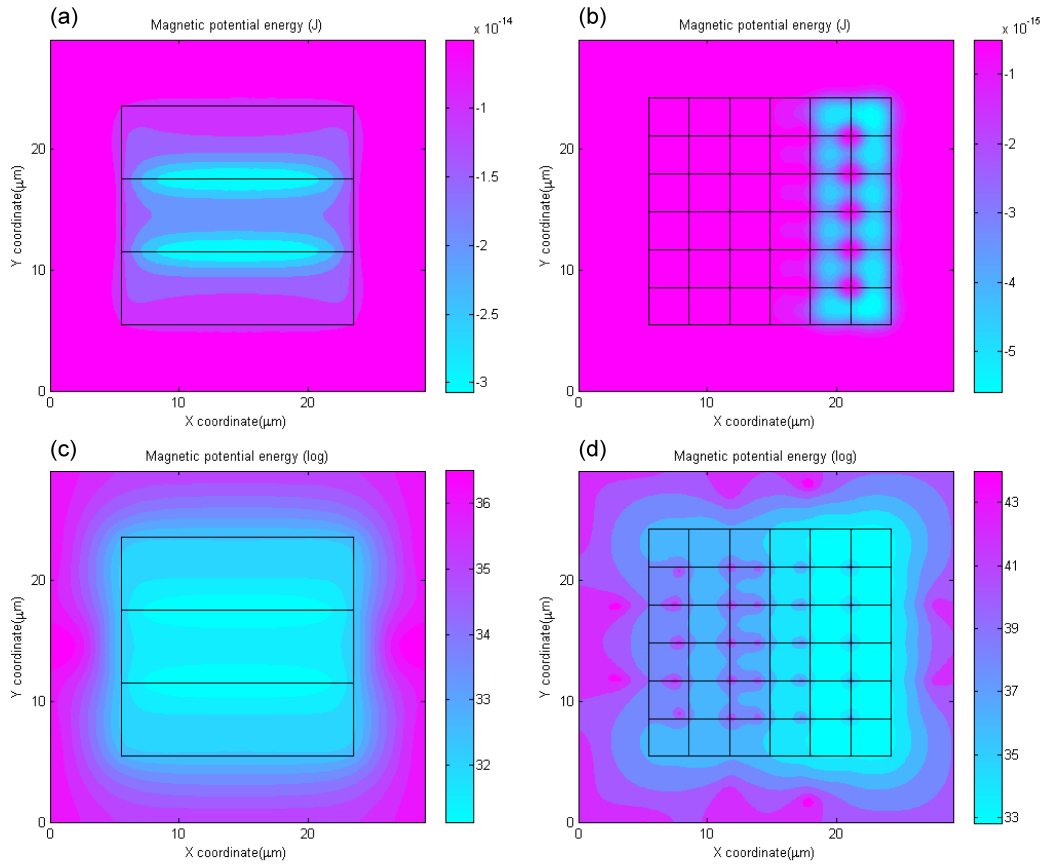


Figure 3.12: Magnetic potential energy of target cells in (a) three-parallel, (b) pixel permanent magnet array. The logarithmic value of the magnetic potential energy in (c) three-parallel, (d) pixel permanent magnet array.

Figure 3.12(a) and (b) show the original values of the magnetic potential energy of target cells in three-parallel and pixel permanent magnet

array, respectively. The blue color indicates a relatively low magnetic potential energy. The results match the magnetic field simulation results well. In the three-parallel configuration, the boundaries between neighboring magnets have deep potential wells, while for the pixel design, the deep potential wells lie in the later part of the array. At these deep potential wells, the target cells are subject to stronger magnetic forces.

Due to the large variance in potential energy, the front part of the array is saturated, as shown in Figure 3.12(b). To clarify the potential energy distribution in the front part, we take a logarithmic calculation of the energy, and the results are shown in Figure 3.12(c) and (d) for three-parallel and pixel permanent magnet array separately. The three-parallel design works as a single, large potential well that generates attractive forces starting at the front edge of the array. In contrast, the pixel layout displays weak but scattered potential wells in the front half array due to the spacers. In the meantime, the pixel array shows enhanced potential well toward the end of the array, which guarantees that any target cells that might escape from the front part can be captured before flowing out of the channel.

Generally, the pixel permanent magnet layout is advantageous over the three-parallel configuration. First, the insertion of the spacer significantly reduces the magnetic field at the front part of the array, which helps prevent the cell aggregation at the front edge of the permanent magnets. Second, the small magnets create scattered magnetic potential wells that can further distribute the target cells when they are captured. Third, the

strong magnetic field at the end of the pixel array works as a secure system to guarantee a capture rate comparable to that of the three-parallel layout. Experimental results using the two types of permanent magnet arrays will be presented and evaluated in Chapter 4.

### **3.5 Summary**

In this chapter, we first reviewed the current development of micro-magnet technologies and analyzed their limitations in rare cell separation applications. Then we introduced two technical approaches to fabricate the thin-film micromagnets based on e-beam deposition and inkjet printing technology that can potentially improve the detection sensitivity and distribution pattern of captured cells; both are critical to the immunomagnetic assay. Related fabrication principles and characterization results are presented. In the third section, we introduced the major components of the CTC screening system, with focus on the screening stage that can change the orientation of the microchip and manipulate the local viscosity inside the channel to enhance the separation efficiency. Last but not least, we presented two types of permanent magnet configurations and discussed their pros and cons for CTC detections.

# Chapter 4

## Results and Discussions

In this chapter, we introduce both the theoretical and experimental results related to the micro-environment analysis and the micromagnet implementation.

In the micro-environment analysis section, we first present the results of the blood characterization experiments, which help define the relationships among the blood volume rate, sedimentation rate, and viscosity. Then we describe the results of the blood sedimentation and the cell tracking models. In order to evaluate the significance of our analytical models, we perform simulations of CTC separation under different conditions and carry out screening experiments to verify the simulation results.

For the micromagnets, we start with characterizing the magnetic field generation and quantify its impact on rare cell separation through a two-dimensional micromagnet array model. Then we present the screening experiment results using the Ni micromagnet and inkjet-printed micromagnet separately with cultured cancer cells and clinical samples.

## 4.1 Figures of merit

The experiment protocol has been well established. [64] Briefly, the blood sample, spiked with cancer cells, is mixed with magnetic nanoparticles (*Ferrofluid<sup>TM</sup>*, *Veridex*, *Johnson& Johnson*) that are pre-functionalized with cancer specific antibody (anti-epithelial cell adhesion molecule, anti-EpCAM). The CTCs bind actively to the nanoparticles in the blood, and are collected by the immunomagnetic assay when pumped through the microchannel.

To evaluate the performance of the system, we define a parameter “capture rate” as follows - two control slides are prepared from the same cell suspension and at the same time the cells are spiked. Same amount of cell suspension is dropped, dried, stained and counted. Capture rate is the ratio between the number of CTCs found from the screening slide and the average number of cell found on the two control slides.

To characterize the efficiency of the optimized immunomagnetic assay, we carry out experiments with four cancer cell lines - colon cancer (COLO 205), prostate cancer (PC3), and breast cancer (SK-BR-3, MCF-7). We select these cell lines first because colon, prostate, and breast cancers are the three leading lethal cancer types for human beings. [1] More importantly, they have different expression levels of EpCAM, especially PC3 has far less compared with other cell lines. [67] Tests with multiple cell lines would demonstrate the versatility of the system, and provide more robust conclusions.

CTCs are identified through immuno-fluorescent staining and imaging. After screening, the slides are stained with anti-cytokeratin (480 nm/ 535 nm, CK, protein found in epithelial tissue, positive test, mouse anti-cytokeratin, pan-FITC, Sigma- Aldrich, St Louis, MO), anti-CD45 (535 nm/ 610 nm, found on leukocytes, negative test, AlexaFluor 568, Invitrogen, Carlsbad, CA, bound to mouse anti-human clone 9.1 made in University of Texas Southwestern Medical Center), and DAPI (350 nm/ 460 nm, stains DNA found in cell nucleus, positive test, Vectashield Mounting Medium with DAPI, Vector Laboratories, Inc, Burlingame, CA). Figure 4.1 shows the fluorescent panel of a sample COLO205 cell and a white blood cell for comparison. COLO205 are CK+/ DAPI+/ CD45-, while WBC behaves differently CK-/ DAPI+/ CD45+. Other types of cancer cells (PC3, SK-BR-3, and MCF-7) exhibit similar fluorescent signals to COLO205.

## 4.2 Micro-environment analysis and CTC detection

### 4.2.1 Blood characteristics measurement

To address the relationship between the RBCs sedimentation rate ( $\Delta v_{RBC}$ ) and the volume rate of RBCs ( $\rho_{RBC}$ ), we perform a simple measurement using a capillary tube to simulate a microhematocrit tube, as illustrated in Figure 4.2. RBCs suspended at a volume density of  $\rho_{RBC}$  are kept in the tube. After a certain amount of time, blood in the tube displays four layers, supernatant, diffusion, main suspension, and settling layer. The sedimentation velocity  $\Delta V_{RBC}$  is defined as the growth rate of the sedimentation length

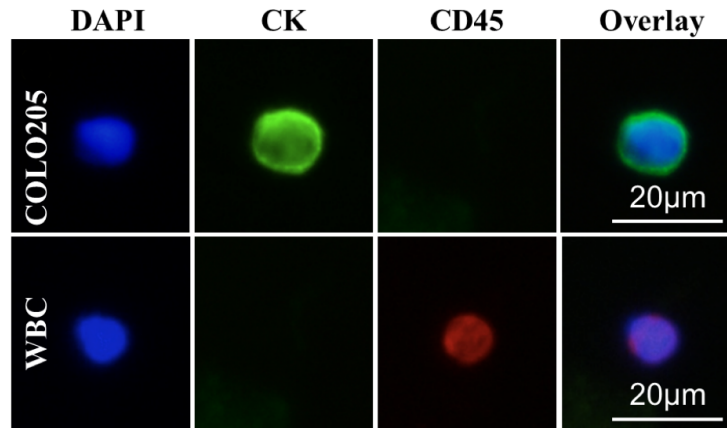


Figure 4.1: Fluorescent panel of COLO 205 and WBCs. COLO205 are CK+, DAPI + and CD45+, while WBCs have different expressions CD-, DAPI+ and CD45+. PC3, SK-BR-3 and MCF-7 all exhibit similar fluorescent signals to COLO205.

$L$  in the tube. The growth of the diffusion layer is found to be slow enough to be neglected.

Some proteins in blood may cause RBCs stick to each other, forming clusters, and changing the sedimentation velocity. To avoid this bias, we replace the blood plasma with a buffer solution (*Dilution buffer, Veridex*). [119,120] The sedimentation samples are prepared in the following way: 2.5 mL of blood is drawn from a healthy subject, add 3.5 mL PBS, and centrifuge at a relative centrifugal force of 800G for 10 min. Supernatant containing white blood cells, platelets, blood plasma and buffer are removed. The buffer solution is then added to suspensions with RBCs volume rates  $\rho_{RBC} = 0.5, 0.25, 0.13, 0.06, 0.03, \text{ and } 0.01$ . The processed blood samples are mixed well and 2 mL of each sample is placed in a transparent tube and kept stable

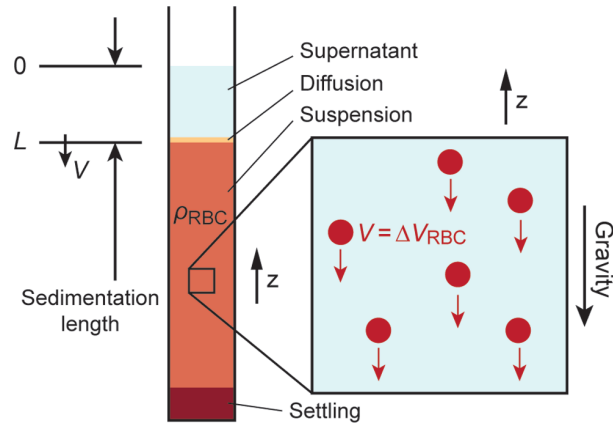


Figure 4.2: Red blood cell sedimentation rate measurement schematic. The sedimentation rate is defined as the growth rate of the sedimentation length  $L$  in the tube.

for hours.

Figure 4.3 shows the measured sedimentation for the six different volume RBC rates. The sedimentation velocity is estimated as the slope of the line fit for each sedimentation plot. Fit curve for  $y = a(1 - x)^n$  ( $n = 2, 3, 4, 5$ ) is used to model the relation between sedimentation velocity  $\Delta V_{RBC}$  as a function of  $\rho_{RBC}$  under the assumption that the sedimentation velocity should approach asymptotically to 0 as  $\rho_{RBC}$  gets closer to 1. Eventually, the relation can be expressed as:

$$\Delta v_{RBC} = 1.8 \times 10^{-6} \cdot (1 - \rho_{RBC})^4 \quad (4.1)$$

As we discuss previously, the total viscosity of blood suspension is the summation of the medium viscosity and the partial viscosity from RBCs as:

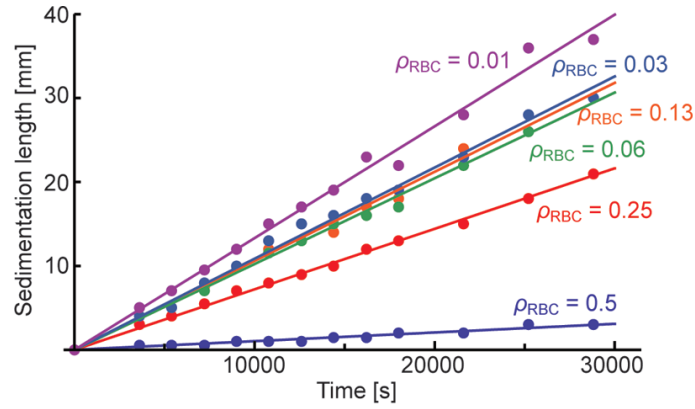


Figure 4.3: Measured RBC sedimentation length changes for different volume RBC rates ( $\rho_{RBC} = 0.5, 0.25, 0.13, 0.06, 0.03,$  and  $0.01$ ).

$$\eta_{RBC}(\rho_{RBC}) = \eta_{med} + \Delta\eta_{RBC}(\rho_{RBC}) \quad (4.2)$$

When  $\Delta V_{RBC} = 0$ , the RBC suspension can be treated as a continuous medium, and the viscosity is equate to the value of the medium:

$$\eta_{RBC}(0) = \eta_{med} \quad (4.3)$$

The relation between the volume RBC rate  $\rho_{RBC}$  and the blood viscosity  $\eta_{RBC}$  has been expressed in different formats, such as linear, [81] quadratic, [121] and exponential. [122] One of the easy way is the linear function by Einstein: [81]

$$\eta_{RBC} = \eta_{plasma}(1 + 2.5\rho_{RBC}) \quad (4.4)$$

We perform experiments to find out the relationship between the volume RBC rate ( $\rho_{RBC}$ ) and blood viscosity ( $\eta_{RBC}$ ) using a cone plate viscometer (*DV-I+*, *Brookefield, Middleboro, MA*) at the shear rates ranging from 2 to 750  $s^{-1}$ . Figure 4.4 shows the measured data. We use a simple linear fit, which is similar to Einsteins model, to estimate the function that gives the viscosity.

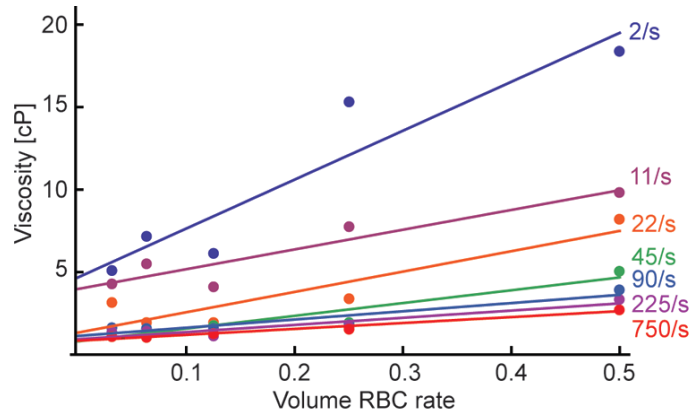


Figure 4.4: Measured blood viscosity as a function RBC volume rate  $\rho_{RBC}$  at different shear rates ranging from 2 to 750  $s^{-1}$ . Linear fit for each viscosity plot is also shown.

Assuming the shear rate of a moving rare cell to be on the order of  $\Delta V_{cell}/R_{cell}$ , with the cell radius  $R_{cell} = 7.5 \mu m$  and cell velocity  $\Delta V_{cell} \approx 10 \mu m/s$ , we decide to use the line fit at 2  $s^{-1}$  as the viscosity model used in the following calculations. Therefore, the relation between the volume RBC rate ( $\rho_{RBC}$ ) and blood viscosity ( $\eta_{RBC}$ ) can be expressed use:

$$\eta_{RBC} = 4.7 + 30 \cdot \rho_{RBC} \text{ [cP]} \quad (4.5)$$

Comparing Equation 4.5 with 4.4, we can define the related coeffi-

icients as:  $\eta_{med} = 4.7 [cP]$  and  $\Delta\eta_{RBC}(\rho_{RBC}) = 30 \cdot \rho_{RBC} [cP]$ .

## 4.2.2 RBC sedimentation modeling results

### Blood sedimentation in bent tubes

In order to verify the efficacy of our mathematical model, we first simulate RBC sedimentation in a simple bent tube with inner diameter of  $1.6 \text{ mm}$ , and bent curvature radius  $20 \text{ mm}$ . The tube can be considered as a simplified representation of the microchannel. The results are compared with experimental observations. A RBC suspension with a volume rate of  $\rho_{RBC} = 0.02$  starts flowing in a bent tube, which is initially filled with a medium  $\rho_{RBC} = 0$  at  $t = 0 \text{ s}$ . The tube space is divided into  $85 \times 85 \times 20$  three-dimensional cubic control volumes. Then, the distribution of volume RBC rates is calculated using *Matlab* program from 0 to 140 s, with a time step of 0.01 s. Photographs of the tube and simulation results are shown in Figure 4.5 for time points at  $t = 20, 80, \text{ and } 140 \text{ s}$ . The gray scale of the simulation result indicates the local RBC volume rate. Simulation results show good agreement with the measurements, especially when sedimentation is well grown in the tube at  $t = 140 \text{ s}$ .

### Blood sedimentation in microchannel

We then apply the sedimentation model to assess the immunomagnetic microchip. We build a 3D device model for finite element analysis. The model is show in Figure 4.6(a), with important dimensions included.

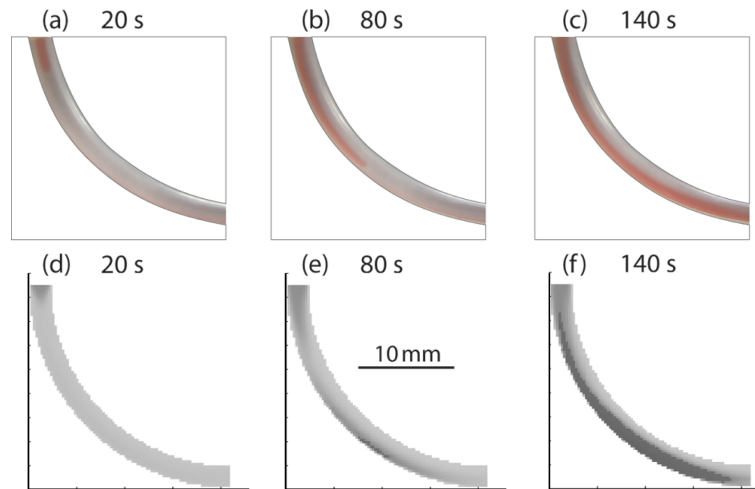


Figure 4.5: Comparative experiments of blood sedimentation in a bent tube. Photographs (preferred to be viewed in color) taken at (a) 20, (b) 80, and (c) 140 s. Simulation results at (d) 20, (e) 80, and (f) 140 s.

Figure 4.6(b) shows the flow velocity magnitude distribution calculated with a sample flow rate of  $Q = 10 \text{ mL/h}$ . The average flow velocity is given as  $v_{ave} = 0.33 \times 10^{-3} \text{ m/s}$ . This value falls into the typical range of microchip-based separators, where velocity in the order of  $10^{-6} \text{ m/s}$  [123] to  $10^{-3} \text{ m/s}$  [124] have been demonstrated. We used the three-parallel magnet array to provide the external magnetic attraction. The simulated magnetic field distribution can be seen in Figure 3.11(a).

Here, we are primarily interested in the orientations of the microchannel - upright and inverted. With different channel orientations, we can change the direction of gravity with regard to the magnetic force, and investigate the role of gravity in separating CTCs from blood. Please refer to Figure 3.9(c) for the illustration of the two orientations.

The three-dimensional model of the microchannel is divided into 20 (x axis)  $\times$  60 (y axis)  $\times$  20 (z axis) cubic control volumes. The channel is initially filled with medium without any RBCs  $\rho_{RBC} = 0$ . A RBC suspension with a volume rate of  $\rho_{RBC} = 0.5$  is flowed into the channel with flow rate of 10 mL/hr starting at the time point of  $t = 0$  s. The sedimentation patterns are shown in Figure 4.7(a) for the upright, and 4.7(b) for the inverted condition at the time points  $t = 20s, 40s, 80s$ . Three-dimensional illustration of the sedimentation can be seen in Figure 4.7(c) and (d) for upright and inverted channel at  $t = 270s$ . Through comparison between upright and inverted case, we find that RBC sedimentation gradually covers the bottom substrate “capture plane” in the upright condition. In contrast, there is a separation between the bottom substrate and the RBC stream in the inverted case. To facilitate cell capture, it is preferable that the capture plane is not covered with a viscos layer of RBC sedimentation. From this perspective, the inverted orientation is advantageous over the upright case.

### 4.2.3 Computational analysis of rare cell isolation

#### Cellular force analysis

Before we present the result of the cell tracking algorithm and discuss the efficacy of rare cell separation. We calculate the magnitude of several important forces in the system to clarify some assumptions of our calculations. The density of a cancer cell is assumed to be  $d_{cell} = 1.077 \times 10^3 \text{ kg/m}^3$ , [125] so the additional gravitational force acting on a cancer cell can be calculated

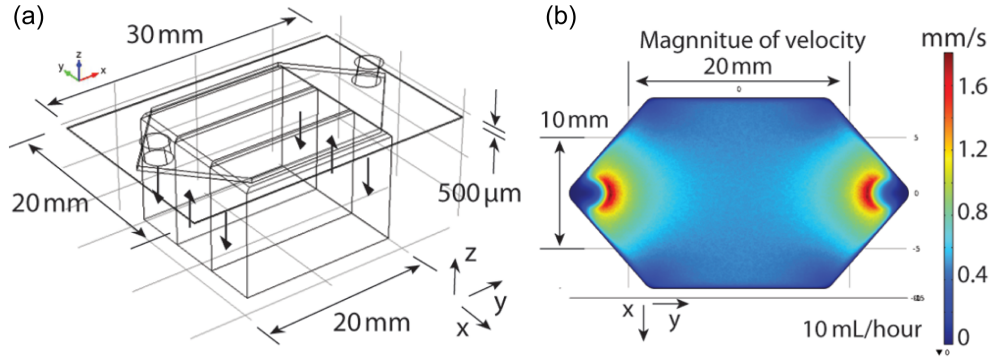


Figure 4.6: Configuration of the microfluidic immunomagnetic separation device. (a) Three-dimensional model created for a finite element analysis software *COMSOL*. (b) Flow velocity magnitude [mm/s] calculated with the sample flow rate of  $Q = 10$  mL/h.

by subtracting the buoyancy force as:

$$F_{g,cell} = \frac{4}{3}\pi R_{cell}^3 \cdot (d_{cell} - d_{water}) \cdot g = 1.3 \times 10^{-12} \text{ [N]} \quad (4.6)$$

Here  $R_{cell}$  is the radius of the cancer cell  $R_{cell} = 7.5 \mu m$ ,  $g$  is the acceleration of gravity  $g = 9.8 \text{ m/s}^2$ , and the medium density is  $d_{water} = 1 \times 10^3 \text{ kg/m}^3$ .

The magnitude of the magnetic force is dependent on the magnetic field gradient  $\nabla B^2$ , which is around  $\nabla B^2 = 10 \sim 70 \text{ T}^2/m$  at the bottom of the channel. [48] Therefore, the magnetic attractive force is estimated to be

$$F_{mag,cell} = \frac{V_{cell}\Delta\chi_{cell}}{2\mu_0}\nabla B^2 = 1.2 \times 10^{-10} \text{ [N]} \quad (4.7)$$

Here the effective relative magnetic susceptibility of the cell  $\Delta\chi_{cell}$  can be calculated using Equation 2.10, and is estimated to be  $\Delta\chi_{cell} = 0.0044 \text{ (SI)}$ .

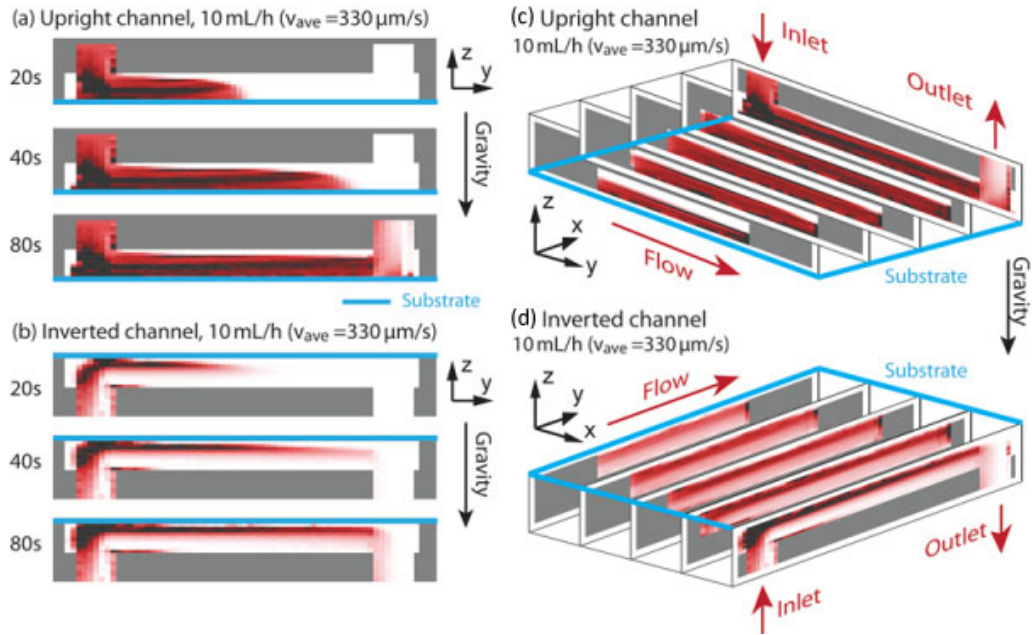


Figure 4.7: Simulated RBC sedimentation pattern inside the microchannel for (a) upright and (b) inverted orientations at the center y plane at the time of 20, 40 and 80 s. Three-dimensional illustration of the sedimentation patterns in (c) upright and (d) inverted at the times of 270 s. Upright channel makes a thicker sedimentation layer on the bottom substrate and the corner near the inlet.

The magnetic force is nearly two orders of magnitude larger than the gravitational force on the CTCs. It justifies our assumption that the magnetic force dominates the motion of the CTCs.

In addition, we investigate the effect of magnetic force on RBCs. The density of RBCs is found to be  $d_{RBC} = 1.10 [kg/m^3]$ , and the volumetric magnetic susceptibility is  $\Delta\chi_{RBC} = 6.5 \times 10^{-6} (SI)$ . [126] Therefore, the gravitational and magnetic forces on RBCs are calculated to be:

$$F_{g,RBC} = \frac{4}{3}\pi R_{RBC}^3 \cdot (d_{RBC} - d_{water}) \cdot g = 5.1 \times 10^{-13} [N] \quad (4.8)$$

$$F_{mag,RBC} = \frac{V_{RBC}\Delta\chi_{RBC}}{2\mu_0}\nabla B^2 = 5.1 \times 10^{-14} [N] \quad (4.9)$$

The gravitational force is about 10 times larger than the magnetic force. We can expect that RBC sedimentation could be affected at about 10% by the magnetic force. However, considering the variations found in the measured sedimentation velocity and the mathematical model we use here, an effect of 10% is still within the range of measurement errors and small enough to be neglected to simplify the calculation process. In the following simulation, we do not take the magnetic force on RBCs into account.

### **Rare cell separation analysis**

Now we discuss the result of the cell tracking algorithm. Cells are “virtually” released from the inlet of the microchannel. Figure 4.8(a) and (b) are examples of CTCs trajectories that are released at  $t = 270$  s (we assume the sedimentation profile becomes stable at this time point and beyond) in the upright and inverted channels, respectively. Three dimensional views of the cell trajectories are also shown for the upright and inverted channels. We can observe more cells being gradually pulled to the capture plane in the inverted orientation channel orientation.

In order to evaluate the significance of our analytical models, we

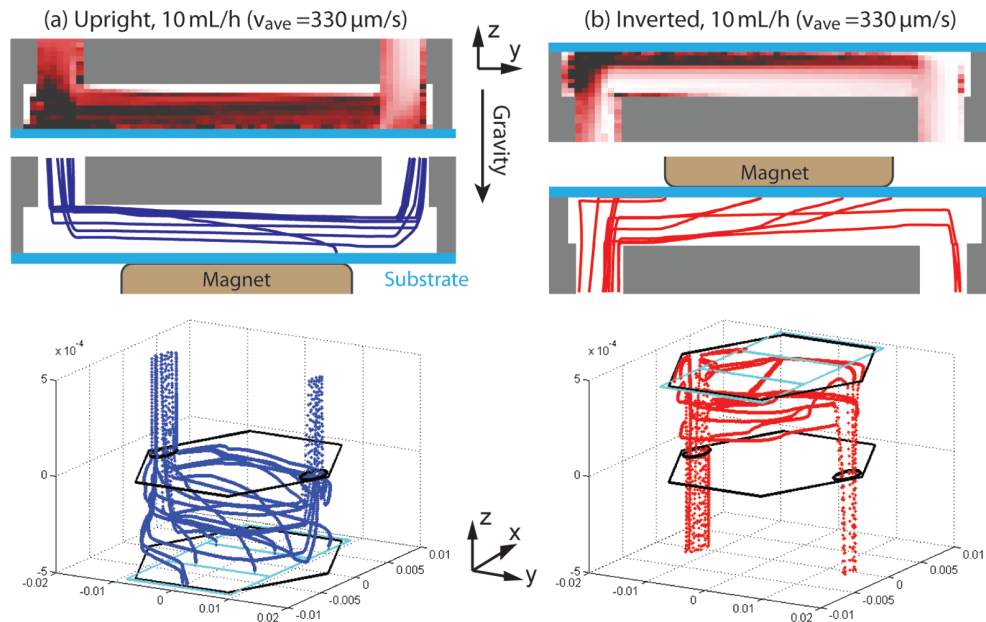


Figure 4.8: Side-view cell trajectories of the CTCs that are released at  $t = 270s$  for the (a) upright and (b) inverted channels respectively. 3D views of the trajectories are also shown for the upright and inverted channels. Position of the magnets (cyan line) and shape of the microchannel (black lines) are included in the figures.

perform comparative simulations under with different channel orientations, flow rates, and channel designs. The conditions used are as follows:

- (1) Upright,  $Q = 10 \text{ mL/h}$ , standard channel (channel width = 17 mm)
- (2) Inverted,  $Q = 10 \text{ mL/h}$ , standard channel
- (3) Inverted,  $Q = 5 \text{ mL/h}$ , standard channel
- (4) Inverted,  $Q = 5 \text{ mL/h}$ , half-width channel (channel width = 8.5 mm)

The sedimentation patterns calculated for conditions (1) - (4) are

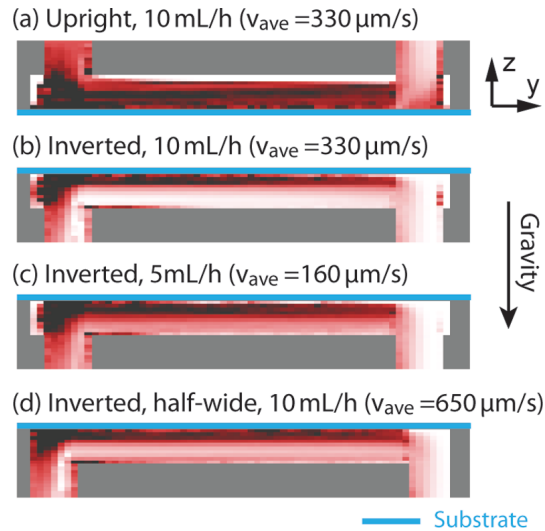


Figure 4.9: (a)-(d) RBCs sedimentation pattern calculated for the four control conditions (1-4) with different channel orientations, flow rates and channel designs at the time of  $t = 270\text{s}$ .

shown in Figure 4.9(a) - (d), and Figure 4.10(a) - (d) show the simulated capture counts and final positions of the captured cells on the substrate under the four conditions. Comparison between Figure 4.10(a) and (b) shows that the capture efficiency of the upright channel is significantly lower than the inverted channel, which can be attributed to the high viscosity of the dense RBC layer that covers the capture plane. The effect of the flow rates can be found in comparison between Figure 4.10(a) and (c). Even though cells stay inside the channel for longer time with slow flow rate, the thicker RBC sedimentation layer counter-balances the effect of the flow rate and results in a similar capture rate. Same principle can be used to explain the results of the half-width channel in Figure 4.10(d), since the half-width channel essentially makes the flow rate two times faster. The results suggest that

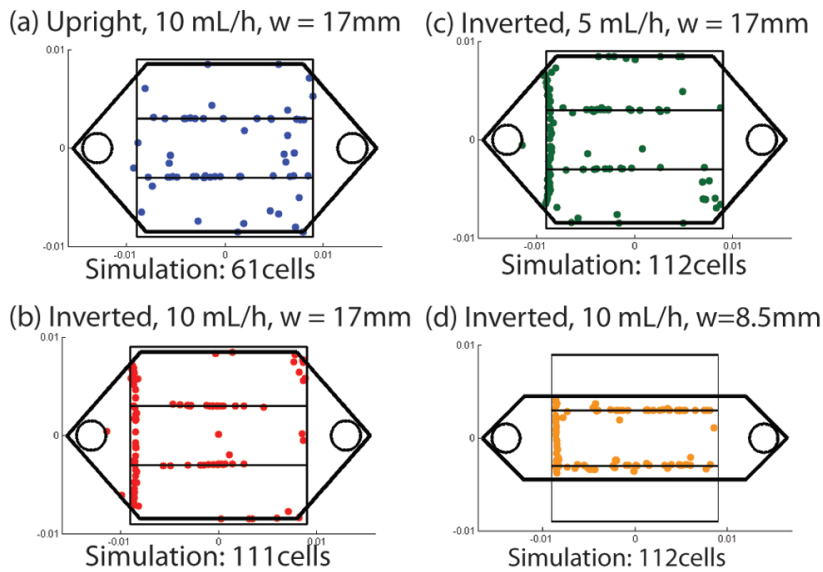


Figure 4.10: (a)-(d) Simulated maps of the captured CTCs compared for the four conditions (1-4). In the simulation, 150 cells are released randomly from the inlet of the microchannel.

the orientations of the channels, and the corresponding viscosity changes of the local microenvironment have a large effect on the capture rates of the immunomagnetic assay.

#### 4.2.4 Experimental verifications

We conduct experiments with plain glass slides corresponding to the conditions (1) - (4) to verify our theoretical models. We use the rotational holder (as shown in Figure 3.9(c)) to place microchannels in inverted and upright orientations. A 100  $\mu\text{L}$  aliquot of cancer cell suspension that contains an average of  $\sim 150$  COLO205 cells is spiked into 2.5 mL of healthy blood sample. The cell count is chosen to match the value used in the simulation.

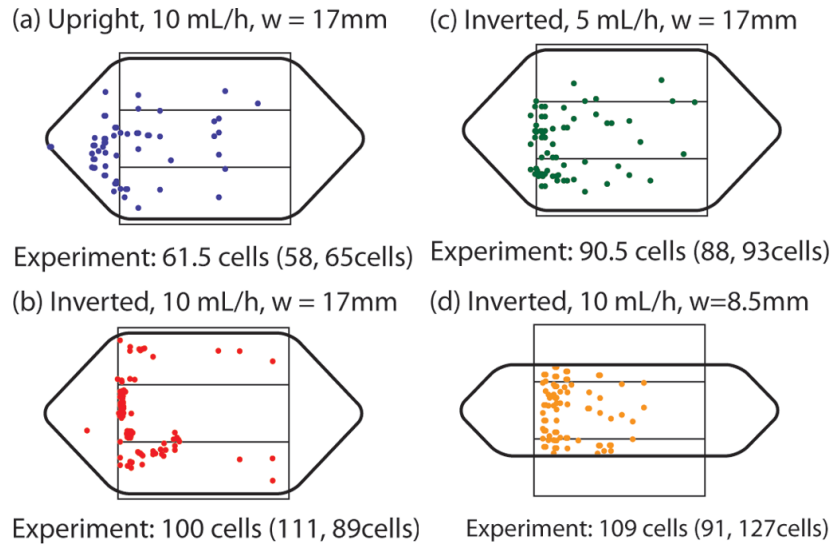


Figure 4.11: (a)-(d) Experimental maps of the captured CTCs compared for the four conditions (1-4). In the experiment, an average of 150 cells are spiked into blood.

The blood plasma is replaced with buffer solution. The experimental results of the capture rate and cell maps are shown in Figure 4.11. Compared with the simulation results in Figure 4.10, experimental results show excellent agreement, indicating the efficacy of our computational model. Additionally, it confirms that the inverted orientation can significantly increase the CTC capture rate for 30%. The number of magnetic particles  $N$  attached to a rare cell is determined based on several experimental conditions such as the type of the rare cell, amount of antigen expression on the cell surface, and concentration of introduced magnetic nanoparticles. We first try  $N = 20000$  to match the simulation and experimental rare cell capture rates for condition (1), then the same  $N$  value is used for the other conditions.

### 4.3 Micromagnet characterization

#### 4.3.1 Micromagnetic field generation

We first calculate the magnetic field generated by a single micromagnet element. In our system, the micromagnets are fabricated using nickel (Ni). The dimension of each micromagnet is  $20 \mu m$ (width)  $\times$   $200 \text{ nm}$  (thickness). The saturation magnetization of Nickel is found to be  $55.1 \text{ emu/g}$  [127] (can be converted to volume magnetization of  $M_{es} = 4.9 \times 10^5 \text{ A} \cdot \text{m}^{-1}$ ). We plot the distribution of both X and Y components of the magnetic field along horizontal lines ( $-40 \mu m < x < 40 \mu m$ ), at three different heights ( $h = 5 \mu m, 10 \mu m$  and  $15 \mu m$ ) on top of the micromagnet.

The results can be seen in Figure 4.12 ((a) $B_x$  and (b) $B_y$ ), where the micromagnet is shown as a gray box (size not to scale) to indicate the position. The magnetic field curves are shape coded according to the heights of the plotting. The field generated by the micromagnet decays fast in both vertical and horizontal directions. Since the value of magnetic force is largely dependent on the properties of the targets, we plot the gradient  $\nabla B^2$  as an indirect but objective measurement of the magnetic force. The results are presented in Figure 4.12(c) ( $\nabla B_x^2$ ) and Figure 4.12(d) ( $\nabla B_y^2$ ). The negative values of the gradient in Y direction indicate that the micromagnet generates attractive force towards the surface that promotes the separation and helps retaining the cells.

We define the effective range of a micromagnet element to be the distance where the magnetic force ( $F_{mag}$ ) acting on the cells is equal to the

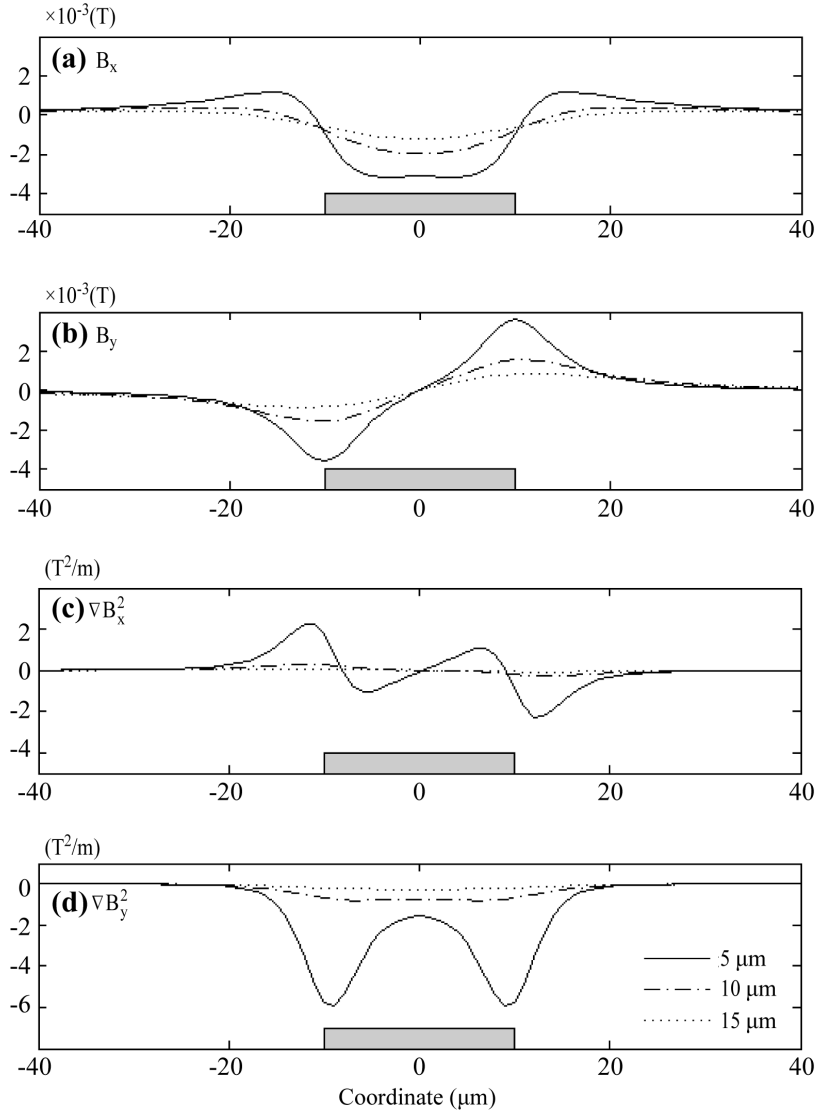


Figure 4.12: Magnetic field and gradient calculated for a single micromagnet element (a)  $B_x$ , (b)  $B_y$ , and the magnetic field gradient (c)  $\nabla B_x^2$  and (d)  $\nabla B_y^2$ . The gray box indicates the lateral position of the micromagnet. The curves are plotted along horizontal lines ( $-40\mu\text{m} < x < 40\mu\text{m}$ ) with different heights ( $h = 5 \mu\text{m}, 10 \mu\text{m}$  and  $15 \mu\text{m}$ ) on top of the micromagnet.

gravitational force ( $F_g$ ). Beyond this range, micromagnets cannot generate sufficient magnetic force to dominate the movement of the cells. According to our previous calculations (Equation 4.6), the gravitational force on a single cancer cell is  $F_g = 1.3 \times 10^{-12}$  [N], which gives an equivalent threshold magnetic gradient to be  $\nabla B^2 \approx 0.3 T^2/m$ . Therefore, the vertical effective range is  $15 \mu m$ . As for the lateral range, we make the decision by examining the gradient at  $10 \mu m$  on top of the micromagnets, which is the center of the CTCs when they are on the surface (typical diameter of CTCs is  $\sim 20 \mu m$ ). [10] The lateral range is found to be  $\pm 15 \mu m$ . The fact that the effective capture range of the micromagnet is comparable to the size of a single cancer cell indicates that only a few cells can interact fully with each micromagnet through its magnetic field. It helps distribute cell populations across the substrate covered by the network of micromagnet elements.

In addition, we also perform calculations for micromagnet array (an array of 3 elements linearly aligned is used as an example), magnetized in the horizontal direction. The dimensions of each micromagnet are consistent with the single element study ( $20 \mu m \times 200 nm$ ), and the edge-to-edge distance between adjacent micromagnets is  $100 \mu m$ . The magnetic field along a horizontal line  $10 \mu m$  on top of the micromagnet array is shown in Figure 4.13(a). The magnetic field gradients are shown in Figure 4.13(b). The magnetic field generated by micromagnet array exhibits the same characteristics as single element, with the profiles being spatial repetition of a single micromagnet.

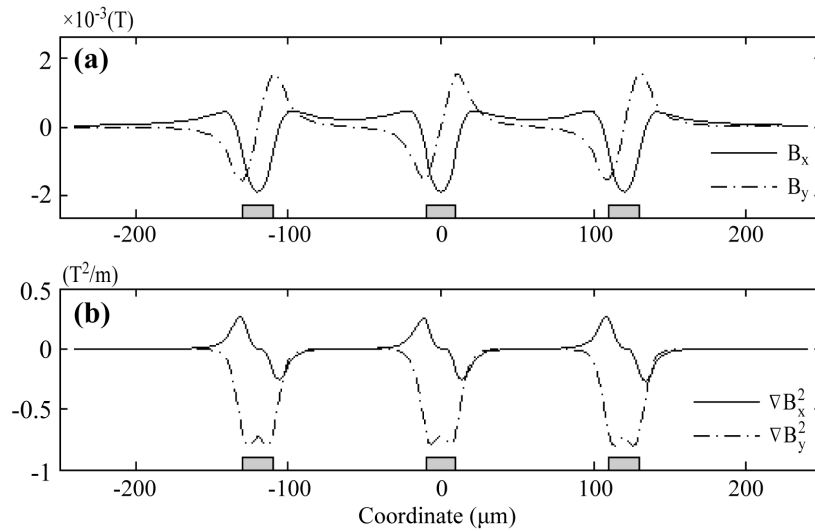


Figure 4.13: Magnetic field (a) and magnetic field gradient (b) of an linear array of three micromagnets. The data are plotted  $10\mu\text{m}$  on top of the micromagnet array.

### 4.3.2 Impact of micromagnets on CTCs detection

We incorporate the micromagnets into the 2D immunomagnetic microchip model to investigate the impact of the micromagnets on cell separation. Key design parameters of the microchip and detailed introduction of the model can be found in Figure 2.7 and the related descriptions. We divide the motion of the target cells into two stages - (i) in free space and (ii) on solid surface after hitting the channel substrate to obtain the final locations of the captured cells. Figure 4.14(a) shows the calculated trajectories of the target cells inside the microchannel at a flow rate of 2.5 ml/hr. In the first stage, the cells are attracted by the permanent magnets and gradually move towards

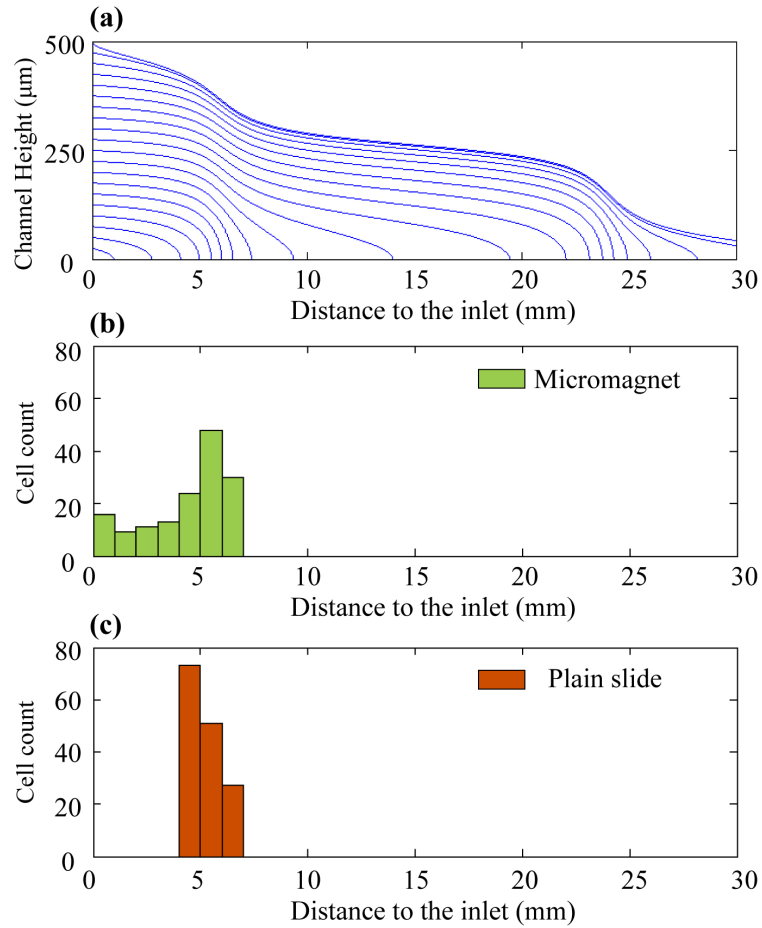


Figure 4.14: Simulation results of the impacts of micromagnets on rare cell detection. (a) Sample cell trajectories in the microfluidic channel. (b) distribution histogram of the captured CTCs of micromagnet slide and (c) plain slide.

the substrate as they flow through the channel. In the second stage, cells continue moving under the combined influence of the permanent magnets and micromagnets. The calculated histograms of the final positions of the captured cells are shown in Figure 4.14(b) and (c) for micromagnet slide and plain slide separately. On plain slide, most of the cells are captured and aggregated in a confined area, where the front edge of the permanent magnet lies (refer to Figure 2.7 for the position of the permanent magnet). In contrast, micromagnet slide exhibits a broader cell distribution spectrum from the inlet to the front edge of the magnets as expected. This result indicates that the micromagnet array re-arranges the magnetic field inside the microchannel and improves the distribution patterns of the captured CTCs. The stopping factor is estimated to be  $\lambda = 1.2$ .

#### **4.4 Screening results - Ni micromagnet**

Now we discuss the experimental results of using the Ni micromagnet integrated system to separate rare CTCs. As we mentioned before, four different human cancer cell lines, including COLO205 (colorectal cancer cell), SK-BR-3 and MCF-7 (breast cancer cell), and PC3 (prostate cancer cell), are used as the model cells. The CTCs are identified based on fluorescent signals from CK, CD45, and DAPI, as illustrated in the fluorescent panel in Figure 4.1. Please note that in the experiments with the Ni micromagnets, we use the three-parallel permanent magnet configuration as the external magnetic flux source. Since the micromagnets increase the surface retention

force at short range, we can directly observe the cancer cells' being captured by a micromagnet with a strong fluorescent signal and intact shape, as shown in Figure 4.15(a). SEM images of cancer cells being captured by micromagnets are shown in Figure 4.15(b), which confirm the interactions between the target cells and the micromagnets.

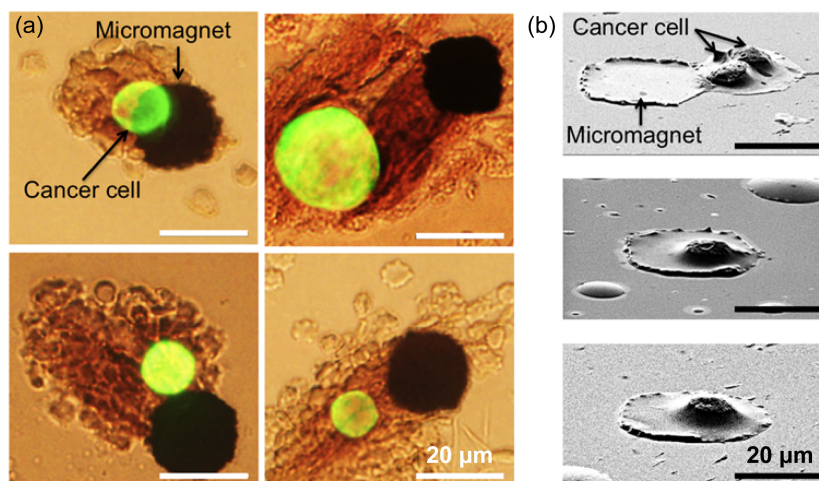


Figure 4.15: Ni micromagnet screening experimental results with COLO205 cells. (a) Overlay of fluorescence images and bright field images of CK-stained COLO205 cells (green) captured by Ni micromagnets. (b) SEM images of of COLO205 cells captured next to or on top of the Ni micromagnet.

Figure 4.16(a) summarizes the capture rates of the four spiked cell lines with the Ni-micromagnet integrated immunomagnetic system (COLO205:  $98\pm 7\%$ , PC3:  $99\pm 5\%$ , SK-BR-3:  $90\pm 3\%$ , and MCF-7:  $100\pm 9\%$ ). On average, the Ni micromagnet integrated system yields  $>97\%$  capture rates. Meanwhile, we run experiments with plain slides (without any surface patterns) in parallel for comparison. We choose COLO205 and PC3 as the model cells. On plain slides, the capture rates are  $84\pm 19\%$  for COLO205

and  $86 \pm 11\%$  for PC3, as shown in Figure 4.16(b). To briefly sum up, the implementation of the thin-film Ni micromagnets optimizes the immunomagnetic assay in the following aspects: first, an average 14% increase in capture rate is achieved. Second, the micromagnets reduce the variations of the capture rates by 10%, indicating an improved working stability. In addition, the integrated micromagnets improve the working versatility of the immunomagnetic assay by increasing the number of types of cancer cell lines that are applicable to this system.

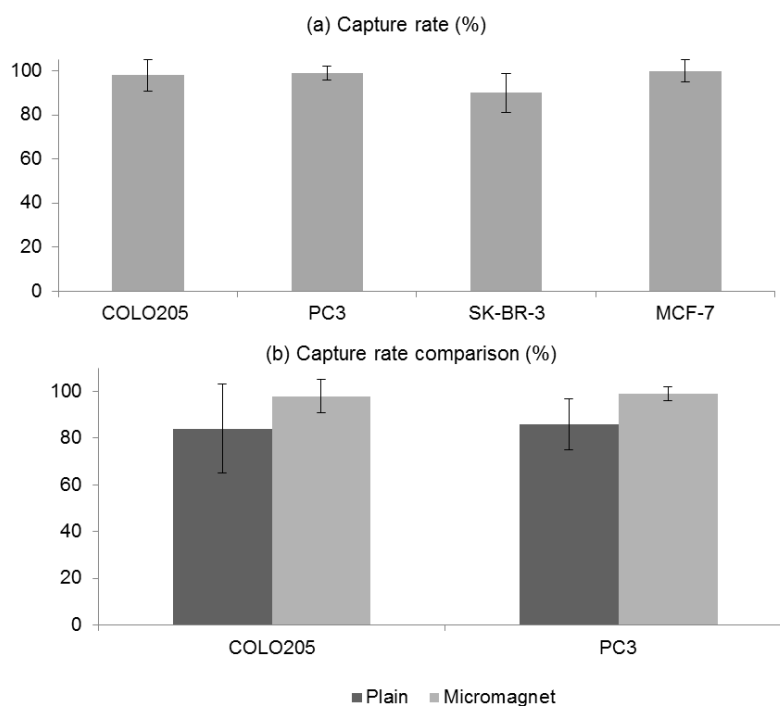


Figure 4.16: Ni micromagnet cell screening results. (a) Capture rates for the four cell lines: COLO205, PC3, SK-BR-3 and MCF-7. (b) Capture rate comparison between micromagnet slides and plain slides using COLO205 and PC3 cells as the screening targets.

To further investigate the impacts of the micromagnets, we categorize the captured CTCs into three groups based on how they are captured: 1) directly by micromagnets, also including the cells that are captured by the nanoparticle aggregating around the micromagnet element; 2) by permanent magnets, including the CTCs that are found near the front edge of the permanent magnets, but are not attached to any micromagnets; and 3) in others areas - these cells are also captured due to magnetic attraction. Figure 4.17 shows the percentage of CTCs in each category for plain slides and micromagnet slides respectively, using COLO205 and PC3 as the target cells. According to Figure 4.17(a), in the experiments with COLO205,  $90\pm 7\%$  of the spiked cells are captured by permanent magnets, while  $10\pm 8\%$  are captured in other ways on plain slides. On micromagnet slides, micromagnets attract  $59\pm 6\%$  of the captured cells, while  $35\pm 6\%$  cells are still captured by the permanent magnets, and only  $6\pm 1\%$  of spiked cells are captured elsewhere. In the spiked experiment with PC3 cells, about  $39\pm 6\%$  of the target cells are attracted by the micromagnets. The numbers of PC3 cells captured by permanent magnets drops from  $72\pm 12\%$  to  $49\pm 6\%$  after the implementation of the micromagnets. We observe a similar phenomenon in the spiked experiments with MCF-7 and SK-BR-3 cells - 23% and 40% of the spiked cells are captured by the micromagnets. The increased ratio of cells captured by the micromagnets demonstrates the interactions between micromagnets and the target cells. We can conclude that the increase in the capture rates is largely attributed to the implementation of the micromagnets.

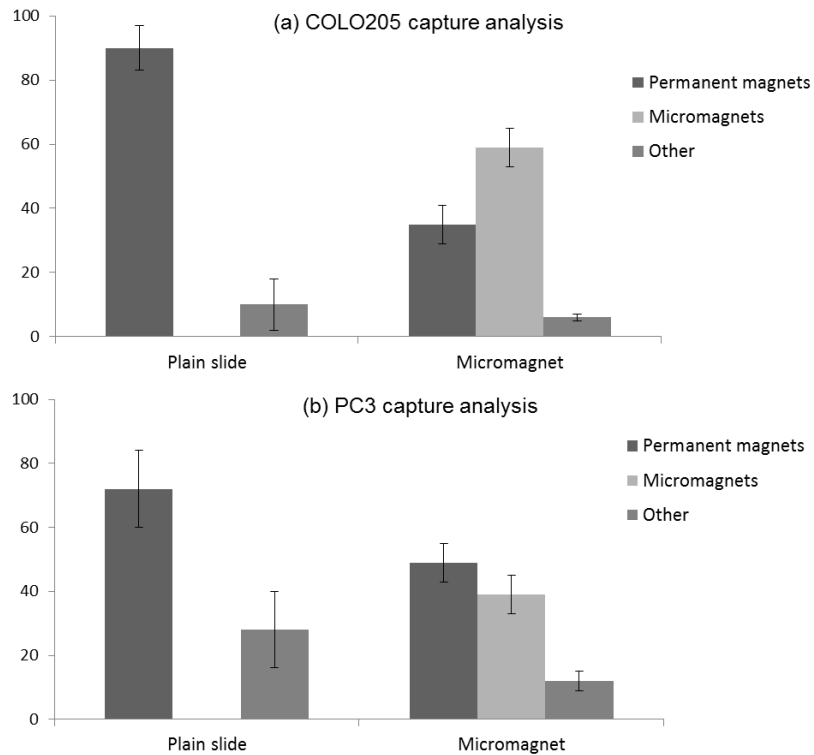


Figure 4.17: Breakdown analysis of the spiked COLO 205 and PC3 cells based on how they are captured on plain and micromagnet slides respectively.

In addition, we study the effect of the micromagnet in changing the distribution of the CTCs after capture. Here, we use COLO205 as the model cell line. We run experiments using micromagnet slides and plain slides in parallel for comparison. Figure 4.18(a) shows example location maps of the captured CTCs on the micromagnet and plain slide, respectively. We summarize the positions of the cells based on the distance to the channel inlet and generate the distribution histogram in Figure 4.18(b). The experimental results of the distribution histogram match the simulation results (presented

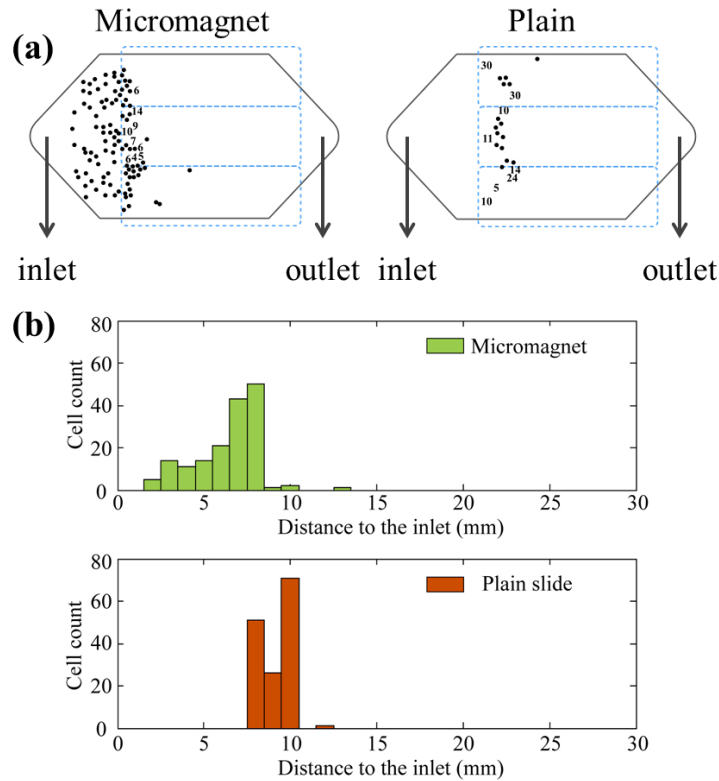


Figure 4.18: Micromagnet distribution analysis of the spiked experiments using COLO205. (a) Locations of the captured COLO205 cells on plain slide and micromagnet slide. (b) Distribution histogram of the captured CTCs from micromagnet slide and plain slide respectively.

in Figure 4.14(b) and (c)) very well, both showing that cells captured on the micromagnet slides are more evenly distributed than those on plain glass slides. To quantify the comparison of the distribution uniformity, we define a parameter “distribution uniformity” by calculating the unit area ( $1 \text{ mm} \times 1 \text{ mm}$ ) within the microchannel that has at least one captured cell. This term can be used to reflect the channel space occupancy. On plain slides, the uniformity is found to be  $9 \pm 4\%$ . After the implementation, the micro-

magnets change this value to  $23\pm 4\%$ , an increase of  $14\pm 8\%$ . These results further demonstrate the value of micromagnets - not only in increasing the capture rate but also in optimizing the distribution of the captured cells on the substrate.

We also use the Ni micromagnet integrated system to study blood samples from cancer patients and successfully discover CTCs with four different types of metastasis cancers - colorectal, lung, prostate, and breast cancers. The CTCs are identified based on the same immuno-staining methodology. Similar to the spiked experiments, 54% of the CTCs are captured by micromagnets, and we observe cancer cells being captured directly by the micromagnets, as shown in Figure 4.19. Table 4.1 summarizes the pathology information and CTC screening experimental results of the patient samples.

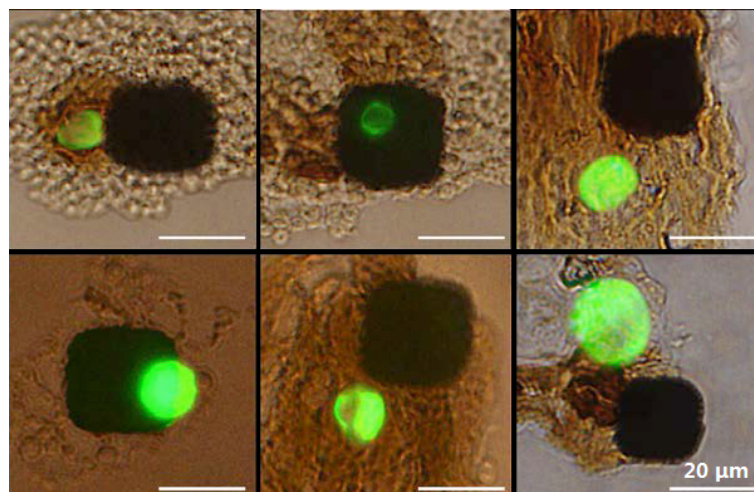


Figure 4.19: Overlay of fluorescence image and bright field image of CTCs from patient blood samples captured by micromagnets.

Table 4.1: Pathology information and screening results using the Ni micromagnet-integrated immunomagnetic assay for patient studies.

Sample	Ferrofluid/ Blood ( $\mu\text{l/ml}$ )	Flow rate (ml/hr)	Screening volume (ml)	CTC counts	Cancer type
1	7.5	2.5	7.5	2	Breast
2	7.5	2.5	7.5	1	Breast
3	7.5	2.5	10	22	Breast
4	7.5	2.5	5	215	Breast
5	7.5	2.5	7.5	2	Breast
6	7.5	2.5	7.5	6	Breast
7	7.5	2.5	5	10	Breast
8	7.5	2.5	7.5	13	Prostate
9	7.5	2.5	7.5	7	Prostate
10	7.5	2.5	12.5	7	Prostate
11	7.5	2.5	7.5	3	Breast
12	7.5	2.5	7.5	6	Breast
13	7.5	2.5	10	1	Lung
14	7.5	2.5	5	7	Breast
15	7.5	2.5	5	1	Colon

## 4.5 Screening results - Inkjet micromagnets

To test the strength of the inkjet-printed patterns, we first run separation experiments using fluorescent magnetic microbeads as the targets. The fluorescent magnetic microbeads (*FCM-2052-2, Spherotech, IL*) are made with ferromagnetic material, with diameters of  $2\ \mu\text{m}$ , and are pre-conjugated with green fluorescent dyes (470 nm/ 490 nm). An amount of  $3\ \mu\text{L}$  microbeads suspension is added to 1 mL PBS and flowed through the printed-patterned integrated microchannel at the rate of 5 mL/hr. Figure 4.20(a) shows the fluorescent image of the slide after the screening experiments. The printed patterns work as microscale magnetic flux sources and attract the magnetic beads. We plot the relative fluorescent intensity of the image as shown in Figure 4.20(b). It exhibits regular repetition, and the distance between two adjacent fluorescent peaks is about  $75\ \mu\text{m}$ , which is the value we use for the fabrication. It validates the idea that the surface pattern is generated due to the printed micromagnet patterns. Furthermore, we examine the fluorescent signal intensity of the beads suspension before and after the screening with a spectrofluorometer, and the depletion rate is 100%.

Moreover, we perform cell screening experiments with COLO205 cells as the separation targets using the immunomagnetic assay integrated with the inkjet-printed patterns. Other experimental conditions are identical to the standard protocol. Blood samples are acquired from healthy donors. Then, blood plasma is replaced using a dilution buffer to keep the physiological properties of the screening samples consistent. *Ferrofluid* nanoparticles

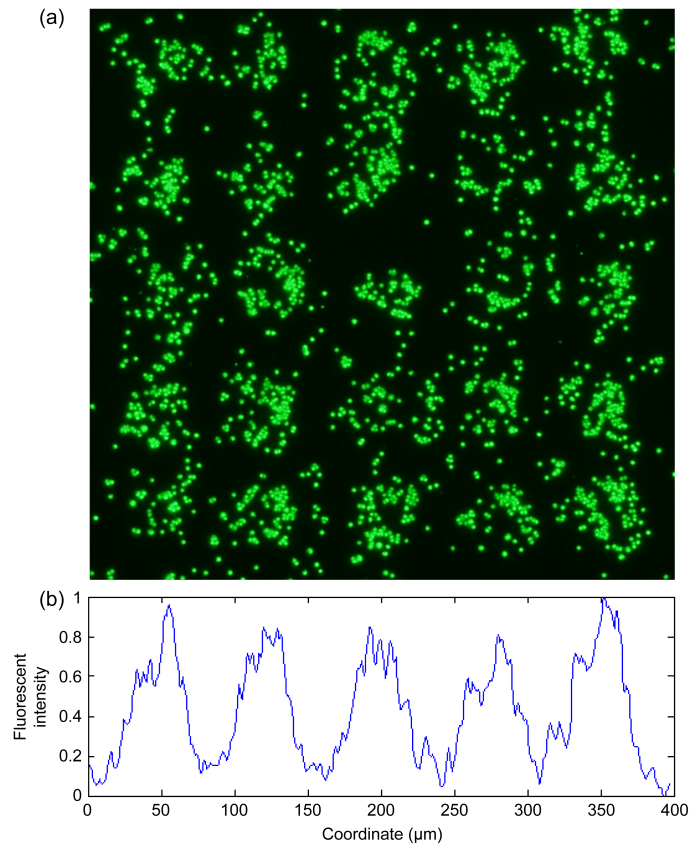


Figure 4.20: (a) Magnetic fluorescent beads screening results with the inkjet printed patterns. (b) Relative fluorescent intensity profile exhibits regular repetition, with periodicity equal to the value of the printed patterns.

are used to label the cells and provide the magnet momentum. During the screening experiment, flow rate is 2.5 mL/hr. After the screening, we stain the slides with CK/DAPI/CD45 for cell identification, counting and locating. We then observe the slides using a brightfield and a fluorescent microscope, respectively. The brightfield images and fluorescent signals from three dyes are shown in Figure 4.21. We can observe COLO205 cells being directly captured onto the printed patterns. There are also cells being trapped by the

ferrofluid nanoparticles aggregated around the printed patterns, as shown in the overlay images in Figure 4.21. These observations are similar to what we find with the Ni micromagnets.

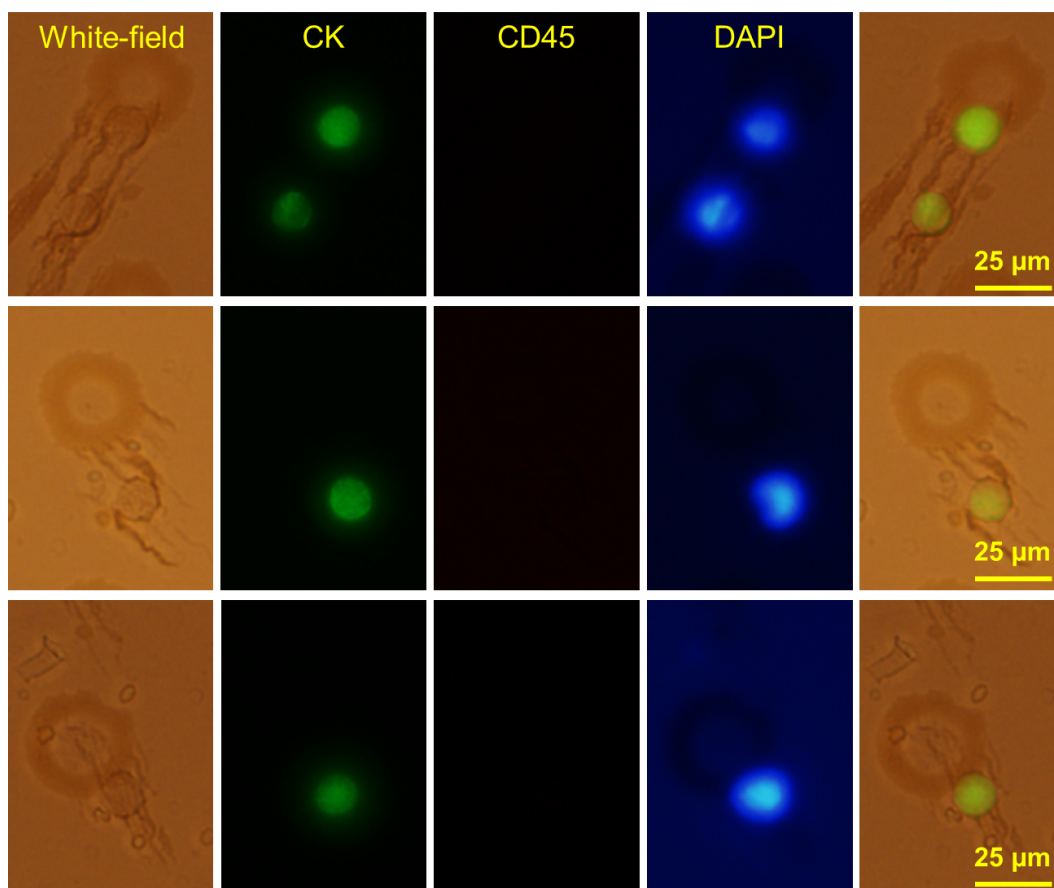


Figure 4.21: Brightfield and fluorescent images of the COLO205 cells found on the inkjet printed slides. Cells are either directly captured by the printed patterns or indirectly trapped by the magnetic nanoparticle aggregation around the printed patterns.

Now we discuss the capture efficiency of the inkjet-printed slides. Noteworthy is that we use the 6×6 pixel permanent magnet array (as il-

illustrated in Figure 3.10) with spacer insertion as the external magnetic flux source in this section with the inkjet patterns. Since the permanent magnet configuration design has changed compared with the Ni micromagnet, here we are comparing the inkjet printed slide and the plain slide. On plain slides, the average capture rate is  $67.5 \pm 15.5\%$ , while on inkjet printed slides, the average capture rate is  $103 \pm 1\%$ . The printed pattern increases the capture rate by  $35.5 \pm 16.5\%$  compared with plain slides. To study the effect of the patterns, we divide the captured cells into two groups based on whether they are captured by the printed patterns. The results are shown in Figure 4.22 (blue dots: captured by micromagnets, orange dots: captured by permanent magnets). 78.5% of the captured cells are found to be captured by the printed patterns, and 21.5% of the cells are captured by permanent magnets.

Eventually, we study the distribution of the captured cells. One sample patterned slide and one plain slide are shown in Figure 4.22(a) and (b), respectively. The position of the permanent magnet array is also shown in Figure 4.22. Compared with the cell maps and histograms using the three-parallel permanent magnet array (Figure 4.18(a) and (b)), the combination of pixel permanent magnet and inkjet printed pattern create even better distribution. The insertion of the spacers reduces the magnetic field at the front of the channel, allowing more cells to migrate beyond the front edge of the permanent magnet array. A significant number of the cells are captured at the center and end part of the channel. The distribution

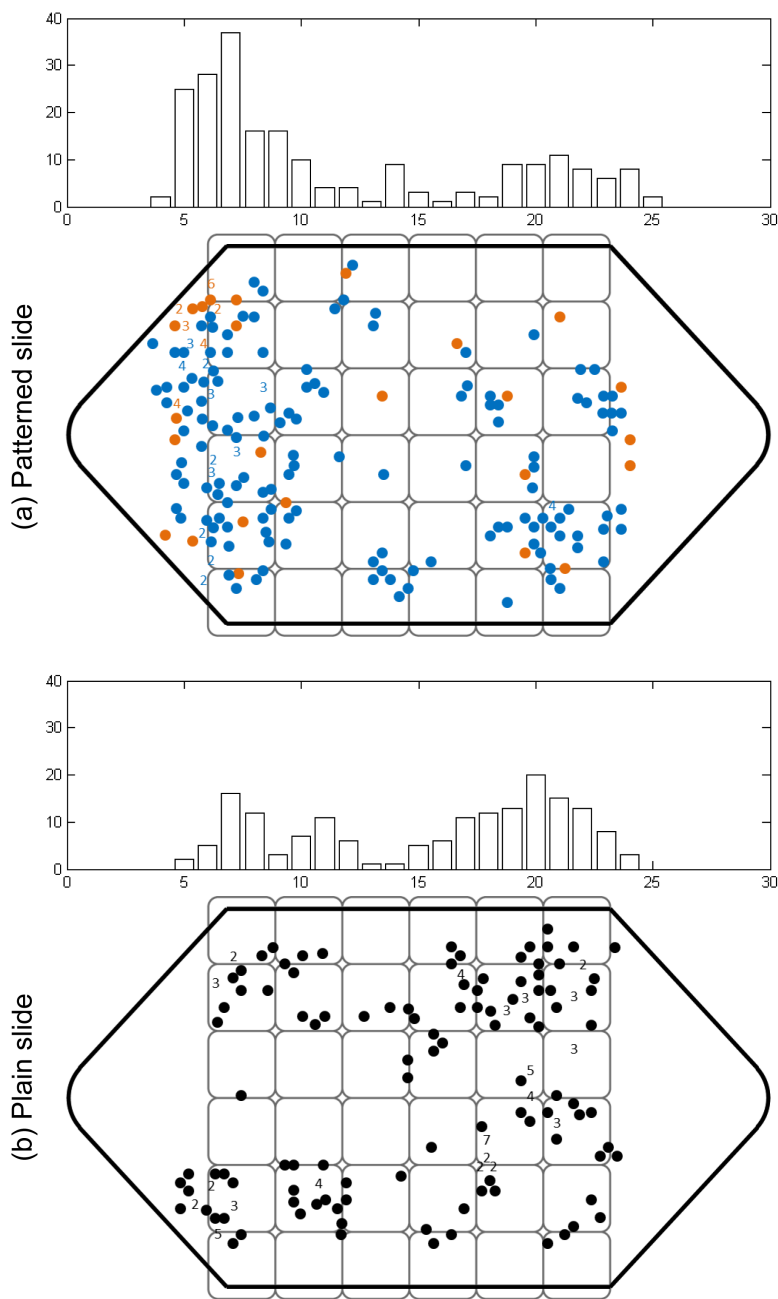


Figure 4.22: Cell screening results with COLO205 on patterned and plain slides. (a) Map and histogram on the printed slide. Blue cells are captured by the printed patterns, while orange cells are captured by the permanent magnets. (b) Map and histogram on plain slide.

uniformity is further increased by 20%. In addition, through comparison between Figure 4.22(a) and (b), we find that the cells start to be captured before the permanent magnet array on the patterned slides, whereas on plain slides, all the cells are captured on top of the permanent magnet array. It can be attributed to the patterns before the permanent magnet array being magnetized and generating an attractive force to retain the cells. Overall, the printed pattern combined with the pixel permanent magnet array yields high capture rates but with even better distribution. It can potentially work as a flexible substitute for the deposited Ni micromagnets.

## 4.6 Summary

In this chapter, we first presented the results of the blood sedimentation model and the cell tracking model, based on a set of measurements of blood characteristics. It reveals that keeping the microchannel in the inverted orientation can significantly increase the capture rate of the immunomagnetic assay by 30%.

Then we introduced the modeling results of the thin-film micromagnet implementation. We calculated the magnetic field generated by the thin-film micromagnets, and determined the vertical effective range to be  $15 \mu m$ , and the lateral range to be  $\pm 15 \mu m$ . We incorporated the micromagnets into a 2-D model simulating the immunomagnetic assay and observed an extended distribution spectrum, indicating that micromagnets help improve the distribution of the captured cells.

In the last section, we presented the experimental results using the Ni micromagnet and the inkjet printed micromagnet separately. Ni micromagnets achieve over 97% capture rates in spiked experiments with COLO205, SK-BR-3, PC3, and MCF7. Compared with the plain slide, the Ni micromagnet increases the capture rate by 14% on average. It also improves the distribution uniformity by  $14\pm 8\%$ . On the other hand, the inkjet printed patterns achieve a similarly high capture rate of  $103\pm 1\%$ , with a  $35.5\pm 16.5\%$  increase compared with plain slides. Using the pixel permanent magnet array, the inkjet pattern further optimizes the cell distribution after capture, increasing the distribution uniformity by 20%.

## Chapter 5

### Conclusion and Future Work

#### 5.1 Conclusion

Rare cell separation has been an important emerging process toward the early diagnosis of diseases such as cancer. In particular, circulating tumor cells (CTCs) have been extensively studied due to their clinical significance in cancer diagnosis, prognosis, and treatment monitoring. Immunomagnetic assay combines the strength of magnetic separation and biomarker recognition and has been a promising tool to perform CTC detection. In this dissertation, we present the theoretical frameworks and technical approaches to develop an immunomagnetic CTC detection platform with high sensitivity, stability, and versatility.

The major contributions of the dissertation includes:

First, we investigate the principles of magnetic separation, and the related biophysical phenomenon on micro-scale. We address the impacts of the system parameters on the detection efficiency of the immunomagnetic assay, and discover two important parameters - the viscosity of the micro-environment ( $\eta$ ) and the magnetic field ( $B$ ) - that are worthy of more in-depth studies.

We develop a set of theoretical models to describe the relationship between the micro-environment viscosity and rare cell detection. The red blood cell (RBC) sedimentation model, in which the local RBC volume rate can be instantly calculated based on the medium flow field and the RBC sedimentation rate. The partial viscous model, which connects the RBC sedimentation with rare CTC detection. The cell tracking algorithm, which allows us to trace the movement of the target cells, to record the positions where they are captured, and to evaluate the detection system.

To improve both the capture efficiency and cell distribution after capture of the immunomagnetic assay, we propose a micromagnet approach to modulate the in-channel magnetic field ( $B$ ). We discuss the micromagnet magnetization process and principle of the micromagnet integration. Based on a 2-D model simulating the thin-film micromagnets, we calculate the magnetic field generated by the thin-film micromagnets and determine the vertical effective range to be  $15 \mu m$  and lateral range to be  $\pm 15 \mu m$ . In addition, we theoretically demonstrate the contribution of the micromagnet in optimizing the cell distribution after capture.

Second, we develop two technical approaches to fabricate the thin-film micromagnets based on e-beam deposition and inkjet printing technology. The fabrication principles, processes and results are presented and analyzed detailedly. We build a screening system, which incorporates a rotational stage to control the channel orientation based on the specific requirements at different experimental steps.

Third, we present the experimental results in using the proposed system to do CTC screening. We perform comparative studies of cell separation with different channel orientations (upright and inverted), flow rates, and channel widths. Experimental and simulation results match well, both indicating that keeping the microchannel in the inverted orientation can significantly increase the capture rate of the immunomagnetic assay for 30%, while the flow rates and channel widths do not affect the capture rate much.

In the experiments with the micromagnets, the Ni micromagnets achieve over 97% capture rates in spiked experiments with COLO205, SK-BR-3, PC3 and MCF7. Compared with plain slides, the Ni micromagnet increases the capture rate by 14% on average. It also improves the distribution uniformity by  $14\pm 8\%$ . The Ni micromagnet integrated system has also been used to study clinical samples, and successfully isolate CTCs from four types of metastatic cancer patients. The inkjet printed patterns achieve a similarly high capture rate of  $103\pm 1\%$ , with a  $35.5\pm 16.5\%$  increase compared with plain slides. Using the pixel permanent magnet array, the inkjet pattern further optimizes the cell distribution after capture, increasing the distribution uniformity by 20%.

To sum up the dissertation, as is shown in Figure 5.1, we derive theoretical models that successfully address the fundamental relations between force, flow, and field at the interface of engineering and biomedicine. We successfully build an immunomagnetic assay for rare CTC detection with enhanced sensitivity, stability, versatility, and yields better cell distribution

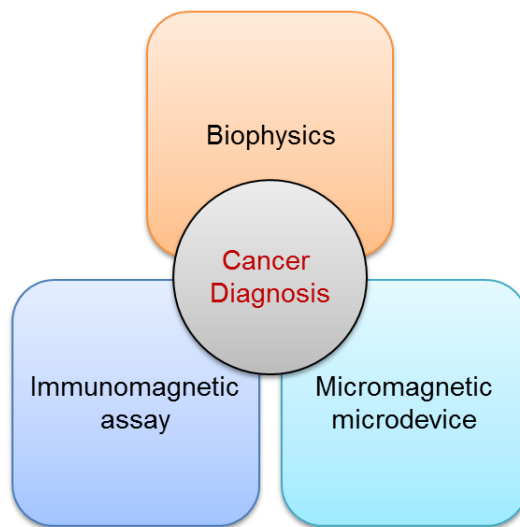


Figure 5.1: Dissertation contribution.

after capturing. We develop robust techniques to fabricate the micromagnets. The combination of the micromagnets and the immunomagnetic assay provides an efficient tool to probe cancer and other development diseases. We perform clinical studies with cancer patients, demonstrating the potential of the system in translational applications.

## 5.2 Future work

In the previous sections, we reviewed the CTC detection technologies based on mechanisms such as filtration, immunoassay, DEP separation, and hydrodynamic sorting. The fundamental goal of these systems is to yield high capture efficiency, high isolation purity, and high system throughput. In the meantime, they confront the same challenges that arise from CTCs'

rarity and heterogeneity. Going forward from this dissertation research, future endeavors could be move in the following directions.

The cell surface molecule EpCAM is a commonly used biomarker to target CTCs. However, EpCAM is not expressed on some types of cancer, and it may be down-regulated during metastasis. Depending on the specific targeting cancer type, additional antibodies need to be discovered. An alternative approach is to develop versatile nanoparticles with multiple antibody labelings. As a recent example, we have successfully demonstrated the improved capture of A-431 cells (skin cancer cells) using the combination of EpCAM/EGFR, SK-BR-3 cells (breast cancer cells) using EpCAM/HER2, and BT-20 cells (breast cancer cells) using EpCAM/MUC1. [9]

In addition, efforts in developing novel nano-carriers with hybrid functionalities should be considered. Figure 5.1 illustrates the concept of using a ciliated silicon micropillar for CTC detection. The principle is shown in Figure 5.1(a): the silicon micropillar ( $\sim 20\mu m$  in length) is coated with porous silicon nanowire ( $\sim 300nm$  in length) and is covered with a thin layer of Ni deposition on one end. The porous silicon nanowire coating works as the affinity domain, offering the selective binding with cancer cells through antibody - antigen interaction. The thin Ni layer works as the magnetic domain and provides the magnetic momentum for the cell-pillar complex. Figure 5.1(b) shows the SEM image of the fabricated ciliated micropillar. [128, 129] We test the micropillar carrier with SK-BR-3 cells, and the capture rate is 30% in the initial experiments. Figure 5.1(c) shows one

cancer cell being captured due to the attachment with the micropillars. The ciliated micropillar is one of the few CTC nanocarriers that is fabricated based on top-down techniques. [130,131]

There are several advantages to this micropillar approach. First, the magnetic momentum can be easily changed by fine-tuning the Ni deposition layer's thickness. Second, the large size of the pillars prevents them from being uptaken by the cells through endocytosis. It helps to obtain viable cells. Third, the porous nanowire dissolves in PBS buffer (phosphate buffered saline) after a certain amount of time, which essentially provides a capture-and-release assay. Therefore, the pillars can be detached from the cells after the capture, which can potentially eliminate the fluorescent quenching issue completely.

Most of the current studies regarding immunomagnetic assay focus on the existence determination of a single target, while the multiplexing capabilities of immunomagnetic assay are overlooked. [132, 133] Figure 5.2(a) illustrates the concept of multiplexing immunomagnetic detection. Two types of cells with different magnetic labelings flow through the microchannel placed in an external magnetic field. Since the applied magnetic forces are different, the cells with stronger magnetic responses are captured closer to the inlet, while the weaker cells tend to be captured at a distant location. The spatial information of the final locations of the captured cells can be used for cancer phenotyping.

We perform simple calculations based on our cell tracking algorithm-

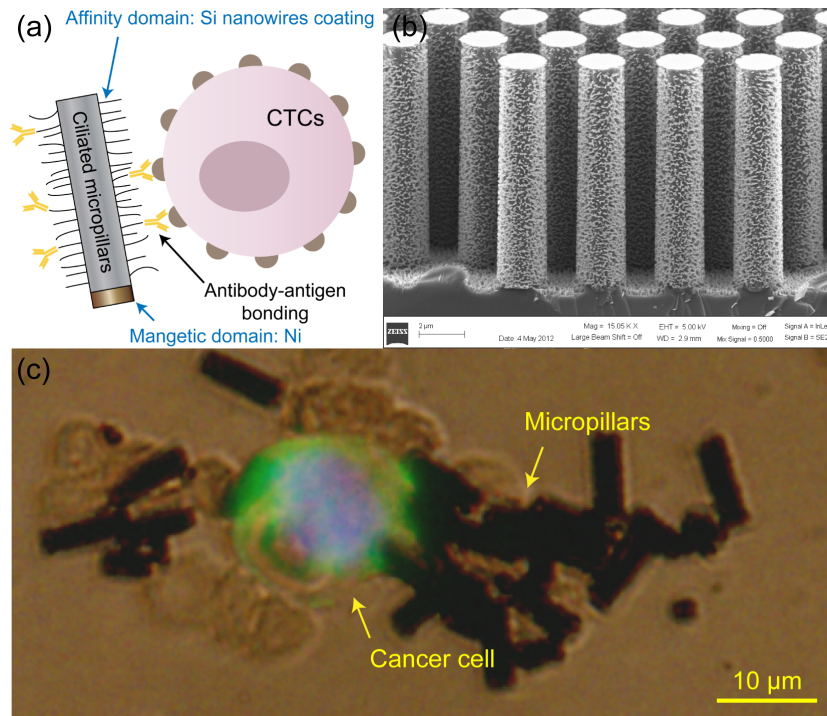


Figure 5.2: Ciliated micropillar based CTC detection. (a) Schematic of the ciliated micropillar based CTC detection. The micropillars have one affinity domain that binds to cancer cells based on antibody-antigen bonding. The magnetic domain on the tip of the micropillar provides the momentum to the CTC-pillar complex. (b) SEM of the fabricated ciliated micropillars. (c) Preliminary results of the micropillar screening experiments - the cancer cell is captured due to the attachment with the micropillars.

s. A mixture of three types of cells flows through a microchannel on top of three-parallel permanent magnet array. Figure 5.2(b) shows the trajectories of three types of cells, using the same labeling nanoparticle, but with different labeling numbers (red: 20000 per cell, green: 1000 per cell, blue: 50 per cell). It is corresponding to the case in which the cells have the same biomarker expression, but at different levels. Figure 5.2(c) shows the cell trajectories with three different types of nanoparticle labeling (radius of the nanoparticle - red: 100 nm, green: 25 nm, blue: 8 nm). This is to simulate the condition in which different biomarkers are expressed among different cell lines. In both cases, the trajectories show clear separations. Cells labeled with either larger nanoparticles, or more nanoparticles are captured first close to the inlet of the channel.

As a conceptual demonstration, we carry out experiments with two types of ferromagnetic nanoparticles made with the same Au shell/ iron oxide core, [9] but with different diameters of 6 nm and 100 nm. The distributions of the nanoparticles on the substrate are shown in Figure 5.2(d). We measure the maximum capture distance - 6 nm nanoparticles travel farther, with a maximum difference of 19%.

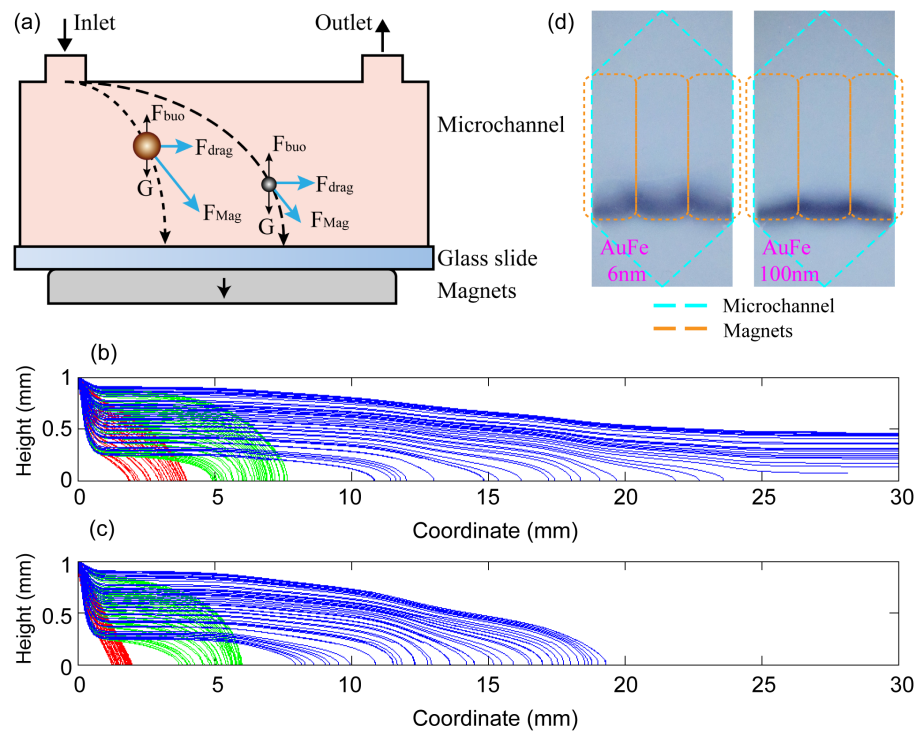


Figure 5.3: Multi-target immunomagnetic CTC phenotyping. (a) Concept of the multi-target detection. (b) Simulated cell trajectories with three targets labeled with different amount of nanoparticles. (c) Simulated cell trajectories with three targets labeled with nanoparticles of different diameters. (d) Conceptual demonstration using two types of ferromagnetic nanoparticles (6 nm and 100 nm). The maximum difference in capture distance is 19%.

## Appendices

# Appendix A

## Experimental protocols

### Cell culture protocols

For adherent cells, such PC3, SKBR3, MCF7 et al., they can be cultured and passaged based on the following protocol.

1. Remove and discard the used culture media from the culture petri dish.

2. Wash cells using 1 mL PBS(1X) buffer. Gently add wash solution to the side of the petri dish to avoid disturbing the cell layer, and rock the petri dish back and forth several times.

3. Remove and discard the wash solution from the petri dish.

4. Add the pre-warmed dissociation reagent such as trypsin to the petri dish; use enough reagent to cover the cell layer (approximately 3~5 mL). Gently rock the container to get complete coverage of the cell layer.

5. Keep the culture petri dish in the incubator (37°C) for approximately 5 minutes. Note that the actual incubation time varies with the cell line used.

6. Observe the cells under the microscope for detachment. If cells are

less than 90% detached, increase the incubation time a few more minutes, checking for dissociation every 30 seconds.

7. When >90% of the cells have detached, add the equivalent volumes (equal the volume used for the dissociation reagent) of pre-warmed complete growth medium. Disperse the medium by pipetting over the cell layer surface several times.

8. Transfer the cells to a 15-mL conical tube and centrifuge then at 1000 RPM for 3 minutes. Note that the centrifuge speed and time vary based on the cell type.

9. Remove and discard the supernatant in the conical tube. Re-suspend the cell pellet in a minimal volume of pre-warmed complete growth medium and remove a sample for counting.

10. Determine the total number of cells and percent viability using a hemacytometer, cell counter and Trypan Blue exclusion.

11. Dilute cell suspension to the seeding density recommended for the cell line, and pipet the appropriate volume into new cell culture petri dish, and return the cells to the incubator.

For non-adherent cells, such as COLO205, they can be directly transferred to the conical tube, and starting from Step 8. If over-growth, and cell clustering are observed, step 4, 5 can be performed by option to break the cell clusters.

Note: All solutions and equipment that come in contact with the

cells must be sterile. And all procedures must be performed in laminar flow hood.

## Cell counting protocols

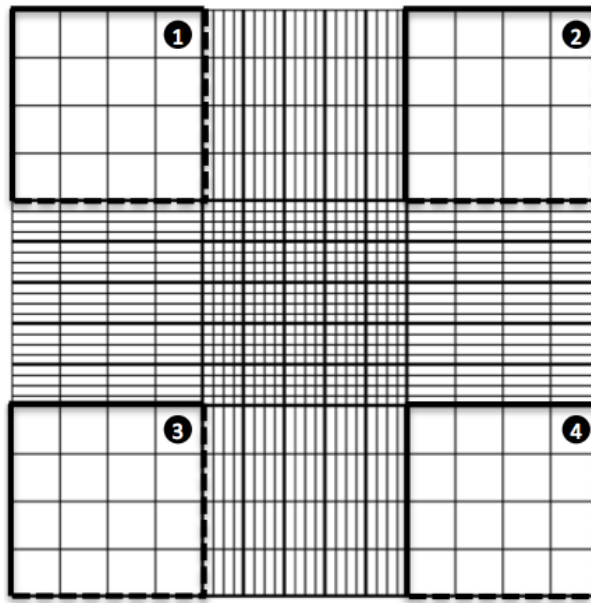


Figure A.1: Grids on the hemacytometer. Average number of cells found in area 1~4 multiplied by  $3 \times 10^4$  is the number of cells per mL in the original cell suspension.

Cell counting is performed using standard hemacytometer. Following is a brief introduction of the counting procedure.

1. Clean the chamber and the cover slip with alcohol. Dry and fix the cover slip in the right position.

2. Harvest the cells. Take  $50 \mu\text{L}$  cell suspension, and mix with same amount of PBS (1X), Trypan blue. Add  $10 \mu\text{L}$  of the mixed cell suspension

to the hemacytometer from the notch.

3. Place the chamber in the inverted microscope under 10X objective.

4. Count the cells in the large, central grid square (1 mm<sup>2</sup>), labeled with 1~4 in Figure A.1. Average the number from area 1~4, and multiply the value by  $3 \times 10^4$  to estimate the number of cells per mL in the original cell suspension.

### **Screening sample preparation**

1. Blood samples are obtained from healthy donors or cancer patients, and stored in *CellSave*<sup>TM</sup> (*Veridex, LLC, NJ*) tubes.

2. Blood samples are divided into multiple conical tubes, each containing 2.5 mL.

3. 2.2 mL of dilution buffer solution (*Veridex, LLC, NJ*) is added to each 2.5 mL blood, well mixed and centrifuged at 800g for 10 min.

4. Supernatant containing plasma as well as the buffer solution is removed till there is 2.5 mL solution in the tube. 1 mL buffer solution is added again to make screening sample of 3.5 mL.

5. Cancer cells are harvested, centrifuged, counted and resuspended in PBS buffer to prepare a solution with approximate 200 cells per 10  $\mu$ L.

6. 10  $\mu$ L cell suspension is added to each 3.5 mL aliquot of blood to prepare a sample spiked with ~200 cells.

7. 18.8  $\mu\text{L}$  Ferrofluid (*Veridex, LLC, NJ*) nanoparticle suspension is added to the screening sample, and well mixed.

8. 18.8  $\mu\text{L}$  Capture enhancement reagent (*Veridex, LLC, NJ*) is added to the screening sample, and well mixed.

9. The blood samples are kept in strong magnetic field to facilitate the nanoparticle binding for 10 mins before being loaded into the microchannel.

### **Blood sample screening protocols**

Blood samples are stored in a syringe that is connected to the microchannel before flowing into the channel. The blood samples and other screening solutions are introduced into the micro-chamber using a pressure driven syringe pump (*PHD 2000, Harvard Apparatus*) in the following orders. At different steps, the microchannel needs to be placed at different orientations to facilitate the operation.

1. PBS buffer is flowed into the microchannel, at a flow rate of 5~10 ml/hr to eject the air bubbles inside the tubing and microchannel. (Upright channel)

2. Blood samples are flowed into the microchannel at a constant flow rate of 2.5~10 ml/hr. (Inverted channel)

3. After blood flows out of the syringe, PBS is introduced with the same flow rate in step 2 to push the blood left in the tubing through the microchannel. (Inverted channel)

4. Keep introducing PBS until the red blood cells are not visible in the microchannel. (Vertical channel)

5. Bury the system in ice to cool down the system, at the same time keep flowing PBS. (Upright channel)

6. Add 1 mL of cold acetone at the same flow rate into the channel to fix the cancer cells onto the glass slide. (Upright channel)

7. After the screening, the microchannel is disassembled with the PDMS chamber and dried completely at room temperature.

8. The sample slides are stored at low temperature 4 °C until staining.

Note: From step 3 to 6, typically 4 mL of PBS buffer is needed to push the blood and flush the channel completely.

## **Cell staining protocols**

The experimental slides are stained with fluorescent dyes based on the following protocol.

1. Take the slides out of the fridge, warm up at room temperature and mark the staining area with hydrophobic pen.

2. Rinse/ rehydrate with PBST solution (PBS+ 0.1% Tween 20), wait for 5 minutes, and then apply Kimwipe on the side to remove excessive solution.

3. Add 300  $\mu$ L pre-warmed blocking buffer per slide to immerse the

staining area. Put slides in a plastic box, and add some water in the box outside of foil to prevent drying.

4. Incubate 30 mins in 37°C oven.

5. Remove the blocking buffer, and rinse the slides with PBS buffer.

Apply Kimwipe on the side to remove excessive solution.

6. Apply staining solution for CK and CD45.

7. Incubate 45 mins in 37°C oven.

8. Rinse with PBST, hold for 5 mins. Repeat 3 times.

9. Gently remove excessive PBST solution.

10. Apply DAPI staining solution 10  $\mu$ L on each slide, gently drop to cover the entire staining area.

11. Cover the staining are with glass coverslip. Store the samples at 4°C 30 mins before observation.

Note: The CK/ CD45 staining solution is composed of PBST, 1% BSA, cytokeratin dye solution (200:1), and CD45 dye solution (100:1). For example, 10 sample slides need 3000  $\mu$ L staining solution, which is made up of 3 mL PBST, 30 mg of BSA, 15  $\mu$ L cytokeratin solution and 30  $\mu$ L CD45 solution.

The DAPI staining solution is made by mountain media and DAPI solution mixed with 1:1 ratio.

## Inkjet fabrication

The instrument we use for the inkjet printing fabrication of the micromagnets is the DMP-2800 FUJIFILM Dimatrix Materials Printer. It is a sheet substrate scanning ink jet deposition system with drop observation, spot location, and variable printing resolution. A user-fillable piezo-based jetting cartridge is used to store the 'ink'. We use the cartridge with 10  $pL$  nozzle volume.

To achieve the best printing quality, some of the fluid physical characteristics needs to be pre-examined.

- 1) Viscosity - 10~12  $cP$  at the jetting temperature
- 2) Surface tension - 28~42  $dynes/cm$  at the jetting temperature
- 3) Filtration - for the 10  $pL$  cartridge, it is recommended to filter all fluids to 0.2  $\mu m$

There are also other parameters, such as the density needs to be greater than 1, the boiling point needs to be higher than 100 °C, the pH value needs to be between 4 and 9.

The piezo-jetting of the cartridge is controlled by a customized waveform. The typical basic waveform is divided into four segments, as shown in Figure A.2. Each segment has three properties: duration, level and slew rate. The level values, which is a percentage of the cartridge voltage. The level values in segment one and two have the most impact on the jetting process. Changing duration of segment one and slew rate and/or duration

of segment two changes drop formation largely. The applied voltage relates directly to the volume of the pumping chamber. Faster changes in voltage change the volume faster, bigger changes in voltage cause bigger volume changes. The slew rate determines the rate of the volume change.

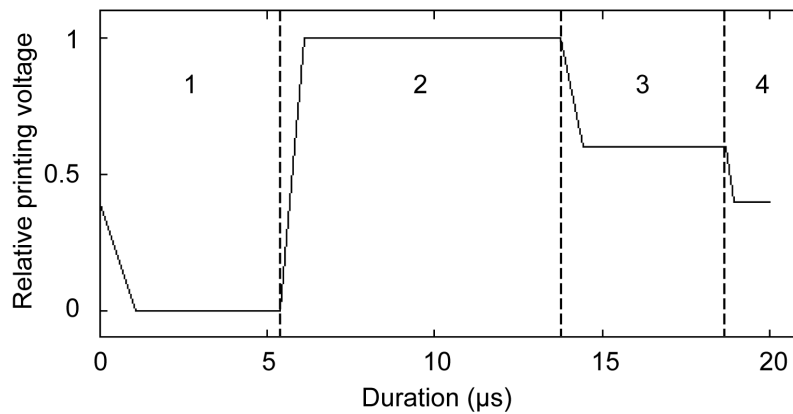


Figure A.2: Printing waveform of the inkjet printing instrument.

The waveform we used is summarized in table 2.

Table A.1: Inkjet micromagnet fabrication waveform parameters

Segment	Level (%)	Slew rate	Duration <sub>i</sub> ( $\mu$ s)
1	0	0.36	5.376
2	100	1.35	8.384
3	67	0.6	4.928
4	40	0.8	1.344

## Bibliography

- [1] A. C. Society. Cancer Facts and Figures. 2014.
- [2] M. Heron. Deaths: leading causes for 2010. *National vital statistics reports: from the Centers for Disease Control and Prevention, National Center for Health Statistics, National Vital Statistics System*, 62(6):1–97, 2013.
- [3] N. Beaulieu, D. Bloom, R. Bloom, and R. Stein. Breakaway: The global burden of cancer-challenges and opportunities. *The Economist Intelligence Unit*, 2009.
- [4] B. Alberts, J. Wilson, and T. Hunt. *Molecular Biology of the Cell*. Garland Science, 2008.
- [5] S. Paget. The distribution of secondary growths in cancer of the breast. *The Lancet*, 133(3421):571–573, 1889.
- [6] X. Zhe, M. L. Cher, and R. D. Bonfil. Circulating tumor cells: finding the needle in the haystack. *American journal of cancer research*, 1(6):740, 2011.
- [7] W. Kemmner. Currently used markers for CTC isolation-advantages, limitations and impact on cancer prognosis. *Journal of Clinical & Experimental Pathology*, 2011.
- [8] E. A. Punnoose, S. K. Atwal, J. M. Spoerke, H. Savage, A. Pandita, R.-F. Yeh, A. Pirzkall, B. M. Fine, L. C. Amler, D. S. Chen, et al. Molecular biomarker analyses using circulating tumor cells. *PloS one*, 5(9):e12517, 2010.

- [9] C.-H. Wu, Y.-Y. Huang, P. Chen, K. Hoshino, H. Liu, E. P. Frenkel, J. X. Zhang, and K. V. Sokolov. Versatile immunomagnetic nanocarrier platform for capturing cancer cells. *ACS nano*, 7(10):8816–8823, 2013.
- [10] M. Hosokawa, H. Kenmotsu, Y. Koh, T. Yoshino, T. Yoshikawa, T. Naito, T. Takahashi, H. Murakami, Y. Nakamura, A. Tsuya, et al. Size-based isolation of circulating tumor cells in lung cancer patients using a microcavity array system. *PloS one*, 8(6):e67466, 2013.
- [11] S. Park, R. R. Ang, S. P. Duffy, J. Bazov, K. N. Chi, P. C. Black, and H. Ma. Morphological Differences between Circulating Tumor Cells from Prostate Cancer Patients and Cultured Prostate Cancer Cells. *PloS one*, 9(1):e85264, 2014.
- [12] Y. Chen, P. Li, P.-H. Huang, Y. Xie, J. D. Mai, L. Wang, N.-T. Nguyen, and T. J. Huang. Rare cell isolation and analysis in microfluidics. *Lab on a Chip*, 14(4):626–645, 2014.
- [13] P. Li, Z. S. Stratton, M. Dao, J. Ritz, and T. Jun Huang. Probing circulating tumor cells in microfluidics. *Lab on a chip*, 13(4):602–609, 2013.
- [14] Y. Dong, A. M. Skelley, K. D. Merdek, K. M. Sprott, C. Jiang, W. E. Pierceall, J. Lin, M. Stocum, W. P. Carney, and D. A. Smirnov. Microfluidics and circulating tumor cells. *The Journal of Molecular Diagnostics*, 15(2):149–157, 2013.
- [15] Y. Gao, W. Li, and D. Pappas. Recent advances in microfluidic cell separations. *Analyst*, 138(17):4714–4721, 2013.
- [16] P. Chen, Y.-Y. Huang, K. Hoshino, and X. Zhang. Multiscale immunomagnetic enrichment of circulating tumor cells: from tubes to microchips. *Lab on a Chip*, 14(3):446–458, 2014.

- [17] S. J. Tan, R. L. Lakshmi, P. Chen, W.-T. Lim, L. Yobas, and C. T. Lim. Versatile label free biochip for the detection of circulating tumor cells from peripheral blood in cancer patients. *Biosensors and Bioelectronics*, 26(4):1701–1705, 2010.
- [18] S. Zheng, H. K. Lin, B. Lu, A. Williams, R. Datar, R. J. Cote, and Y.-C. Tai. 3D microfilter device for viable circulating tumor cell (CTC) enrichment from blood. *Biomedical microdevices*, 13(1):203–213, 2011.
- [19] Y. J. Kim, G.-B. Koo, J.-Y. Lee, H.-S. Moon, D.-G. Kim, D.-G. Lee, J.-Y. Lee, J. H. Oh, J.-M. Park, M. S. Kim, et al. A microchip filter device incorporating slit arrays and 3-D flow for detection of circulating tumor cells using CAV1-EpCAM conjugated microbeads. *Biomaterials*, 2014.
- [20] Y. Kim and Y.-H. Cho. A size-dependent microparticle capture and release chip using concentric membrane ring barriers. *Current Applied Physics*, 14(8):1016–1021, 2014.
- [21] M. Hosokawa, T. Hayata, Y. Fukuda, A. Arakaki, T. Yoshino, T. Tanaka, and T. Matsunaga. Size-selective microcavity array for rapid and efficient detection of circulating tumor cells. *Analytical chemistry*, 82(15):6629–6635, 2010.
- [22] R. Rosenberg, R. Gertler, J. Friederichs, K. Fuehrer, M. Dahm, R. Phelps, S. Thorban, H. Nekarda, and J. Siewert. Comparison of two density gradient centrifugation systems for the enrichment of disseminated tumor cells in blood. *Cytometry*, 49(4):150–158, 2002.
- [23] S. J. Tan, L. Yobas, G. Y. H. Lee, C. N. Ong, and C. T. Lim. Microdevice for the isolation and enumeration of cancer cells from blood. *Biomedical microdevices*, 11(4):883–892, 2009.

2009.

- [24] H. Mohamed, M. Murray, J. N. Turner, and M. Caggana. Isolation of tumor cells using size and deformation. *Journal of Chromatography A*, 1216(47):8289–8295, 2009.
- [25] D. R. Gossett, W. M. Weaver, A. J. Mach, S. C. Hur, H. T. K. Tse, W. Lee, H. Amini, and D. Di Carlo. Label-free cell separation and sorting in microfluidic systems. *Analytical and bioanalytical chemistry*, 397(8):3249–3267, 2010.
- [26] J. Zhou, P. V. Giridhar, S. Kasper, and I. Papautsky. Modulation of aspect ratio for complete separation in an inertial microfluidic channel. *Lab on a Chip*, 13(10):1919–1929, 2013.
- [27] D. W. Inglis. Efficient microfluidic particle separation arrays. *Applied Physics Letters*, 94(1):013510, 2009.
- [28] J. A. Davis, D. W. Inglis, K. J. Morton, D. A. Lawrence, L. R. Huang, S. Y. Chou, J. C. Sturm, and R. H. Austin. Deterministic hydrodynamics: taking blood apart. *Proceedings of the National Academy of Sciences*, 103(40):14779–14784, 2006.
- [29] S. C. Hur, A. J. Mach, and D. Di Carlo. High-throughput size-based rare cell enrichment using microscale vortices. *Biomicrofluidics*, 5(2):022206, 2011.
- [30] H. W. Hou, M. E. Warkiani, B. L. Khoo, Z. R. Li, R. A. Soo, D. S.-W. Tan, W.-T. Lim, J. Han, A. A. S. Bhagat, and C. T. Lim. Isolation and retrieval of circulating tumor cells using centrifugal forces. *Scientific reports*, 3, 2013.
- [31] M. E. Warkiani, G. Guan, K. B. Luan, W. C. Lee, A. A. S. Bhagat, P. K. Chaudhuri, D. S.-W. Tan, W. T. Lim, S. C. Lee, P. C. Chen, et al. Slanted spiral microfluidics for the

- ultra-fast, label-free isolation of circulating tumor cells. *Lab on a Chip*, 14(1):128–137, 2014.
- [32] G. Guan, L. Wu, A. A. Bhagat, Z. Li, P. C. Chen, S. Chao, C. J. Ong, and J. Han. Spiral microchannel with rectangular and trapezoidal cross-sections for size based particle separation. *Scientific reports*, 3, 2013.
- [33] J. Takagi, M. Yamada, M. Yasuda, and M. Seki. Continuous particle separation in a microchannel having asymmetrically arranged multiple branches. *Lab on a Chip*, 5(7):778–784, 2005.
- [34] S. Shim, P. Gascoyne, J. Noshari, and K. S. Hale. Dynamic physical properties of dissociated tumor cells revealed by dielectrophoretic field-flow fractionation. *Integrative Biology*, 3(8):850–862, 2011.
- [35] P. R. Gascoyne, J. Noshari, T. J. Anderson, and F. F. Becker. Isolation of rare cells from cell mixtures by dielectrophoresis. *Electrophoresis*, 30(8):1388–1398, 2009.
- [36] J. Yang, Y. Huang, X.-B. Wang, F. F. Becker, and P. R. Gascoyne. Cell separation on microfabricated electrodes using dielectrophoretic/gravitational field-flow fractionation. *Analytical Chemistry*, 71(5):911–918, 1999.
- [37] S. Nagrath, L. V. Sequist, S. Maheswaran, D. W. Bell, D. Irimia, L. Ulkus, M. R. Smith, E. L. Kwak, S. Digumarthy, A. Muzikansky, et al. Isolation of rare circulating tumour cells in cancer patients by microchip technology. *Nature*, 450(7173):1235–1239, 2007.
- [38] S. Wang, H. Wang, J. Jiao, K.-J. Chen, G. E. Owens, K.-i. Kamei, J. Sun, D. J. Sherman, C. P. Behrenbruch, H. Wu, et al. Three-Dimensional Nanostructured Sub-

- strates toward Efficient Capture of Circulating Tumor Cells. *Angewandte Chemie*, 121(47):9132–9135, 2009.
- [39] S. L. Stott, C.-H. Hsu, D. I. Tsukrov, M. Yu, D. T. Miyamoto, B. A. Waltman, S. M. Rothenberg, A. M. Shah, M. E. Smas, G. K. Korir, et al. Isolation of circulating tumor cells using a microvortex-generating herringbone-chip. *Proceedings of the National Academy of Sciences*, 107(43):18392–18397, 2010.
- [40] Y. Xu, J. A. Phillips, J. Yan, Q. Li, Z. H. Fan, and W. Tan. Aptamer-based microfluidic device for enrichment, sorting, and detection of multiple cancer cells. *Analytical chemistry*, 81(17):7436–7442, 2009.
- [41] J. A. Phillips, Y. Xu, Z. Xia, Z. H. Fan, and W. Tan. Enrichment of cancer cells using aptamers immobilized on a microfluidic channel. *Analytical chemistry*, 81(3):1033–1039, 2008.
- [42] J. Zhang, W. Sheng, and Z. H. Fan. An ensemble of aptamers and antibodies for multivalent capture of cancer cells. *Chemical Communications*, 50(51):6722–6725, 2014.
- [43] S. Mittal, I. Y. Wong, W. M. Deen, and M. Toner. Antibody-functionalized fluid-permeable surfaces for rolling cell capture at high flow rates. *Biophysical journal*, 102(4):721–730, 2012.
- [44] S. Mittal, I. Y. Wong, A. A. Yanik, W. M. Deen, and M. Toner. Discontinuous Nanoporous Membranes Reduce Non-Specific Fouling for Immunoaffinity Cell Capture. *Small*, 9(24):4207–4214, 2013.
- [45] W. Bonner, H. Hulett, R. Sweet, and L. Herzenberg. Fluorescence activated cell sorting. *Review of Scientific Instruments*, 43(3):404–409, 1972.

- [46] T.-H. Wu, Y. Chen, S.-Y. Park, J. Hong, T. Teslaa, J. F. Zhong, D. Di Carlo, M. A. Teitell, and P.-Y. Chiou. Pulsed laser triggered high speed microfluidic fluorescence activated cell sorter. *Lab on a Chip*, 12(7):1378–1383, 2012.
- [47] J. Krüger, K. Singh, A. O’Neill, C. Jackson, A. Morrison, and P. O’Brien. Development of a microfluidic device for fluorescence activated cell sorting. *Journal of Micromechanics and Microengineering*, 12(4):486, 2002.
- [48] K. Hoshino, Y.-Y. Huang, N. Lane, M. Huebschman, J. W. Uhr, E. P. Frenkel, and X. Zhang. Microchip-based immunomagnetic detection of circulating tumor cells. *Lab on a Chip*, 11(20):3449–3457, 2011.
- [49] B. D. Plouffe, M. Mahalanabis, L. H. Lewis, C. M. Klapperich, and S. K. Murthy. Clinically relevant microfluidic magnetophoretic isolation of rare-cell populations for diagnostic and therapeutic monitoring applications. *Analytical chemistry*, 84(3):1336–1344, 2012.
- [50] J. Chung, D. Issadore, A. Ullal, K. Lee, R. Weissleder, and H. Lee. Rare cell isolation and profiling on a hybrid magnetic/size-sorting chip. *Biomicrofluidics*, 7(5):054107, 2013.
- [51] S. Miltenyi, W. Müller, W. Weichel, and A. Radbruch. High gradient magnetic cell separation with MACS. *Cytometry*, 11(2):231–238, 1990.
- [52] M. Nakamura, K. Decker, J. Chosy, K. Comella, K. Melnik, L. Moore, L. C. Lasky, M. Zborowski, and J. J. Chalmers. Separation of a breast cancer cell line from human blood using a quadrupole magnetic flow sorter. *Biotechnology progress*, 17(6):1145–1155, 2001.

- [53] A. H. Talasaz, A. A. Powell, D. E. Huber, J. G. Berbee, K.-H. Roh, W. Yu, W. Xiao, M. M. Davis, R. F. Pease, M. N. Mindrinos, et al. Isolating highly enriched populations of circulating epithelial cells and other rare cells from blood using a magnetic sweeper device. *Proceedings of the National Academy of Sciences*, 106(10):3970–3975, 2009.
- [54] A. A. Powell, A. H. Talasaz, H. Zhang, M. A. Coram, A. Reddy, G. Deng, M. L. Telli, R. H. Advani, R. W. Carlson, J. A. Mollick, et al. Single cell profiling of circulating tumor cells: transcriptional heterogeneity and diversity from breast cancer cell lines. *PloS one*, 7(5):e33788, 2012.
- [55] M. Balic, N. Dandachi, G. Hofmann, H. Samonigg, H. Loibner, A. Obwaller, A. van der Kooi, A. G. Tibbe, G. V. Doyle, L. W. Terstappen, et al. Comparison of two methods for enumerating circulating tumor cells in carcinoma patients. *Cytometry Part B: Clinical Cytometry*, 68(1):25–30, 2005.
- [56] M. C. Miller, G. V. Doyle, and L. W. Terstappen. Significance of circulating tumor cells detected by the CellSearch system in patients with metastatic breast colorectal and prostate cancer. *Journal of oncology*, 2010, 2009.
- [57] M. Cristofanilli, G. T. Budd, M. J. Ellis, A. Stopeck, J. Matera, M. C. Miller, J. M. Reuben, G. V. Doyle, W. J. Allard, L. W. Terstappen, et al. Circulating tumor cells, disease progression, and survival in metastatic breast cancer. *New England Journal of Medicine*, 351(8):781–791, 2004.
- [58] G. T. Budd, M. Cristofanilli, M. J. Ellis, A. Stopeck, E. Borden, M. C. Miller, J. Matera, M. Repollet, G. V. Doyle, L. W. Terstappen, et al. Circulating tumor cells versus imaging predicting overall survival in metastatic breast cancer. *Clinical Cancer Research*,

12(21):6403–6409, 2006.

- [59] S. J. Cohen, C. J. Punt, N. Iannotti, B. H. Saidman, K. D. Sabbath, N. Y. Gabrail, J. Picus, M. Morse, E. Mitchell, M. C. Miller, et al. Relationship of circulating tumor cells to tumor response, progression-free survival, and overall survival in patients with metastatic colorectal cancer. *Journal of Clinical Oncology*, 26(19):3213–3221, 2008.
- [60] J. S. de Bono, H. I. Scher, R. B. Montgomery, C. Parker, M. C. Miller, H. Tissing, G. V. Doyle, L. W. Terstappen, K. J. Pienta, and D. Raghavan. Circulating tumor cells predict survival benefit from treatment in metastatic castration-resistant prostate cancer. *Clinical Cancer Research*, 14(19):6302–6309, 2008.
- [61] D. F. Hayes, M. Cristofanilli, G. T. Budd, M. J. Ellis, A. Stopeck, M. C. Miller, J. Matera, W. J. Allard, G. V. Doyle, and L. W. Terstappen. Circulating tumor cells at each follow-up time point during therapy of metastatic breast cancer patients predict progression-free and overall survival. *Clinical Cancer Research*, 12(14):4218–4224, 2006.
- [62] J. G. Moreno, M. C. Miller, S. Gross, W. J. Allard, L. G. Gomella, and L. W. Terstappen. Circulating tumor cells predict survival in patients with metastatic prostate cancer. *Urology*, 65(4):713–718, 2005.
- [63] M. Zborowski, C. B. Fuh, R. Green, L. Sun, and J. J. Chalmers. Analytical magnetapheresis of ferritin-labeled lymphocytes. *Analytical chemistry*, 67(20):3702–3712, 1995.
- [64] Y.-y. Huang, K. Hoshino, P. Chen, C.-h. Wu, N. Lane, M. Huebschman, H. Liu, K. Sokolov, J. W. Uhr, E. P. Frenkel, et al. Immunomagnetic nanoscreening of

- circulating tumor cells with a motion controlled microfluidic system. *Biomedical microdevices*, 15(4):673–681, 2013.
- [65] T. Zhu, R. Cheng, S. A. Lee, E. Rajaraman, M. A. Eiteman, T. D. Querec, E. R. Unger, and L. Mao. Continuous-flow ferrohydrodynamic sorting of particles and cells in microfluidic devices. *Microfluidics and nanofluidics*, 13(4):645–654, 2012.
- [66] J. H. Kang, S. Krause, H. Tobin, A. Mammoto, M. Kanapathipillai, and D. E. Ingber. A combined micromagnetic-microfluidic device for rapid capture and culture of rare circulating tumor cells. *Lab on a Chip*, 12(12):2175–2181, 2012.
- [67] E. Ozkumur, A. M. Shah, J. C. Ciciliano, B. L. Emmink, D. T. Miyamoto, E. Brachtel, M. Yu, P.-i. Chen, B. Morgan, J. Trautwein, et al. Inertial focusing for tumor antigen-dependent and-independent sorting of rare circulating tumor cells. *Science translational medicine*, 5(179):179ra47–179ra47, 2013.
- [68] N. M. Karabacak, P. S. Spuhler, F. Fachin, E. J. Lim, V. Pai, E. Ozkumur, J. M. Martel, N. Kojic, K. Smith, P.-i. Chen, et al. Microfluidic, marker-free isolation of circulating tumor cells from blood samples. *Nature protocols*, 9(3):694–710, 2014.
- [69] C. Chang, S. Jalal, W. Huang, A. Mahmood, D. Matei, and C. Savran. High-throughput Immunomagnetic Cell Detection using a Micro-aperture Chip System. *Sensors Journal, IEEE*, PP(99):1–1, 2014.
- [70] M. Yu, A. Bardia, B. S. Wittner, S. L. Stott, M. E. Smas, D. T. Ting, S. J. Isakoff, J. C. Ciciliano, M. N. Wells, A. M. Shah, et al. Circulating breast tumor cells exhibit dynamic changes in epithelial and mesenchymal composition. *Science*, 339(6119):580–584, 2013.

- [71] M. Pestrin, S. Bessi, F. Galardi, M. Truglia, A. Biggeri, C. Biagioni, S. Cappadona, L. Biganzoli, A. Giannini, and A. Di Leo. Correlation of HER2 status between primary tumors and corresponding circulating tumor cells in advanced breast cancer patients. *Breast cancer research and treatment*, 118(3):523–530, 2009.
- [72] M. Yu, D. T. Ting, S. L. Stott, B. S. Wittner, F. Ozsolak, S. Paul, J. C. Ciciliano, M. E. Smas, D. Winokur, A. J. Gilman, et al. RNA sequencing of pancreatic circulating tumour cells implicates WNT signalling in metastasis. *Nature*, 2012.
- [73] S. Maheswaran, L. V. Sequist, S. Nagrath, L. Ulkus, B. Brannigan, C. V. Collura, E. Inserra, S. Diederichs, A. J. Iafrate, and D. W. Bell. Detection of mutations in EGFR in circulating lung-cancer cells. *New England Journal of Medicine*, 359(4):366–377, 2008.
- [74] A. Martowicz, G. Spizzo, G. Gastl, and G. Untergasser. Phenotype-dependent effects of EpCAM expression on growth and invasion of human breast cancer cell lines. *BMC cancer*, 12(1):501, 2012.
- [75] W. Onstenk, J. Gratama, J. Foekens, and S. Sleijfer. Towards a personalized breast cancer treatment approach guided by circulating tumor cell (CTC) characteristics. *Cancer treatment reviews*, 39(7):691–700, 2013.
- [76] S. S. Kanwar, L. Rivera, and S. Nagrath. Personalized Medicine through Circulating Tumor Cells: The New Dimension in Cancer Research. *Journal of Developing Drugs*, 2013.
- [77] E. M. Matthew and J.-N. Gallant. Sizing up circulating tumor cells for personalized therapy. *Cell Cycle*, 12(15):2346, 2013.

- [78] C. Sun and L. L. Munn. Particulate nature of blood determines macroscopic rheology: a 2-D lattice Boltzmann analysis. *Biophysical journal*, 88(3):1635–1645, 2005.
- [79] K.-i. Tsubota, S. Wada, H. Kamada, Y. Kitagawa, R. Lima, and T. Yamaguchi. A particle method for blood flow simulation, application to flowing red blood cells and platelets. *Journal of the Earth Simulator*, 5:2–7, 2006.
- [80] K. Hoshino, P. Chen, Y.-Y. Huang, and X. Zhang. Computational analysis of microfluidic immunomagnetic rare cell separation from a particulate blood flow. *Analytical chemistry*, 84(10):4292–4299, 2012.
- [81] A. Einstein. *Investigations on the Theory of the Brownian Movement*. Courier Dover Publications, 1956.
- [82] J. W. Judy and R. S. Muller. Magnetic microactuation of torsional polysilicon structures. *Sensors and Actuators A: Physical*, 53(1–3):392–397, 1996.
- [83] E. P. Furlani and Y. Sahoo. Analytical model for the magnetic field and force in a magnetophoretic microsystem. *Journal of Physics D: Applied Physics*, 39(9):1724, 2006.
- [84] D. W. Inglis, R. Riehn, R. Austin, and J. Sturm. Continuous microfluidic immunomagnetic cell separation. *Applied Physics Letters*, 85(21):5093–5095, 2004.
- [85] J.-W. Choi, C. H. Ahn, S. Bhansali, and H. T. Henderson. A new magnetic bead-based, filterless bio-separator with planar electromagnet surfaces for integrated bio-detection systems. *Sensors and Actuators B: Chemical*, 68(1):34–39, 2000.
- [86] K. Smistrup, O. Hansen, H. Bruus, and M. F. Hansen. Magnetic separation in microfluidic systems using microfabricated electromagnet experiments and simulations. *Journal of Magnetism and Magnetic Materials*, 293(1):597–604, 2005.

- [87] C.-H. Chiou, Y.-Y. Huang, M.-H. Chiang, H.-H. Lee, and G.-B. Lee. New magnetic tweezers for investigation of the mechanical properties of single DNA molecules. *Nanotechnology*, 17(5):1217, 2006.
- [88] K. Smistrup, T. Lund-Olesen, M. F. Hansen, and P. T. Tang. Microfluidic magnetic separator using an array of soft magnetic elements. *Journal of Applied Physics*, 99(8):08P102, 2006.
- [89] X. Yu, X. Feng, J. Hu, Z.-L. Zhang, and D.-W. Pang. Controlling the magnetic field distribution on the micrometer scale and generation of magnetic bead patterns for microfluidic applications. *Langmuir*, 27(8):5147–5156, 2011.
- [90] Y. Huang, P. Chen, K. Hoshino, C. Wu, N. Lane, M. Huebschman, J. Uhr, K. Sokolov, E. Frenkel, and X. Zhang. Patterned nanomagnets on-chip for screening circulating tumor cells in blood. In *part at the The 16th International Conference on Miniaturized Systems for Chemistry and Life Sciences ( $\mu$ TAS), Okinawa, Japan, 2012.*
- [91] A. Walther, C. Marcoux, B. Desloges, R. Grechishkin, D. Givord, and N. Dempsey. Micro-patterning of NdFeB and SmCo magnet films for integration into micro-electro-mechanical-systems. *Journal of Magnetism and Magnetic Materials*, 321(6):590–594, 2009.
- [92] D. Nawarathna, N. Norouzi, J. McLane, H. Sharma, N. Sharac, T. Grant, A. Chen, S. Strayer, R. Ragan, and M. Khine. Shrink-induced sorting using integrated nanoscale magnetic traps. *Applied Physics Letters*, 102(6):063504–063504–5, 2013.
- [93] F. Dumas-Bouchiat, L. F. Zanini, M. Kustov, N. M. Dempsey, R. Grechishkin, K. Hasselbach, J. C. Orlianges, C. Champeaux, A. Catherinot, and D. Givord. Thermomag-

- netically patterned micromagnets. *Applied Physics Letters*, 96(10):102511–102511–3, 2010.
- [94] L.-F. Zanini, N. M. Dempsey, D. Givord, G. Reyne, and F. Dumas-Bouchiat. Autonomous micro-magnet based systems for highly efficient magnetic separation. *Applied Physics Letters*, 99(23):232504, 2011.
- [95] L.-F. Zanini, O. Osman, M. Frénéa-Robin, N. Haddour, N. Dempsey, G. Reyne, and F. Dumas-Bouchiat. Micromagnet structures for magnetic positioning and alignment. *Journal of Applied Physics*, 111(7):07B312, 2012.
- [96] J. Xia, X. Chen, C. Zhou, Y. Li, and Z. Peng. Development of a low-cost magnetic microfluidic chip for circulating tumour cell capture. *IET nanobiotechnology*, 5(4):114–120, 2011.
- [97] C. Fanelli, S. Coppola, R. Barone, C. Colussi, G. Gualandi, P. Volpe, and L. Ghibelli. Magnetic fields increase cell survival by inhibiting apoptosis via modulation of Ca<sup>2+</sup> influx. *The FASEB Journal*, 13(1):95–102, 1999.
- [98] T. Kimura, M. Yamato, and A. Nara. Particle trapping and undulation of a liquid surface using a microscopically modulated magnetic field. *Langmuir*, 20(3):572–574, 2004.
- [99] C. Lee, H. Lee, and R. Westervelt. Microelectromagnets for the control of magnetic nanoparticles. *Applied physics letters*, 79(20):3308–3310, 2001.
- [100] H. Lee, A. Purdon, and R. Westervelt. Manipulation of biological cells using a microelectromagnet matrix. *Applied physics letters*, 85(6):1063–1065, 2004.

- [101] D. Hsieh, R. Langer, and J. Folkman. Magnetic modulation of release of macromolecules from polymers. *Proceedings of the National Academy of Sciences*, 78(3):1863–1867, 1981.
- [102] U. E. Steiner and T. Ulrich. Magnetic field effects in chemical kinetics and related phenomena. *Chemical Reviews*, 89(1):51–147, 1989.
- [103] T. Deng, M. Prentiss, and G. M. Whitesides. Fabrication of magnetic microfiltration systems using soft lithography. *Applied physics letters*, 80(3):461–463, 2002.
- [104] P. Chen, Y.-Y. Huang, K. Hoshino, and X. Zhang. On-chip magnetic field modulation for distributed immunomagnetic detection of circulating tumor cells. In *The 17th International Conference on Solid-State Sensors, Actuators and Microsystems (Transducers 2013)*, pages 1202–1205, 2013.
- [105] A. D. Stroock, S. K. Dertinger, A. Ajdari, I. Mezić, H. A. Stone, and G. M. Whitesides. Chaotic mixer for microchannels. *Science*, 295(5555):647–651, 2002.
- [106] M. Singh, H. M. Haverinen, P. Dhagat, and G. E. Jabbour. Inkjet printing—process and its applications. *Advanced materials*, 22(6):673–685, 2010.
- [107] E. Tekin, P. J. Smith, and U. S. Schubert. Inkjet printing as a deposition and patterning tool for polymers and inorganic particles. *Soft Matter*, 4(4):703–713, 2008.
- [108] G. C. Jensen, C. E. Krause, G. A. Sotzing, and J. F. Rusling. Inkjet-printed gold nanoparticle electrochemical arrays on plastic. Application to immunodetection of a cancer biomarker protein. *Physical Chemistry Chemical Physics*, 13(11):4888–4894, 2011.

- [109] V. N. Truskett and M. P. Watts. Trends in imprint lithography for biological applications. *Trends in biotechnology*, 24(7):312–317, 2006.
- [110] J. Seekamp, S. Zankovych, A. Helfer, P. Maury, C. S. Torres, G. Boettger, C. Liguda, M. Eich, B. Heidari, and L. Montelius. Nanoimprinted passive optical devices. *Nanotechnology*, 13(5):581, 2002.
- [111] E. Tekin, P. J. Smith, S. Hoepfner, A. M. van den Berg, A. S. Susa, A. L. Rogach, J. Feldmann, and U. S. Schubert. Inkjet printing of luminescent CdTe nanocrystal-polymer composites. *Advanced Functional Materials*, 17(1):23–28, 2007.
- [112] W. Wu, G.-Y. Jung, D. Olynick, J. Straznicky, Z. Li, X. Li, D. Ohlberg, Y. Chen, S.-Y. Wang, and J. Liddle. One-kilobit cross-bar molecular memory circuits at 30-nm half-pitch fabricated by nanoimprint lithography. *Applied Physics A*, 80(6):1173–1178, 2005.
- [113] J. D. Kim, J. S. Choi, B. S. Kim, Y. Chan Choi, and Y. W. Cho. Piezoelectric inkjet printing of polymers: Stem cell patterning on polymer substrates. *Polymer*, 51(10):2147–2154, 2010.
- [114] W. Voit, W. Zapka, L. Belova, and K. Rao. Application of inkjet technology for the deposition of magnetic nanoparticles to form micron-scale structures. In *Science, Measurement and Technology, IEEE Proceedings*, volume 150. IET, 2003.
- [115] S. B. Fuller, E. J. Wilhelm, and J. M. Jacobson. Ink-jet printed nanoparticle microelectromechanical systems. *Journal of Microelectromechanical Systems*, 11(1):54–60, 2002.

- [116] J. A. Lim, W. H. Lee, H. S. Lee, J. H. Lee, Y. D. Park, and K. Cho. Self-Organization of Ink-jet-Printed Triisopropylsilylethynyl Pentacene via Evaporation-Induced Flows in a Drying Droplet. *Advanced functional materials*, 18(2):229–234, 2008.
- [117] C. H. Chon, S. Paik, J. B. Tipton, and K. D. Kihm. Effect of nanoparticle sizes and number densities on the evaporation and dryout characteristics for strongly pinned nanofluid droplets. *Langmuir*, 23(6):2953–2960, 2007.
- [118] E. P. Furlani. *Permanent magnet and electromechanical devices: materials, analysis, and applications*. Academic Press, 2001.
- [119] G. De Simone, R. B. Devereux, S. Chien, M. H. Alderman, S. A. Atlas, and J. H. Laragh. Relation of blood viscosity to demographic and physiologic variables and to cardiovascular risk factors in apparently normal adults. *Circulation*, 81(1):107–117, 1990.
- [120] A. Pries, D. Neuhaus, and P. Gaehtgens. Blood viscosity in tube flow: dependence on diameter and hematocrit. *American Journal of Physiology*, 263:H1770–H1770, 1992.
- [121] G. Batchelor. The effect of Brownian motion on the bulk stress in a suspension of spherical particles. *Journal of Fluid Mechanics*, 83(01):97–117, 1977.
- [122] M. Mooney. The viscosity of a concentrated suspension of spherical particles. *Journal of colloid science*, 6(2):162–170, 1951.
- [123] K. S. Kim and J.-K. Park. Magnetic force-based multiplexed immunoassay using superparamagnetic nanoparticles in microfluidic channel. *Lab on a Chip*, 5(6):657–664, 2005.

- [124] C. W. Yung, J. Fiering, A. J. Mueller, and D. E. Ingber. Micromagnetic–microfluidic blood cleansing device. *Lab on a Chip*, 9(9):1171–1177, 2009.
- [125] B. Mostert, S. Sleijfer, J. A. Foekens, and J. W. Gratama. Circulating tumor cells (CTCs): detection methods and their clinical relevance in breast cancer. *Cancer treatment reviews*, 35(5):463–474, 2009.
- [126] E. Furlani. Magnetophoretic separation of blood cells at the microscale. *Journal of Physics D: Applied Physics*, 40(5):1313, 2007.
- [127] J. Crangle and G. M. Goodman. The Magnetization of Pure Iron and Nickel. *Proceedings of the Royal Society of London. A. Mathematical and Physical Sciences*, 321(1547):477–491, 1971.
- [128] Z. Wang, H.-j. Wu, D. Fine, J. Schmulen, Y. Hu, B. Godin, J. X. J. Zhang, and X. Liu. Ciliated micropillars for the microfluidic-based isolation of nanoscale lipid vesicles. *Lab on a Chip*, 13:2879–2882, 2013.
- [129] C. Chiappini, X. Liu, J. R. Fakhoury, and M. Ferrari. Biodegradable porous silicon barcode nanowires with defined geometry. *Advanced functional materials*, 20(14):2231–2239, 2010.
- [130] H. Liu, Y. Li, K. Sun, J. Fan, P. Zhang, J. Meng, S. Wang, and L. Jiang. Dual-responsive surfaces modified with phenylboronic acid-containing polymer brush to reversibly capture and release cancer cells. *Journal of the American Chemical Society*, 135(20):7603–7609, 2013.
- [131] X. Yu, R. He, S. Li, B. Cai, L. Zhao, L. Liao, W. Liu, Q. Zeng, H. Wang, S.-S. Guo, et al. Magneto-Controllable Capture and Release of Cancer Cells by Using a Micropillar

Device Decorated with Graphite Oxide-Coated Magnetic Nanoparticles. *Small*, 9(22):3895–3901, 2013.

[132] J. D. Adams, U. Kim, and H. T. Soh. Multitarget magnetic activated cell sorter. *Proceedings of the National Academy of Sciences*, 105(47):18165–18170, 2008.

[133] U. Kim, J. Qian, S. A. Kenrick, P. S. Daugherty, and H. T. Soh. Multitarget dielectrophoresis activated cell sorter. *Analytical chemistry*, 80(22):8656–8661, 2008.